Universität Hamburg
DER FORSCHUNG | DER LEHRE | DER BILDUNG

# From 2D to 3D -
# Neurite Guiding Scaffolds for Designer Neuronal Networks

**Dissertation**

zur Erlangung des Doktorgrades

an der Fakultät für Mathematik, Informatik und Naturwissenschaften

Fachbereich Physik

der Universität Hamburg

vorgelegt von

***Cornelius Fendler***

- Hamburg, 2019 -

GUTACHTER DER DISSERTATION:

Prof. Dr. Robert H. Blick

Prof. Dr. Wolfgang J. Parak

Prof. Dr. Linwei Yu

MITGLIEDER DER PRÜFUNGSKOMMISSION:

Prof. Dr. Robert H. Blick

Prof. Dr. Wolfgang J. Parak

Prof. Dr. Michael A. Rübhausen

Prof. Dr. Viacheslav Nikolaev

Prof. Dr. Gabriel Bester

DATUM DER DISPUTATION:

14.08.2020

VORSITZENDER DER PRÜFUNGSKOMMISSION:

Prof. Dr. Michael A. Rübhausen

VORSITZENDER DES FACH-PROMOTIONSAUSSCHUSSES PHYSIK:

Prof. Dr. Günter H. W. Sigl

LEITER DES FACHBEREICHS PHYSIK:

Prof. Dr. Wolfgang Hansen

DEKAN DER MIN-FAKULTÄT:

Prof. Dr. Heinrich Graener

# Abstract

*In vitro* neuronal cultures on artificial substrates are essential tools for neuroscience. Microstructured surfaces and targeted chemical preparation have been utilized in recent years to fabricate substrates for the development of ordered neuronal networks with substrate-specific geometry.

In this thesis, new types of culture platforms are introduced that enable the design of tailor-made neuronal networks beyond planar 2D geometries. First, surface shaping to grooves and steps - produced with grayscale lithography, reactive ion etching and nanoimprint lithography - is presented for the study of directed neurite outgrowth on 2.5D pathways. Second, novel 3D cell culture platforms produced with direct laser writing by two-photon polymerization are introduced. These platforms consist of pillars of varying heights with cavities at the top and free-standing tunnels that connect the cavities with each other.

Substrates are cultivated with two different kinds of neurons - primary murine cerebellar granular cells and humane midbrain dopaminergic neurons derived from small molecule neural precursor cells. Surface coatings of $Al_2O_3$ and the polymer parylene-C promote neuron adhesion and vitality. Topological guidance of neurite outgrowth inherent to the substrate geometry is combined with chemical guidance through selective poly-D-lysine deposition. Simultaneous function of the 3D cell culture platforms as neurocages as well as neuroguides is shown by selective cell adhesion inside the cavities and neurite outgrowth through tunnels, which lead to the formation of ordered neuronal networks. Electrical activity in the neuronal networks is verified and analyzed with patch clamping measurements. Variations of the design of the platforms show that the tunnels can be freely arranged in any spatial direction according to the desired network geometry and act as customizable pathways for neurite outgrowth in 3D. Thus, the presented concept establishes *in vitro* neuronal networks with design-specific 3D complexity.

# Zusammenfassung

Neuronale *in vitro* Kulturen auf künstlichen Substraten sind wichtige Werkzeuge der Neurowissenschaften. Mikrostrukturierung von Oberflächen und gezielte chemische Behandlung wurden in den vergangenen Jahren angewendet, um Substrate zur Kultivierung von geordneten neuronalen Netzwerken mit substratspezifischer Geometrie herzustellen.

Im Rahmen dieser Doktorarbeit werden neue Arten von Zellkulturplattformen vorgestellt, die die Entwicklung von maßgeschneiderten neuronalen Netzwerken ermöglichen, welche über planare 2D Geometrien hinaus gehen. Zunächst wird Oberflächenmodellierung mit Gräben und Stufen für die Untersuchung von gerichtetem Neuritwachstum mit 2,5D Verlauf gezeigt, die mittels Graustufenlithographie, reaktivem Ionenätzen und Nanoprägelithographie hergestellt wird. Anschließend werden neuartige 3D Zellkulturplattformen vorgestellt, die mittels Laserdirektschreiben durch Zweiphotonenlithographie hergestellt werden. Diese Plattformen bestehen aus Säulen verschiedener Höhe mit Hohlräumen am oberen Ende und freistehenden Tunneln, die diese Hohlräume miteinander verbinden.

Die Substrate werden mit zwei verschiedenen Arten von Neuronen kultiviert: Primären Körnerzellen, extrahiert aus Cerebella von Mäusen, und menschlichen dopaminergen Neuronen des Mittelhirns, die aus neuronalen Vorläuferzellen differenziert werden. $Al_2O_3$ und das Polymer Parylen-C als Oberflächenbeschichtungen fördern die Adhäsion und Vitalität von Neuronen. Topologische Lenkung von Neuritwachstum durch die Substratgeometrie wird kombiniert mit chemischenm Signalmolekülen durch selektive Abscheidung von Poly-D-Lysin. Die Effektivität der vorgestellten 3D Zellkulturplattformen sowohl als 'Neuronenkäfige' als auch als 'Neuronenguides' wird demonstriert durch selektive Zelladhäsion in den Hohlräumen und Neuritewachstum durch die Tunnel. Dies führt zur Ausbildung von geordneten neuronalen Netzen. Elektrische Aktivität der neuronalen Netzwerke wird mittels Patch Clamping nachgewiesen und analysiert. Variationen im Design der Plattformen veranschaulichen, dass die Tunnel je nach gewünschter Netzwerkgeometrie frei im Raum angeordnet werden können und als veränderbare Pfade für Neuritwachstum in 3D fungieren. Damit etabliert das vorgestellte Konzept erfolgreich *in vitro* neuronale Netzwerke mit designspezifischer 3D Komplexität.

# Contents

# Abbreviations

| | |
|---|---|
| **1PP** | one-photon polymerization |
| **2D** | two-dimensional |
| **2.5D** | two-and-a-half-dimensional |
| **2PA** | two-photon absorption |
| **2PP** | two-photon polymerization |
| **3D** | three-dimensional |
| **ALD** | atomic layer deposition |
| **BSA** | bovine serum albumin |
| **CAD** | computer-aided design |
| **CAMs** | cell adhesion molecules |
| **CNS** | central nervous system |
| **CLSM** | confocal laser scanning microscopy |
| **CVD** | chemical vapor deposition |
| **DIV** | days *in vitro* |
| **DLW** | direct laser writing |
| **DMSO** | dimethyl sulfoxide |
| **EDTA** | ethylenediaminetetraacetic acid |
| **FIB** | focused ion beam |
| **FWHM** | full width at half maximum |
| **GFP** | green fluorescent protein |
| **GSL** | grayscale lithography |
| **HEPES** | 4-(2-hydroxyethyl)-1-piperazineethanesulfonic acid |
| **HBSS** | Hank's Balanced Salt Solution |
| **ICP** | inductively-coupled plasma |
| **IPA** | isopropyl alcohol |
| **iPSCs** | induced pluripotent stem cells |
| **mDANs** | midbrain dopaminergic neurons |
| **MPA** | multi-photon absorption |
| **MPP** | multi-photon polymerization |

| | |
|---|---|
| **MCGCs** | murine cerebellar granule cells |
| **NIL** | nanoimprint lithography |
| **UV-NIL** | ultraviolet nanoimprint lithography |
| **ParC** | parylene-C |
| **PBS** | phosphate-buffered saline |
| **PDL** | poly-D-lysine |
| **PI** | propidium iodide |
| **PLL** | poly-L-lysine |
| **PMT** | photomultiplier tube |
| **PPGT** | Photonic Professional GT |
| **PVD** | physical vapor deposition |
| **RIE** | reactive ion etching |
| **RMP** | resting membrane potential |
| **RT** | room temperature |
| **SEM** | scanning electron microscopy |
| **sccm** | standard cubic centimeters per minute |
| **smNPCs** | small molecule neural progenitor cells |
| **STED** | stimulated emission depletion |
| **UV** | ultraviolet |

# Motivation and Scope of the Work

# 1

The human brain is the most capable and arguably the most fascinating organ in existence. All consciousness, perception, memories, thoughts and feelings we experience are the result of complex interactions between billions of neurons, interconnected by trillions of synaptic connections. Even though the structure of the human brain has been studied since the 19th century, unraveling of the exact mechanisms behind brain development and functioning is still considered to be one of the most important scientific challenges of modern times.[1] The importance of neuroscience for biomedicine and technological advance is reflected in a massive growth and development of the field in the last decades, culminating in huge research activities such as the EU Human Brain Project, the U.S. Brain Initiative and the Japanese Brain/MINDS project all over the world.[2] Non-invasive imaging techniques such as functional magnetic resonance imaging enabled detailed mapping of brain activity regions that are active during specific tasks and stimuli or in context to neurodegeneration.[3–5] However, due to poor accessibility of the vital brain for scientific research, which is particularly true for human brains, studying neuronal tissue on a cellular level is a challenge.[6] Even the very basic question of the average number of neurons and glial cells in the human brain has been a topic of debate in recent years, with approximately 86 billion neurons - 14% less than the long time assumption of 100 billion - and claimed numbers of glial cells that differ by more than an order of magnitude from each other.[7, 8] On the cellular and molecular level, the biochemistry of neural functions is well understood as a result of a wide range of studies on *in vivo* animal models and *in vitro* animal cell cultures.[9] Biological mechanisms such as the mechanism behind memory allocation in neuronal networks were uncovered. However, science is far from a complete understanding of neuronal circuits with high complexity and research on the topic is still at its beginning.[10, 11]

A central mechanism in the formation of complex neuronal circuits in the brain, both during development and for repairing damage through disease or injury, is axon pathfinding by growth cone guidance. As for many aspects in neuroscience, the biochemistry of axon guidance in correlation to chemical and topological factors is known, but scientific insight into its mechanics in a complex environment is still nascent.[12] The ability to manipulate or guide axonal path finding is crucial for bioengineering of defined neuronal circuits. Improved knowledge and control over axon outgrowth could lead to the development of diagnostics and cures for currently incurable and in part still poorly understood pathologies of the central nervous system such as Alzheimers's disease, multiple sclerosis or spinal cord injuries.[13]

Valuable tools to study neurons are *in vitro* cell cultures on artificial cell culture platforms. Axon pathfinding on these substrates can be influenced by a combination of chemical and topological cues. A range of surfaces with anisotropic and isotropic topographies such as grooved surfaces, tubes or pillars have been utilized as culture platforms to build ordered neuronal networks.[14] An example of a culture platform with rolled-up microtubes is shown in Figure 1.1 a. However, directed network formation is so far directionally limited to the two-dimensional (2D) space and therefore lacks the potential for increased complexity.[15] While several new techniques to produce three-dimensional (3D) environments for neuron culturing such as hydrogel platforms, micro breads, salt leached polymer scaffolds or microfibers have been presented in the last decade, these approaches only enable statistically oriented network formation. Artificial scaffolds need to offer axonal guidance in 3D on predetermined pathways for the design of sophisticated neuronal networks with specific circuit geometries.

Technologies such as grayscale lithography and reactive ion etching can be utilized to produce well defined modulated surfaces with topological features designed for network formation studies. Since cell culture platforms generated this way are basically large 2D plains with smaller 3D features, they will be called two-and-a-half-dimensional (2.5D) geometries in this thesis. While network formation can be studied beyond the 2D space with these approaches, they offer limited freedom in the design of guidance paths in 3D. Until recently, the realization of customizable architectures that are actually completely 3D has been limited to the macroscale. However, through advances in micro- and nanoscale fabrication, specifically direct laser writing (DLW) by two-photon polymerization (2PP), complex resist-based 3D scaffolds with feature sizes down to approx. 150 nm can now be fabricated. Nearly every mechanically stable computer-aided design (CAD), even with demanding inner geometries, can be translated into 3D polymer cell culture platforms.[16]

The technique of DLW by 2PP has already been utilized in a variety of neuronal growth studies. Most of these applications are designed with the goal

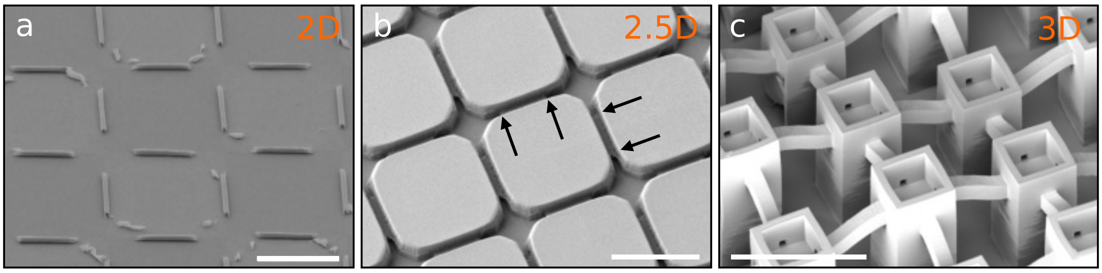

**Figure 1.1.:** Scanning electron microscopy images of cell culture platforms that utilize spatial confinement with the purpose of axon guidance. (a) GaAs/InGaAs heterostructure rolled-up microtubes arranged in a chessboard pattern, defining 2D pathways. (adapted from [18]) (b) Structure produced by reactive ion etching. The arrows point to steps between grooves and cavities, defining 2.5D pathways. (c) Pillar structure connected by free-standing tunnels produced with direct laser writing by two-photon polymerization. The tunnels can be freely arranged in all spatial directions, defining pathways in 3D. Scale bars: 50 µm.

to mimic the environmental structure in the brain, while the adhesion of cell somata and network formation is statistical. One single approach towards an application of DLW for neuro caging and axon guidance by Turunen *et al.* was published in 2014.[17] The presented structures, simple polymer boundaries on planar glass substrates enclosing small compartments connected by channels, were not efficient for cellular confinement, but demonstrated potential of printed channels as axon guides.

In this thesis, two different culture platform approaches are presented. First, as an intermediate step between 2D and 3D, geometries with the potential of 2.5D axon guidance are produced with grayscale lithography (GSL) and reactive ion etching (RIE) and duplicated with nanoimprint lithography (NIL) (Figure 1.1 b). Network orientation and axon paths of murine granular cells through grooves and over edges with varying height are analyzed. Second, for the first time, novel cell culture platforms for designer neuronal networks are produced using DLW by 2PP (Figure 1.1 c). These platforms have defined spots for cell adhesion and axon guidance on distinct pathways, whose design-specific course can be freely arranged in all spatial directions. The approach combines resolution and freedom of DLW scaffold fabrication with adhesion areas and axon outgrowth paths, predefined through topology and poly-D-lysine coating. The basis of the scaffolds are pillars of varying height. Cavities on top of the pillars serve as adhesion spots and neurocages. The pillars are connected to each other by freestanding tunnels, serving as contact guides for axon outgrowth. Successful site-specific attachment of murine granular cells and humane neurons derived from small molecule neural progenitor cells (smNPCs) inside the structures and axon guidance through the tunnels are shown.

The results presented in the thesis give new insight to neuronal behavior on 2.5D and in 3D cell culture platforms. The 3D culture platform presented is a proof of concept for future tailor-made *in vitro* neuronal networks with 3D complexity and introduces novel possibilities of neuronal circuit design.[19]

# Background to Neuronal Cultures

# 2

This chapter is the first of two chapters thought to introduce the theoretical background necessary in context of this thesis and focuses on the biological background. In the first three sections, neurons and neuronal functions are introduced, the mechanics of neurite path-finding are described and signal transmission through neuronal networks is explained. In the forth and fifth section, advances in the cultivation of neurons on artificial culturing platforms and in particular ordered neuronal networks with design-specific geometries are reviewed. In the final section of this chapter, characteristics of the cell types utilized for this thesis are introduced.

## 2.1. Neurons

According to current state knowledge, the human brain consists of 86.1 ± 8.1 billion neurons and 84.6 ± 9.8 billion glial and endothelial cells.[7] A mature mammalian neuron consists of the cell body, called soma, and cellular extentions, called neurites (Figure 2.1). The soma contains the nucleus and is the center of the cell metabolism. Neurites are categorized into two subgroups: axons, capable to propagate nerve signals away from the soma towards other neurons and dendrites, sensing and transmitting incoming signals towards the soma. A mature neuron can have multiple dendrites, but only one axon.

Axons in the central nervous system are insulated by several lipid-rich myelin sheaths formed by oligodendrocytes. In between the myelin sheaths are small free areas called nodes of Ranvier.[20, 21] Electrical signals propagate through neurons by opening and closing of voltage-gated ion channels in the cell membrane. In myelinated axons, the signal propagates through saltatory conduction from one node of Ranvier to the next. Propagation speed increases from 0.5 - 10 m/s in non-myelinated axons to up to 150 m/s in myelinated axons. The amount of sodium ions needed to conduct the signal is reduced to 1/300 compared to non-myelinated axons of the same dimension.[22–24] The length of axons in the human body differs largely depending on the type of neuron ranging from a few tens of microns to over a meter in sciatic nerves, which reach from the big toe to the base of the spinal cord.[25–27] Signal transduction to

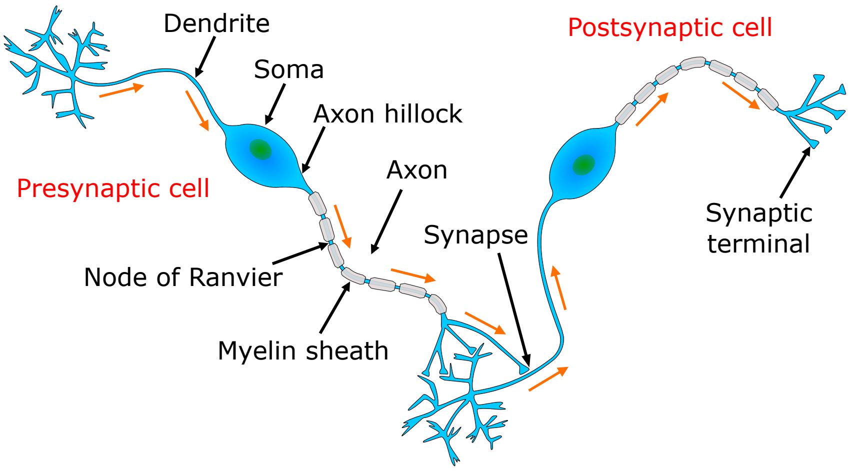

**Figure 2.1.:** Sketch of the basic structure of two connected neurons. In the displayed configuration, the left neuron is the presynaptic cell and the right neuron is the postsynaptic cell. A myelinated axon originating in the axon hillock of the left neuron is connected to dendrites and the soma of the right neuron through synapses at the synaptic terminals. The soma of the neuron contains the nucleus and other organelles responsible for the cell metabolism.

other neurons is realized through chemical or electrical synapses connecting the axon terminal to dendrites of other neurons. Each neuron can have thousands of synaptic connections to other neurons, building a complex network.[28]

Since the signal propagation through axon and synapses is unidirectional, one can distinguish between presynaptic cells - neurons which send signals - and postsynaptic cells - neurons which receive signals - in the discussion of specific synaptic connections. When a neuron receives signals from other neurons, these signals are transported towards the axon hillock, the transition area between soma and axon with an especially high density of voltage-gated ion channels.[29–31] If the summed signal exceeds a certain threshold, the signal is passed on through the axon in form of an action potential.[28] Depending on usage, synaptic strength between neurons is strengthened or weakened, a process called synaptic plasticity. These changes raise or lower the probability of signal propagation towards specific network directions.[32–34] Inactive synaptic connections can dwindle and new connections can be formed. This immensely complex cross-linking and flexibility is the root of the incredible cognitive processing capability of the brain.[11, 35]

## 2.2. Growth Cone and Neuronal Path Finding

In brain development as well as in *in vitro* cell cultures, prerequisite for the formation of any synapses and consequent neuronal network activity is the correct extension of axons towards other neurons. The central biological unit in the formation of neuronal networks are the growth cones, the motile tips of elongating axons (Figure 2.2).[36] In the developing brain, growth cones are guided over long distances along specific pathways to connect to designated targets.[37] Finding these targets is enabled by the special ability of growth cones to sense environmental cues, expand finger-like extensions called filopodia in that direction accordingly and thereby steering the elongation of the axon along specific pathways.[1][39]

The growth cone consists of two domains with very different properties, a stiff central (C) domain and a flexible peripheral (P) domain. The domains are separated by a transition (T) zone.[40] The C domain contains stable bundled microtubule offering structural support during axon elongation as well as serving as substrates for organelle, vesicle and actin transport coming from the axon shaft towards the P domain. The P domain consists of the finger-like filopodia containing polarized F-actin bundels and lamellipodia-like veils containing a less dense, more randomly oriented F-actin network. Some microtubules extend from the C domain into the P domain, where they are flexible and assemble or disassemble along the F-actin bundels as polymerization guides. In the T-zone, F-actin arcs lie perpendicular to the F-actin bundles, building a semicircle structure. [41, 42]

The pathway of axons in the brain is guided by a combination of substrate-bound and diffusible chemotropic cues. Adhesive substrate-bound cues can be located on the surface of other cells such as transmembrane cell adhesion molecules or proteins assembled in a dense extracellular matrix, such as fibronectin or laminin.[43, 44] Growth cone receptors adhere to these cues and signaling pathways are activated for further elongation in the growth cone. Anti-adhesive substrate-bound proteins, such as slits or ephrins, lead to withdrawal of filopodia upon contact. A wide variety of molecules can act as attractive or repulsive diffusible cues, such as netrins, morphogens, growth factors, neurotransmitters or secreted transcription factors.[45–50] The axon path finding in a controlled environment is sketched in Figure 2.2 b. The growth cone

---

[1] A video of *in vitro* axonal path finding on a substrate with rolled-up microtubes can be found online as supporting information for reference [38].

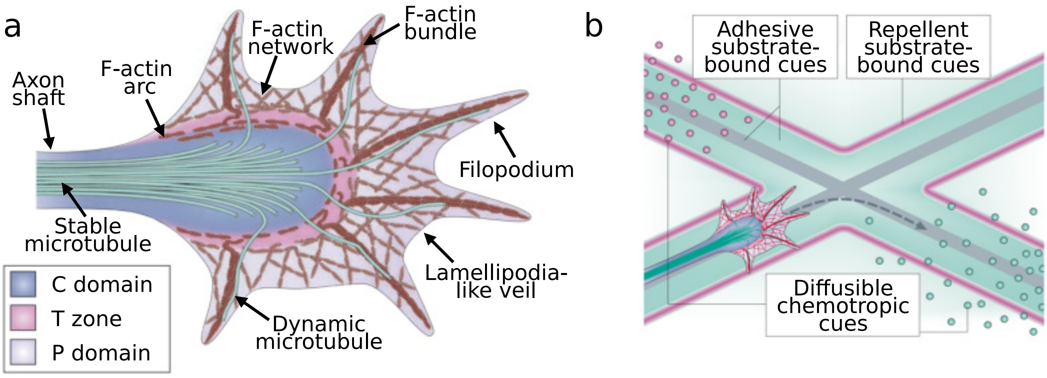

**Figure 2.2.:** (a) Sketch of the cytoskeletal organization of growth cones. Stable microtubule reach from the axon shaft into the C-domain. The F-actin arc builds the T-zone. Dynamic microtubule, F-actin bundle and a F-actin network build the P-domain, extending into filopodia and lamellipodia-like veils. (b) Effect of chemical guidance cues on axon path finding through growth cone navigation. Adhesive and repellent substrate-bound cues determine the general pathways, while diffusible chemotropic cues determine the direction within the limits of these possible pathways. (adapted from [41])

firstly follows the path defined by adhesive substrate-bound cues. Repellent substrate-bound cues act as boundaries of the possible pathway. Concentration gradients of diffusible cues guide the growth cone along a specific path.

Many details about axon guidance are not yet fully understood.[51] A lot of signaling and regulatory components still need to be discovered.[52, 53] Mechanisms such as endocytosis, exocytosis, membrane reconfiguration, -addition and -recycling that play an important role in growth cone navigation too, have to be further addressed in future studies.[54, 55] The topology of cultured substrates also plays an important role in axon guidance in *in vitro* studies, in some cases even dominating over the effect of chemotropic cues.[56]

The forward movement of the growth cone is usually described with three theoretical process stages. When the receptors bind to an attractive cue, intracellular signaling cascades are initiated, the actin cytosceleton binds to the substrate and the first stage, the protrusion is initiated. F-actin retrograde flow is attenuated while polymerization in front of the P domain at the leading edge continues. As a result, a traction force develops extending filopodia and lamellipodia-like veils forward, which moves the leading edge in the direction of the cue and leaves an actin-free space in the T zone between the adhesion spot and the C domain. In a second stage called engorgement, F-actin arcs reorientate. Guided by T zone actin arcs and C domain actin bundles, microtubules from the C domain extend into the free space moving the C domain forward while also invading the protrusions. In the last stage, the consolidation, proximal microtubules transition into a more condense arrangement and form a new axon shaft. F-actin formation in filopodia facing away from the new extention is suppressed and the filopodia regress. In reality, these stages are continuous and overlapping. For instance, when the cone is turning in one direction, the cytoskeleton can simultaneously extend on one side and retract on the other, leading to a left-right transitional polarity. [40, 41, 57]

## 2.3. Signal Transmission

After the axon of a premature neuron has been guided towards its target, the neuron maturates. The growth cone transitions into synaptic terminals.[58] The mature cell is now capable of the central skill of neuronal functioning - the ability to transport signals in form of action potentials. This section reviews the cellular mechanics of action potential propagation and the information transport from presynaptic to postsynaptic cells.

### 2.3.1. Action Potential Propagation

A difference in electric potential between the internal cell plasma and surrounding medium, separated by the cell membrane, is sustained by all cells. This membrane potential arises from a combination of concentration gradients (chemical force) between ions inside and outside of the cell and electrostatic gradients (electrical force) build up by ion migration due to selective permeability of the membrane. The main ions affecting the membrane potentials are potassium ($K^+$), natrium ($Na^+$), calium ($Ca^{2+}$) and chloride ($Cl^-$) ions. The equilibrium potential ($E_{\mathrm{ion}}$), individual for each ion at the point where the two opposing forces are exactly equal to one another, can be determined with the Nernst equation:

$$E_{\mathrm{ion}} = RT/zF \ln_{\mathrm{e}}([ion]_{\mathrm{outside}}/[ion]_{\mathrm{inside}}), \tag{2.1}$$

where $R$ is the universal gas constant, $T$ is the temperature, $z$ is the valence of the ion, $F$ is the Faraday's constant and $[ion]_{\mathrm{outside}}/[ion]_{\mathrm{inside}}$ is the gradient between the concentration of ions outside divided by the concentration of ions inside of the cell. $[ion]_{\mathrm{outside}}$ and $[ion]_{\mathrm{inside}}$ vary between different cell types,

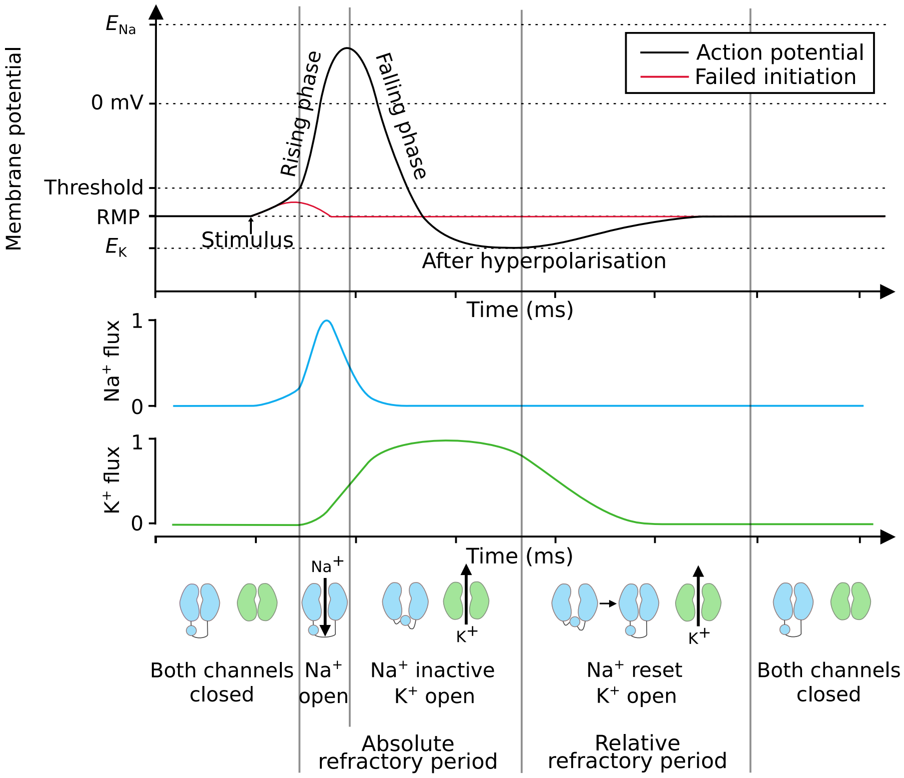

**Figure 2.3.:** Action potential and ionic current. The black trace shows a typical voltage curve $V_m$ of the membrane potential during an action potential. $E_K$ and $E_{Na}$, the resting membrane potential (RMP) and the threshold potential are marked by dotted lines. The red trace shows a failed initiation as a result of sub-threshold stimulation. The blue and green traces show the normed ion flux of $Na^+$ and $K^+$ through the membrane during the action potential, respectively. Sketches of conformational states of $Na^+$ channels (closed, open and inactivated) and $K^+$ channels (closed and open) are shown at specific times during the action potential. During the absolute refractory period, the cell is not excitable. During the relative refractory period, excitability is reduced.

but can be considered as constant regarding one specific type of cells *in vivo*. Since $T$ is also constant *in vivo*, $E_{ion}$ is also a cell type specific constant following Equation 2.1. The resting membrane potential (RMP) of a cell is the sum over $E_{ion}$ for all ions involved.

In contrast to other cells, rapid changes in membrane potential can be triggered in neurons and spread along the membrane. These electrical spikes are called action potentials (Figure 2.3). The most important ions involved in the distinct course of an action potential voltage curve are $Na^+$ and $K^+$. The lipid bilayer of a cell membrane by itself is not permeable to ionic flow. The concentration gradient and the resulting equilibrium between chemical and electric forces at the RMP is determined by ion flow through transmembrane ion pumps and voltage-gated selectively permeable ion channels.[59–61] While most ion channels involved in the action potential are closed at RMP, a large number of $K^+$ channels are open, leading to a membrane that is dominantly permeable to $K^+$ ions. Typical values of the RMP for neurons are therefore close to the $K^+$ equilibrium potential $E_K$, mostly in the range of about $-60\,\mathrm{mV}$ to $-70\,\mathrm{mV}$.[62]

When the membrane is depolarized by a postsynaptic channel or an action potential, the voltage sensor on voltage-gated $Na^+$ and $K^+$ channels moves to an active position that increases the probability of a conformational change to an open pore.[63] The conformational change in $Na^+$ channels is much faster than in $K^+$ channels.[64] If the incoming signal is too small to open a sufficient number of $Na^+$ channels, the influx of $Na^+$ ions does not surpass the resting $K^+$ efflux, which is called sub-threshold stimulation. The membran potential recovers towards the RMP and the signal is not propagated. When the critical threshold $Na^+$ influx is exceeded, it contributes sufficiently to the depolarization of the membrane to activate further $Na^+$ channels, starting a positive-feedback cycle. The membrane potential shifts towards the $Na^+$ equilibrium potential $E_{Na}$, which is about $+60\,\mathrm{mV}$, and switches from negative to positive value, which is called the rising phase. At positive membrane potential, the probability of $Na^+$ channels opening does not rise further. About 1 ms after stimulation, the $Na^+$ channels change their conformation to an inactive state, in which the pore is blocked and the influx of $Na^+$ decreases. Simultaneously, $K^+$ channel activation leads to an increase of $K^+$ efflux. As a result, the membrane potential enters a falling phase of repolarization. Such as the activation, the deactivation of $K^+$ channels is slower compared to $Na^+$ channels. Consequently, the membrane potential undershoots the RMP towards $E_K$. This fall below the RMP is called hyperpolarization.[62]

One aspect of action potential firing in neurons is the refractory period, being essential for controlled signaling and the unidirectionality of axonal signal propagation. In the absolute refractory period, beginning at the start of the action potential until shortly after hyperpolarization, $Na^+$ channels are first in the activated and then in the inactivated state, leaving the membrane inexcitable. Through hyperpolarization and time, $Na^+$ channels transition back from the inactivated form to the deactivated form. After hyperpolarization before the RMP is restored is a period of relative refractory. Even though the $Na^+$ channels are responsive again, an increased depolarization is necessary to trigger another action potential. When a signal is triggered in the axon hillock, a series of action potentials propagates through the whole length of the axon. Without the refractory period, an action potential in the middle of the axon could trigger signals forwards and backwards sending action potentials back towards the soma and causing chaos in the signal transduction through the neuronal network. With the refractory period, the action potential will always be followed by an unresponsive membrane, that only recovers by the time the action potential has moved on.[62] Furthermore, the refractory period ensures sufficient time for proper function of the chemical synapses.

### 2.3.2. Synaptic Signal Transmission

When an action potential reaches the terminal of an axon of a presynaptic cell, the signal can be passed to connected postsynaptic cells with two completely different transmission mechanisms: chemical and electrical synapses (Figure 2.4). Electrical synapses transfer depolarization of the membrane directly via ionic flow. In chemical synapses, electrical depolarization in the presynaptic cell is converted into a chemical signal that is converted back to an electrical signal by the postsynaptic cell. Typical neurons form >1000 synapses.[28] In the nervous system, chemical and electrical synapses cooperate and interact with each other. They even coexist in form of mixed synapses.[65]

#### Chemical Synapses

The majority of synapses are chemical synapses. The membranes of pre- and postsynaptic neurons are in close proximity to each other of distances between 15 - 25 nm. The gap in between is called synaptic cleft. Neurotransmitters are synthesized in the presynaptic terminal and contained in synaptic vesicles. A depolarization of the presynaptic membrane through an incoming action potential opens $Ca^{2+}$ channels. The concentration in the cytoplasm increases sharply and $Ca^{2+}$ ions activate proteins on the vesicle surfaces. As a consequence, the synaptic vesicles connect and merge with the membrane and the neurotransmitters are released into the synaptic cleft (exocytosis).[66, 67] Thus, the electrical signal of the action potential transforms into a chemical signal in form of neurotransmitters. The neurotransmitters diffuse inside the synaptic cleft and bind to ligand-gated channels in the postsynaptic membrane. Depending on the type of neurotransmitter, the ligand-gated channels either open or

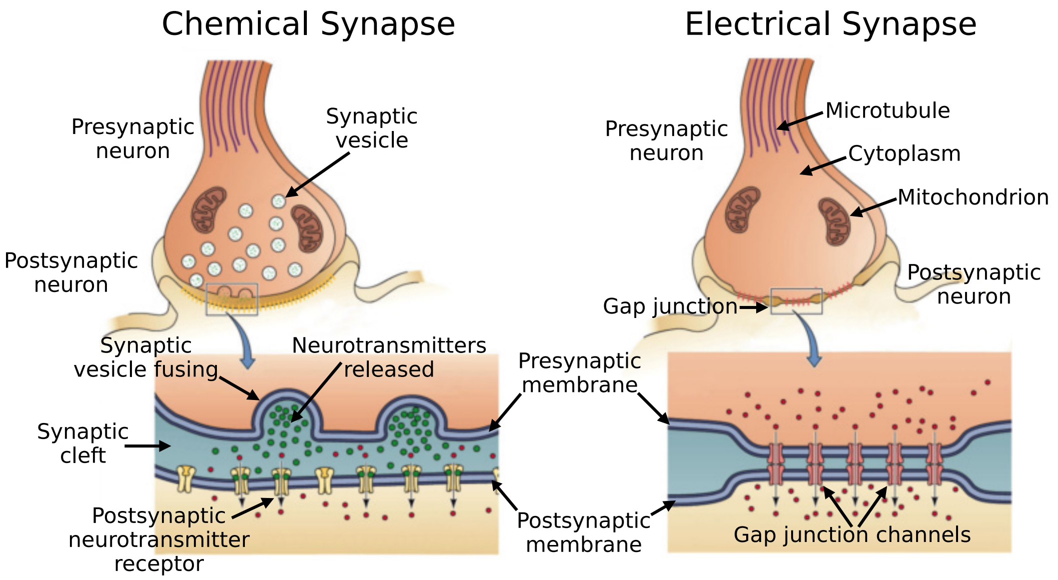

**Figure 2.4.:** Sketches of chemical and electrical synapses. Chemical synapse: Synaptic vesicles in the synaptic terminal of the presynaptic neuron fuse with the presynaptic membrane and release neurotransmitter into the synaptic cleft. The neurotransmitter bind to postsynaptic neurotransmitter receptors, leading to opening (or closing) of ion channels in the postsynaptic membrane. Electrical synapse: The membranes of presynaptic and postsynaptic neurons are in close proximity, forming a gap junction. Gap junction channels in both membranes are aligned to direct openings, connecting pre- and postsynaptic cytoplasm. (adapted from [68])

close, leading to increased or decreased membrane permeability to specific ions, which in turn depolarizes or polarizes the postsynaptic neuron. As a result, the likelihood of an action potential triggered in the postsynaptic neuron increases or decreases. Free neurotransmitters either diffuse out of the synaptic cleft, are broken down by enzymes or are reabsorbed by the presynaptic neuron.[68]

A big advantage of chemical synapses is that the intensity of a transmitted signal is scalable. Depending on the circumstances, the amount of neurotransmitters released from the presynaptic neuron and the number of receptors responsive to specific neurotransmitters is regulated. This capacity to strengthen or weaken synapses is called synaptic plasticity and plays a significant part in the ability of the brain to constantly change in response to all input and triggered activity.[67, 69, 70] One postsynaptic neuron is connected to a large sum of chemical synapses and receives multiple signals simultaneously. All these signals are transmitted towards the axon hillock. Only when the sum of all signals exceeds the threshold potential, an action potential is triggered and the signal is forwarded through the axon. Note, the influence of single synapses does not only depend on individual synaptic strength, but also on the positioning on the dendrites and soma, influencing timing and effect on to the overall signal reaching the axon hillock.[71, 72]

### Electrical Synapses

Even through being in the minority, electrical synapses are also present in the humane central nervous system (CNS).[73] A sketch of an electric synapse is shown in Figure 2.4 b. Pre- and postsynaptic neuron are linked together through so called gap junctions. At the gap junctions, the membranes of the neurons are in very close proximity, only about 3.5 nm apart. Transmembrane channels in both membranes are aligned to each other so that always two opposing channels form a pore that connects the cytoplasm of the two neurons, creating an electical continuity. With diameters of 1.6 - 2.0 nm, the pores are not only permeable to ions, but also to metabolites such as ATP and small second messenger molecules. When an action potential in the presynaptic neuron results in a high concentration of ions in the cytoplasm near the gap junction, the concentration gradient between the cells immediately leads to an ion current trough the gap junction into the postsynaptic neuron, thus directly transferring the depolarization. An advantage of electrical synapses over chemical synapses is the signaling speed. Due to the direct nature of the transfer, the synaptic delay is only a fraction of a millisecond. A disadvantage of the direct connections is a lack of scalability compared to chemical synapses. [68, 74]

## 2.4. *In vitro* Neuronal Cultivation

The foundation of modern neuroscience is the cellular and molecular understanding of neuronal functions and structures. The molecular knowledge we have today could not have been achieved without the ability to culture neurons and manipulate neuron growth and differentiation on a laboratory scale. Over the last century increasingly refined ways to study neurons *in vitro* have been developed, putting forth and answering increasingly complex and in depth questions.[75]

The first step towards *in vitro* neuron cultures was marked by Ross Granville Harrison in 1910.[76] He introduced a device with a hanging drop under a cover slip in which he was able to study outgrowth of nerve fibers taken from embryonic frogs. It was the first time, living tissue from vertebrates was extracted and cultivated *in vitro*. The research settled discussions about the nature of the nervous system by delivering the first incontrovertible prove that nerve fibers develop as extensions from cells. The significance to invent and refine methods for *in vitro* neuron culturing for further research became evident.[75, 76]

The hanging drop method was adapted in the same year to mammalian tissue.[77] The use of artificial media instead of lymphatic fluids enabled improved control over environmental conditions, an aspect still under optimization today.[78] Limitations of the hanging drop in regards to long-term and aseptic cell cultures drove innovation and many different techniques were presented in the following decade. The most significant steps were the introductions of callel flasks (1923, improving the stability of environmental conditions for prolonged viability)[79], roller tubes (1933, improving culture uniformity and media circulation for extended longterm cultures)[80, 81], culture chambers (1940, a multitude of designs for improved visualization and media exchange)[82], microisland cultures (1976, physical isolation of only a few cells to study cell-to-cell interactions)[83], brain slice chambers (1972, observation of thinly sliced brain slices, enabling research on specific regions closer to natural *in vivo* conditions)[84] and the Campenot chamber (1977, compartmentalization of neurons for selective exposure to chemicals)[85]. Over the last 30 years, a multitude of new technologies emerged, enabling the fabrication of patterned and specifically formed substrates with improved biocompatibility and chemotemporal control for neuronal culturing. Microelectrode arrays enable the detection of neuronal activity in complex micronetworks, microfluidic devices give spatiotemporal control over the culture environment.[75]

Besides the culturing method itself, the choice of the cell type also plays an important role in the success of culturing studies and the quality of information obtained. Mature neurons are challenging to culture, since they are sensitive to small environmental changes and do not undergo cell division. One often utilized approach is the use of secondary cell lines. These immortalized lines have been derived from neuronal tumors, resulting in infinite cell devision. These neuron-like cells are readily available for cell cultures and have minimal variability, which are useful properties for large-scale statistical evaluations. A disadvantage of cell lines are significant physiological differences to primary cells. Even when exposed to specific neuronal growth factors to adapt a more neuronal phenotype, research results can not directly be extrapolated to original primary cultures. The cultivation of primary neuron is hence still preferable, despite the challenges. Details to the primary neurons utilized in this theses are given in Section 2.6.1. A breakthrough in neuroscience of recent years is the development of cultivation protocols for neuronal cultures derived from stem cells. Stem cells have the advantage over primary cells to proliferate. Especially the introduction of pluripotent stem cells derived from somatic cells has had a great impact in neuroscience, introducing the possibility of *in vitro* studies on humane neuronal cultures, which is described in more detail in Section 2.6.2.[86]

## 2.5. Towards Designer Neuronal Networks

Precise control over the microenvironment introduced to neurons on artificial culturing platforms is not only important to study neuronal behavior and development properties, but has also enabled the design of neuronal networks with design-specific geometries and properties, which is important for regenerative medicine or studying computational properties of neurons.[87] An interplay of technological advances in physics and engineering with neuroscience has also paved the way towards functioning *in vitro* neuronal networks that in the future could work similar to electrical circuits with the advantage of synaptic plasticity - a goal described as a brain-on-a-chip.[88]

### 2.5.1. Surface Chemistry for Cell Adhesion

The most important factors in the design of ordered neuronal networks are the definition of locations for adhesion of the neuronal somata and neurites as well as the outgrowth direction or paths for axons. Cohesion of the neurons with the surrounding tissue in the brain as well as axon outgrowth are determined by proteins of the extracellular matrix. The main extracellular matrix proteins for neuron adhesion are laminin, fibronectin and collagen as well as lecticans in the developing embryonic and in the adult brain, respectively.[89] Naturally, the proteins of the embrionic brain have been shown to be useful as adhesion cues in *in vitro* cultures as well.[90, 91] Other molecules used for cell adhesion coating are polycationic polymers such as poly-ornithine and poly-lysine. These factors are non-specific to cellular functions, but enhance cell adhesion through ionic interaction with negatively charged side-chains in the cell membrane.[92] Coating molecules such as slits or semaphorins can have the opposite effect and repel cellular adhesion and outgrowth.[93, 94] These factors can be utilized to define substrate areas, where cell attachment and neurite outgrowth is not desired. Some cues such as netrins can trigger repulsion or attraction depending on the presence of specific other substances.[47, 94]

### 2.5.2. Chemical Guidance for Ordered Networks

Around the turn of the decade from the 60th to the 70th, first approaches were introduced to dissociate neural tissue, to fractionate the dissociated cells into homogeneous classes and to cultivate a selected class of neurons.[95, 96] The dissociation-fractionation-cultivation approach swiftly became the standard assay for the identification of molecules and substances related to neuron coherence and neurite outgrowth, and initiated the field of investigation regarding cell adhesion of various cell types with attachment cues such as poly-D-lysine (PDL) in Petri dish cultures.[97, 98] Using the gained knowledge, patterns of adhesive and non-adhesive molecules could be printed onto flat substrates to determine network structures. Results from exemplary patterning applications are shown in Figure 2.5. In a pioneering work from Kleinfeld *et al.*[99] from 1988, lines of adhesion promoting aminosilanes with adhesion repelling acetylsilans in between were defined on lithographically processed substrates (Figure 2.5 a). On lines with 10 µm width and 30 µm spacing, neurons reflect the pattern well two days after the cells were planted on the substrate - at 2 days *in vitro* (DIV). At 10 DIV pattern quality is less faithful with 30 µm spacing, but still good with 50 µm spacing. Soma migration leads to clustering along the lines. Much more practical than covalent binding of silanes is direct micropatterning of proteins, which was introduced in 2003 by Oliva *et al.* (Figure 2.5 b).[100] Poly-L-lysine and an L1-Fc chimera of the adhesion molecule L1 were printed in chessboard and line patterns with a line width of 2 µm. In direct competition, poly-L-lysine promotes soma adhesion, dendrite outgrowth and axon branching, while axon elongation is preferred along the L1-Fc lines. In 2012, Kwiat *et al.*[101] were the first to report on highly ordered long-term neuronal networks free of glia cells with low density to study individual cells in a network. A chessboard pattern (2 µm line width) was coated with PDL with fluorosilane everywhere else (Figure 2.5 c). Cells maintain order after 14 DIV without migration of somata into bigger clusters.

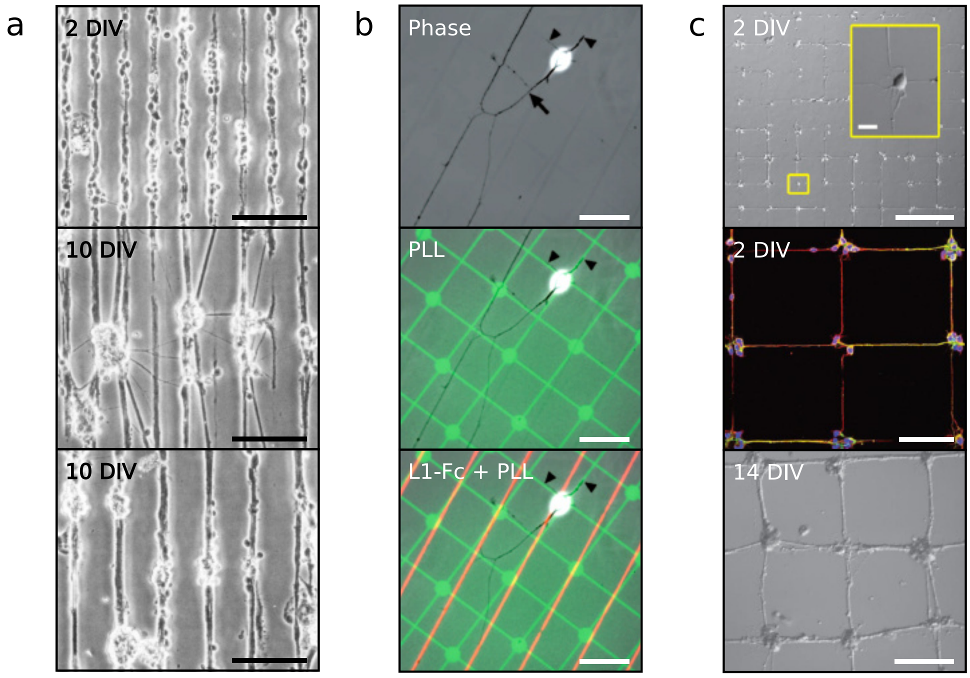

**Figure 2.5.:** Examples of ordered *in vitro* 2D neuronal networks. (a) Optical microscope images of cerebellar cells plated on silicon substrates patterned with different silanes promoting and preventing cell adhesion. Displayed are patterned lines with 10 µm width and 30 µm spacing at 2 DIV and 10 DIV and 50 µm spacing at 10 DIV. Scale bars: 100 µm. (adapted from [99]) (b) Optical microscope images of a hippocampal neuron adhered on a pattern of poly-L-lysine (green) and L1-Fc (red) with line width of 2 µm. Arrowheads point towards dendrites, the arrow points towards the axon. Scale bars: 50 µm. (adapted from [100]) (c) Optical microscope and confocal laser scanning microscopy (CLSM) images of low density cortical neuronal networks, predefined by a pattern of adhesive PDL and repellent fluorosilane at 2 DIV and 14 DIV. Scale bar of the insert is 10 µm. Scale bars: 200 µm, 75 µm, 50 µm. (adapted from [101])

### 2.5.3. Contact Guidance for Ordered Networks

Besides chemical guidance cues, contact guidance also plays a huge role in growth cone path finding and formation of guided *in vitro* neuronal networks. Modulation of the culture platform surfaces is often combined with specific or nonspecific application of adhesive cues.[102] A wide variety of surface modulated (2.5D) structures have been utilized to act as culture platform for guided neurite outgrowth, including variations in nanoscale surface topography,[103, 104] guidance barriers,[104, 105] 3D confinement in neurocages, grooves and channels,[**Taylor2005**, **Scott2012**, 17, 106, 109–113] microtube arrays,[18, 38, 114, 115] nanowires,[101] and nano- or micropillars.[116–120]

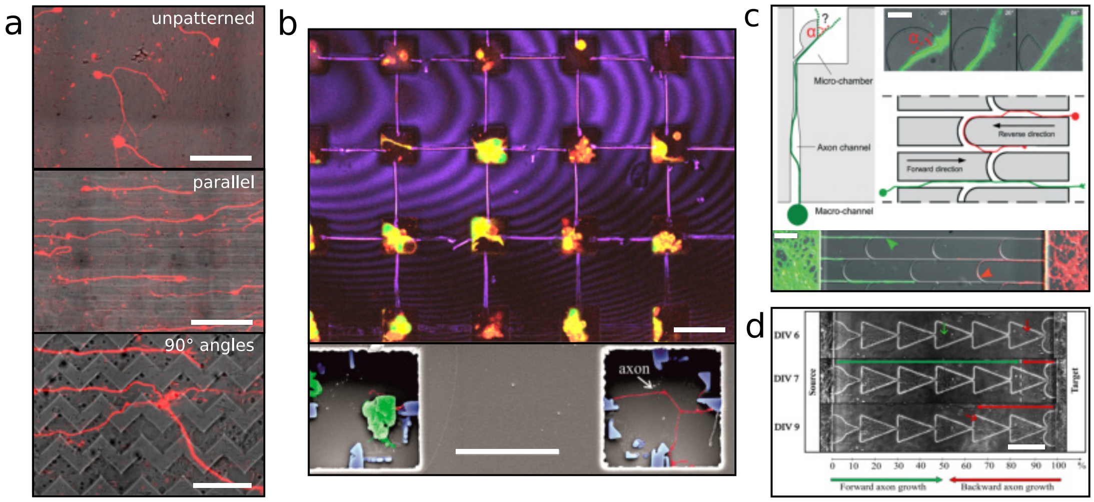

**Figure 2.6.:** Examples of directed neurite growth through topological guidance. (a) Fluorescence images of spiral ganglion neurons seeded on substrates for neural pathfinding on an unpatterned surface, parallel grooves and 90° angle grooves (14 µm depth). Scale bars: 200 µm, 200 µm, 100 µm. (adapted from [111]) (b) CLSM and scanning electron microscopy (SEM) images of murine cerebellar granule cells (MCGCs) at 4 DIV in cavities of 10 µm hight in a polymer layer. Neurite guides in form of rolled up microtubes connect the cavities to each other. Scale bars: 40 µm, 25 µm. (adapted from [115]) (c) Sketches and fluorescence images of microfluidic chips for neurite guidance. The left sketch and top images show a setup to test the angular dependence of edge guidance along corners. The right sketch shows a device that utilizes angular dependent edge guidance for unidirectional cortical axon growth in channels. The bottom image shows a chip at 2 DIV with two-chambers connected by such channels (10 µm width, 5 µm height) 16 h after seeding. Scale bars: 100 µm. (adapted from [113]) (d) Optical microscope images of a microfluidic chip with two-chambers connected by channels (7 µm height) for unidirectional hippocampal axon growth at 6 DIV, 7 DIV and 9 DIV. The shape of the channel favours axon growth from source to target and reduces the likelihood of axon growth in the opposite direction. Scale bar: 100 µm. (adapted from [121])

Some exemplary approaches to neurite guidance through topological constraints are highlighted in Figure 2.6. Modulating surfaces with grooves lead to strong alignment of neurites along unidirectional patterns (Figure 2.6 a). In grooves with multidirectional cues provided by periodic 90° turns, neurites cross features more often than in unidirectional patterns, leading to a reduced degree of alignment with more turns.[111] Interestingly, a different study found that introducing chemical cues laminin or immobilized nerve growth factor and topological cues in form of grooves as competitive stimuli, contact guidance is preferred over chemical guidance 70 % of the time.[56] Even stronger directional guidance is achieved by the introduction of channels with dimensions of a few microns which restricts an entering axon to one direction (Figure 2.6 b). Using a system of cavities and channels, where only a few soma settle per cavity, a low density neuronal network has been cultured with predefined orientation within the limits of the culture platform geometry.[115] If neurite outgrowth is required not only on defined pathways, but into one specific direction, channel arrangement can be adapted accordingly. The design presented in Figure 2.6 c utilizes the principles of edge guidance and critical release angles.[113] In rectangular channels, growth cones sense areas with maximal surface contact and primarily extend along the edges. Reaching a junction, where the edge has a change of direction, axons reliably follow the edge for directional changes with angles $\leq 26°$ and leave the edge to follow a straight path for angles $\geq 84°$. In a device utilizing this principle, arches with rectangular cross sections connect straight rectangular channels. The growth cones of extending axons encounters small and large angles depending on the direction of approach. Axons from one side extend along the straight channels, skipping the arches. Axons from the other side extend through the arches and effectively reverse their direction. A similar effect has been achieved by changes in channel geometry, where edge guidance along particular forms enhances or reduces the likelihood of the growth cone to reach a bottleneck, depending on direction (Figure 2.6 d).[121]

Overall, well defined neuronal networks with specific geometry have been constructed utilizing some of the various available technologies to prepare substrates for chemical and topological guidance. However, a drawback of the approaches discussed so far is the limitation of axon guidance in the lateral space, which is in contrast with the complex 3D environment presented to neurons in the brain.

### 2.5.4. Cell Cultures in 3D Geometries

*In vitro* neuronal cultures in 3D platforms is a new field of research. Diverse approaches include synthetic hydrogel platforms,[122–124] micro beads,[15, 125] porous polymer scaffolds fabricated by gaseous salt leaching or selective decomposition of vesicles through heat,[126–128] microfibrous scaffolds,[129, 130] three-dimensional graphene foam,[131] and scaffolds produced by DLW.[132] Most approaches are focused on mimicking the microenvironment of the brain. While some substrates such as fibers offer basic guidance, culture platforms with the ability to guide neurite outgrowth on specific pathways in 3D to build

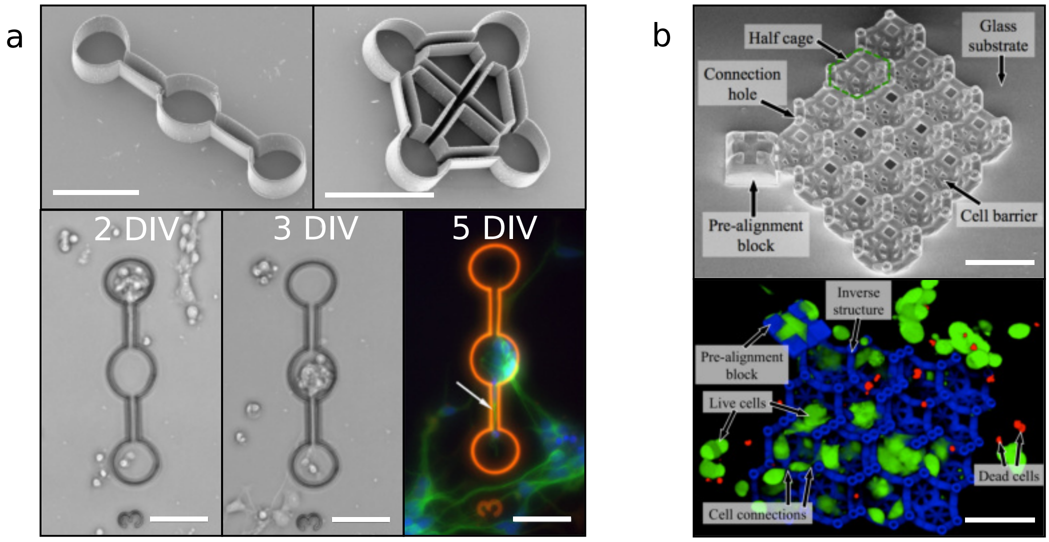

**Figure 2.7.:** Utilization of DLW by 2PP for neurite guidance and soma caging. (a) SEM, bright field and immunostained micrographs of neurocages. (adapted from [17]) (b) SEM and CLSM images of modular neurocages. (adapted from [133]) Scale bars: 50 µm.

neuronal networks with designed geometries analogous to the achievements in 2D have not been realized so far.

One technique for the construction of 3D culture platforms that stands out from the rest in its design freedom is DLW by 2PP: Utilizing DLW, CAD based structures with micron and sub-micron resolution are directly written into liquid droplets of photoresist. Due to the direct nature of DLW, complex scaffolds can be constructed with significant variations in local geometry. It is the only technique available nowadays to freely construct inner geometry. For a detailed review of the technique see Chapter 3.

Utilizing biocompatible polymers, DLW is well suited for the construction of a variety of cell culture platforms for various research applications. Scaffolds with variants such as woodpile, mesh, beam, pillar, cylinder, sea-shell or porous spherical unit cell structures offer distinctly different 3D microenvironments for cell adhesion, development and neuronal network building.[134–145]

In 2014, Turunen *et al.* published a first approach to utilize DLW by 2PP for the construction microstructures of physical confinement of soma adhesion and neurite outgrowth. (Figure 2.7 a).[17] Vertical boundaries were printed onto glass substrates to form nodes and channels. Cell somata were supposed to be confined in the nodes with neurites guided through the channels. The structures did not efficiently act as neurocages, were fragile and neurite guidance was only included in 2D, analogous to the approaches presented in Section 2.5.3, but with less efficiency. However, neuronal somata were attracted and the channels showed neurite guidance, indicating potential of the method for the construction of defined guidance paths. Neurocaging in 3D structures produced by DLW was targeted in a study published one year later by Larramendy *et al.* (Figure 2.7 b).[133] They used a modular design, where a second layer was stacked on top of a first layer after cultivation to create neurocages. While they confined somata of neuron-like PC12 cells successfully inside the structure, this approach does not offer prospects to include neurite guidance for structured networks. In summary, the potential for DLW by 2PP for the construction of neurocages with neurite guidance on distinct 3D pathways has been indicated, but not been explored before this thesis.

## 2.6. Utilized Types of Neurons

Two different kinds of neurons are utilized for growth studies in this thesis: Primary CNS neurons from the cerebella of mice - murine cerebellar granule cells (MCGCs) - and humane CNS neurons derived from stem cells - midbrain dopaminergic neurons (mDANs). Section 2.6.1 outlines, why MCGCs are especially well suited for ordered networks in *in vitro* cultures. Section 2.6.2 depicts background to the development of humane induced pluripotent stem cells (iPSCs) and small molecule neural precursor cells (smNPCs) as foundation for mDANs in culture. Section 2.6.3 introduces midbrain dopamine neurons and depicts the medical relevance of future research on mDANs.

### 2.6.1. Murine Cerebellar Granule Cells

Cerebellar granule cells are the smallest (soma approx. 10 µm diameter), most abundant neurons in the mammalian brain and by far the most numerous cells in the cerebellum.[147] They can be isolated from early postnatal cerebellar cortex. Even though neurites have already been formed at that time, they are destroyed in the dissociation process and the isolated neurons are spherical cells without extensions starting over neuronal development.[146] Many types of neurons such as hippocampal pyramidal neurons develop a multipolar morphology *in vitro* early on by initiating outgrowth of multiple neurites simultaneously and its roles as axons and dendrites are determined later in development. In contrast, MCGCs are first unipolar, with a single axon-like

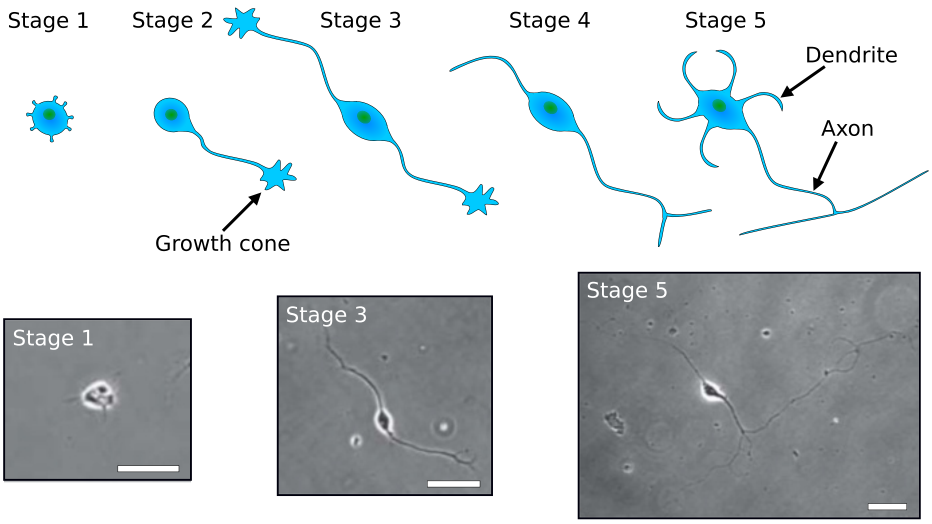

**Figure 2.8.:** Sketches and phase-contrast images of the early development of cerebellar granule cells. (a) Filopodia protrude from the soma (Stage 1) one axon with growth cone is extended (Stage 2), a second axon extends from the opposite side of the soma (Stage 3), one of the axons is further extended and branches (Stage 4) and finally, the second axon retracts and short dendrites are extended from the soma. (b) Images of a cerebellar granular cell at stages 1 , 3 and 4. Scale bars: 20 µm. (adapted from [146])

extension and then bipolar, with two long axons extending from opposite sides of egg-shaped cells (Figure 2.8). Eventually, one of the axons branches and the other axon retracts. At approx. 4 - 5 DIV, on average four short dendrites are extended from the soma.[148, 149] Mature axons of MCGCs are 0.3 µm on average in diameter.[150] *In situ*, each dendrite receives only a single excitatory mossy fiber input. Bipolarity early on in development, which results in moderate complexity of the cultured network, and a high sensitivity to small synaptic input currents, render MCGCs ideal systems for the study of neuronal network formation and the construction of defined, substrate specific networks.[146, 151]

### 2.6.2. Induced Pluripotent Stem Cells and Neural Progenitor Cells

One of the main goals in neuroscience is the development of therapies for neurodegenerative diseases. The molecular reason for many of these diseases still remains elusive. In the past, disease models had to rely on animal models - mostly rodent models - and immortalized cell lines. As a distinct disadvantage, especially in medical science, animal models can not adequately recapitulate human physiology and pathology. Hence, those research results can not directly

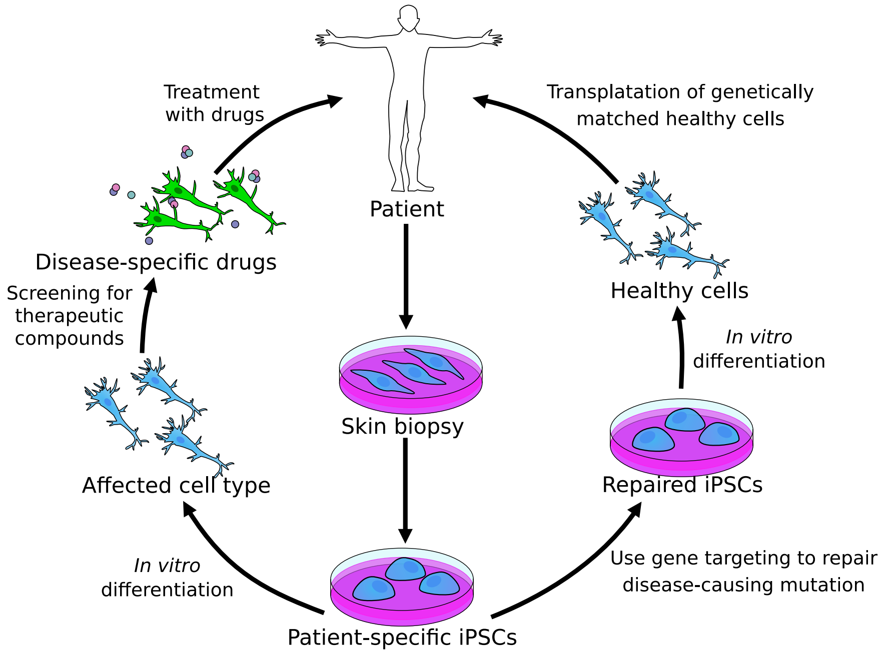

**Figure 2.9.:** Potential medical applications of iPSCs. Skin cells are taken from patients and differentiated *in vitro* into patient specific iPSCs through the introduction of specific genes. In one possible approach, these cells are differentiated into mature cells affected by a specific decease to screen for therapeutic compounds and to develop disease-specific drugs. In another approach, the iPSCs are differentiated *in vitro* to patient specific healthy cells, to be transplanted into the patients. (adapted from [157])

be applied to humans. As an example, the concordance rate of human toxicity in animal models in general was found to be 71 % overall and only 43 % specifically in rodents.[152] Results based on cell lines are also not directly comparable to those of primary cells.[153] Naturally, direct studies in humans are strictly regulated according to ethical guidelines.[154] Hence, it is difficult to source human neurons. Additionally, in contrast to cell lines, primary neurons are not expandable through cell devision. Thus, no human disease models have been available until recently.[155, 156]

In 2006, Shinya Yamanaka revolutionized the field with the introduction of iPSCs, a new class of immature stem cells reprogrammed for the first time from mature cells without the need of embryonic stem cells.[158, 159] He used the expression of only four genes to transform murine dermal fibroblasts into iPSCs which exhibit morphology and growth properties similar to embryonic stem cells - an achievement honored with the Nobel Prize in medicine 2012.[160] One year later, research results for humane iPSCs were published.[161, 162] Many optimizations have been developed since, which improve the iPSCs protocol

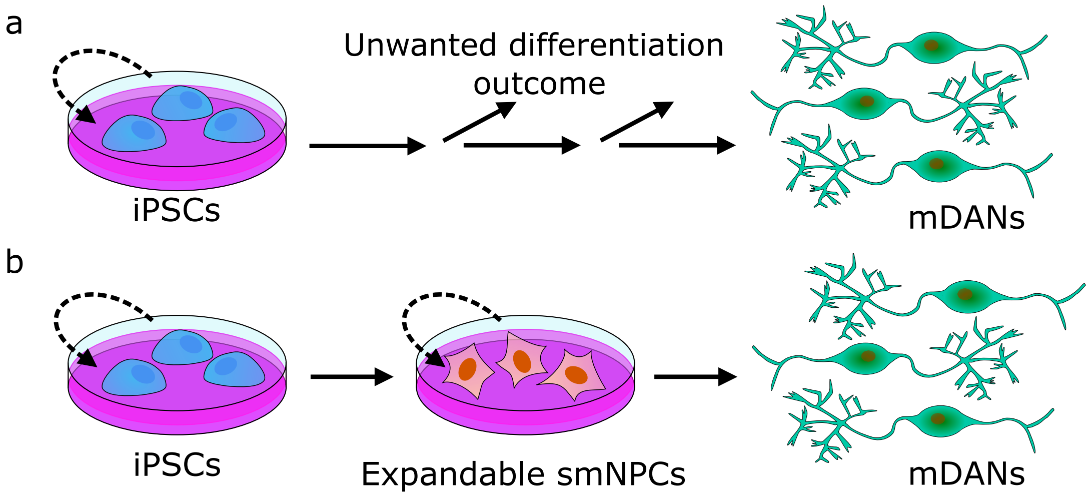

**Figure 2.10.:** Sketch comparing direct differentiation of iPSCs and differentiation of iPSCs into intermediate progenitor cells. (a) Direct differentiation of iPSCs into mDANs takes 1 - 2 months with manual selection steps, where unwanted diffentiation outcome has to be sorted out. (b) Expandable smNPCs derived from iPSCs do still proliferate and can be kept in a cell-line manner. Differentiation to mature cells takes 2 weeks without the need of manual selection. (adapted from [155])

significantly and enable differentiation into any type of human cell.[163–165] iPSCs have had major impacts to the fields of regenerative medicine, with the first clinical studies with humans already realized in 2014, and disease modeling and drug discovery (see Figure 2.9).[166–168] The discovery of iPSCs has huge implications for neuroscience, too. It is now possible to generate functioning humane neurons for *in vitro* studies and to develop human models for neurodegenerative diseases.[169–172]

Human neurons utilized in this thesis are mDANs that were differentiated from smNPCs according to a protocol introduced by Reinhardt *et al.* in 2013.[173] The usage of progenitor cells has considerable advantages over the direct differentiation of mDANs from iPSCs. Direct differentiation takes about 1 - 2 months, during which the iPSCs have to be exposed to a large amount of growth factors. Additionally, these protocols come with low efficiency and the need of many manual culture and selection steps. Only a small subpopulation of the total cell culture actually develops to mDANs and the unwanted outcome has to be screened out (Figure 2.10 a).[174, 175] Long culture cycles together with needed manpower and the consumption of consumables lead to a high cost for the procedure. The generation of mDANs from smNPCs is much less expensive and faster in comparison. The process does not require manual culturing and selection and is complete in 2 weeks, thus drastically reducing consumption of growth factors (Figure 2.10 b).[155, 173]

smNPCs are expandable intermediate stem cells derived from dermal fibroblast iPSCs using only small molecules. By adding small molecules (dorsomorphin and SB43152) to pluripotent stem cells, specific signaling pathways in the stem cells (BMP and TGFSS) are inhibited which induces neural differentiation. Different signaling pathways are simultaneously stimulated (WNT and Sonic hedgehog) by other small molecules (CHIR99021 and purmorphamine), ensuring the capability of immortal self-renewal. The resulting smNPCs are oligopotent towards different neural tube lineages. Without manual selection, these cultures form homogeneous colonies that can be split enzymatically and divide approximately once a day for more than 150 passages.[2] smNPCs are maintained as a cell line. Maturation into mDANs can be initiated whenever required (see Section 4.1 for details).[173]

### 2.6.3. Humane Midbrain Dopaminergic Neurons

Midbrain dopamine neuron is the term for neurons involved in dopamine signaling. Dopamine (2-(3,4-dihydroxyphenyl)ethylamine) acts as hormone and neurotransmitter. It is commonly known as the hormone for pleasure. The actual role of dopamine in the brain is more complex. As current state of knowledge, dopamine release in mDANs is modulated as a result of positive as well as negative stimuli and is thereby central in motivational salience, the process of adapting motivation and behavior towards specific goals.[176, 177] Besides reward processing, mDANs are also important for other key brain functions such as working memory and voluntary movement.[178] Particular relevance for biomedical research originates from their role in neurological diseases such as Parkinson's disease, dystonia and Huntington's disease.[179]

Humane mDANs derived from smNPCs have already been shown to be well suited for Parkinson's desease models. Mutations causing Parkinson's disease can be studied *in vitro*. Some essential genes and proteins contributing to degeneration of mDANs have been identified utilizing gene-correction and expression profiling.[175] Nevertheless, many details of midbrain dopamine functions is still unknown.[177] *in vitro* studies on humane mDANs could

---

[2] Passaging means spliting a culture of dividing cells and transferring the cells to fresh growth medium to produce new cultures with lower density. The passage number indicates how often a culture has been split.

play a central role in the understanding and development of treatments for neurodegenerative diseases.[175]

# Direct Laser Writing

3

This chapter introduces direct laser writing (DLW) by two-photon polymerization (2PP), an advanced fabrication technique that enables the production of high resolution 3D polymer scaffolds with features in the nanoscale range, which is utilized in this thesis for the development of a new type of culture platform for guided neuronal network growth. After a general overview, the physical and chemical principles of multi-photon absorption (MPA) and multi-photon polymerization (MPP) that enable DLW, as well as the advances and limits of the resolution of the technique are discussed. The last section gives an overview of cell culture platforms already realized with DLW with a particular focus on neuron cultures.

## 3.1. Basics

DLW by 2PP is a unique maskless lithographic technology. It enables the fabrication of true 3D structures based on CAD models with sub-diffraction limit resolution by translating the focal spot of a pulsed laser beam through photoresist or liquid resin (Figure 3.1). The energy of a single photon is not sufficient to start a polymerization reaction in the material. In other words, the resist or resin has a single-photon polymerization threshold above the laser frequency and is therefore transparent to the beam. However, the combined energy of two photons is sufficient to initiate a polymerization reaction based on two-photon absorption (2PA). Only at the focal spot, the energy density is high enough for two photons to be absorbed simultaneously.[180]

The basic principle of 2PA - two photons exciting a molecule from the ground state to the first excited state by simultaneous absorption - was already postulated in 1931 by Göppert-Mayer.[181] Thirty years after initial postulation, 2PA was applied in an experiment for the first time in 1961 by Kaiser *et al.* by generating blue fluorescent light ($\lambda = 425\,\text{nm}$) through illumination of $CaF_2{:}Eu^{2+}$ crystals with red light ($\lambda = 694.3\,\text{nm}$).[182] In 1965, Pao *et al.* published an article on the first experimental realization of the 2PP process.[183] However, technical limitations of UV lasers at the time prevented further significant development until the 90s.[184] In 1990, Denk, Strickler and Webb reported

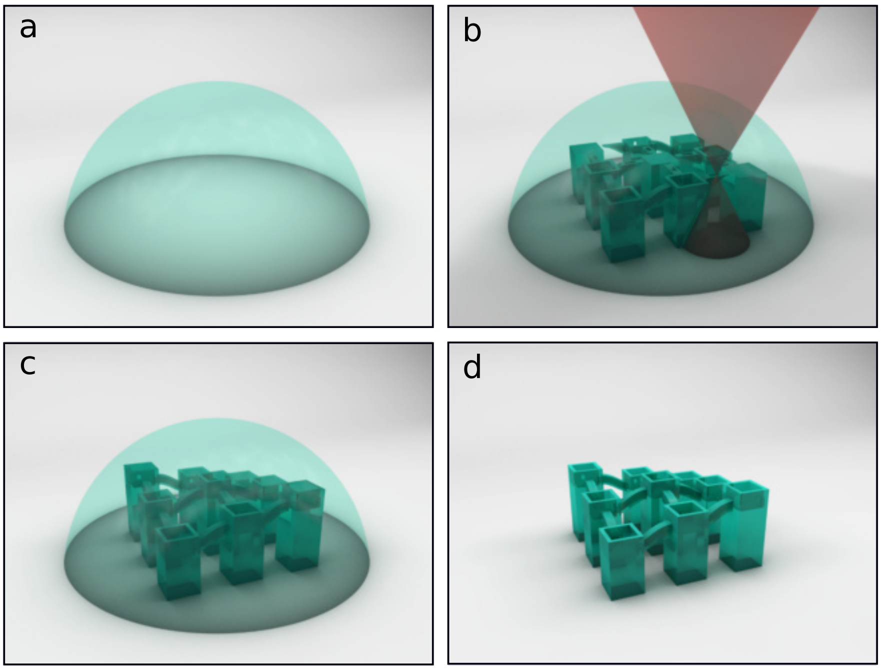

**Figure 3.1.:** Sketch of DLW by 2PP. (a) A droplet of liquid resin is placed on a glass coverslip. (b) A pulsed laser is focused into the resist. At the center of the focal spot, the resin is polymerized. Movement of the laser focus through the polymer in all directions results in a polymer scaffold with 3D features. (c) When the process is finished, the solid scaffold is covered with liquid resin. (d) The liquid resin is dissolved in a developer and the final structure remains on the glass carrier.

on two-photon scanning fluorescence microscopy, laying the foundation for a new field of high resolution imaging in biological studies.[185–187] One year later, a 3D polymer memory stack for optical data storage using 2PA was shown by the same group.[188] The first utilization of 2PA for microfabrication of true 3D structures was published seven years later in 1997 by Kawatas group, who produced spiral structures with features of 1.3 µm - 2.2 µm.[189] In 2001, they reported the next major development step in 2PP processing with sub-diffraction-limit resolution of 120 nm.[190] Today, 3D structures can be produced through DLW by 2PP with feature sizes of >100 nm with the minimum lateral feature size of 65 nm reported already over 10 years ago.[191–194] Even smaller structure sizes of 53 nm - 55 nm have been reported for DLW combined with stimulated emission depletion (STED).[195, 196] However, the development of STED lithography can still be considered to be at an early stage. It is reasonable to assume further improvement in feature resolution in the near future.[197]

Besides DLW, there is no other technology currently available that combines the property of sub-diffraction-limit resolution with the possibility to fabricate true 3D structures with complex inner geometry. On the one hand, other methods to fabricate complex 3D structures such as selective laser sintering, matrix-assisted pulsed-laser evaporation, 3D inkjet printing and UV laser microstereolithography only reach resolutions down to a few microns. With high resolution lithography techniques such as atomic force or electronic beam lithography on the other hand, it is impossible to construct geometries more complicated than basic 2.5D structures with high aspect ratio.[132]

Even though DLW is a relatively new technology, it has already been utilized for a wide variety of structures with diverse functionality. Devices have been fabricated in the fields of microoptics,[198–200], photonics[201–203] and metamaterials,[204, 205] microfluidics,[206–208] biomedical engineering,[209–211] as biomimetics,[212–214] micromachines,[215–218] and mechanical microstructures[219–222] and cell scaffolds.[144, 223, 224] Examples of the latter are discussed in more detail in Section 2.5.4.

## 3.2. Mechanism of Multi-Photon Absorption

The main principle behind the unique properties of DLW is MPA - the interaction of two or more photons with a molecule that is subsequently excited from the ground state to a higher state. The energy of the illuminating light is insufficient for direct excitation by one single photon. Two-photon absorption (2PA) is the most relevant case for DLW. Two mechanisms can be distinguished: sequential and simultaneous excitation (Figure 3.2). In the first case a real intermediate state becomes populated after the molecule absorbed a first photon. The lifetime of this intermediate state is usually between $10^{-9}$ s and $10^{-4}$ s. By absorbing a second photon in this time frame, the molecule is raised to an excited state.[225] In case of simultaneous 2PA, no such intermediate state exists. Instead, a virtual energy state is created through nonresonant interaction between photon and molecule. This virtual levels are the same as accessed in Rayleigh or Raman scattering and have a very short lifetime in the order of $10^{-15}$ s.[226] The lifetime of a virtual state is determined by the Heisenberg uncertainty relation.[227] Simultaneous 2PA is needed for 2PP of complex 3D structures. Thus 2PA stands for simultaneous absorption from here on out. Furthermore, it is important to distinguish between degenerate 2PA which is

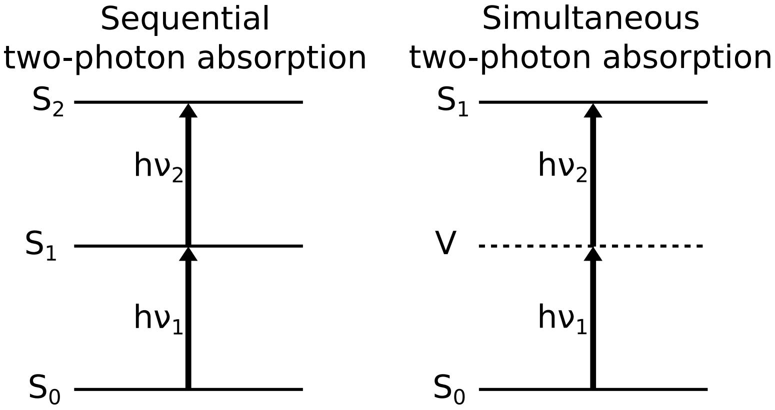

**Figure 3.2.:** Energy diagram of the mechanisms of 2PA. The excitation can be caused by either sequential or simultaneous absorption of photons. In sequential stimulation, a molecule first interacts with one photon and is exited to an actual intermediate energy level $S_1$ with a livetime between $10^{-4}$ s and $10^{-9}$ s and subsequently with a second photon to the excited state $S_2$. In simultaneous absorption, two photons interact with a molecule almost simultaneously within a time frame of $10^{-15}$ s, exciting the molecule over a virtual level V to the excited state $S_1$.

the absorption of two photons with identical frequency and non-degenerate 2PA which is the absorption of two photons with different frequencies. For most applications, degenerate 2PA is utilized.[228]

2PA is a nonlinear absorption process, in which the two photons need to overlap in the virtual state. An extremely high photon density is needed in order to reach a reasonable probability of 2PA. Figure 3.3 shows the methods applied to reach this prerequisite. Microscope objectives with high numerical aperture are used to reach a high spatial density at the focal spot. A pulsed laser with a pulse length in the order of femtoseconds is needed to ensure strong temporal photon density. Even when using a high-energy ultrashort pulse laser such as Ti:Sapphire laser, the photon density exceeds the absorption threshold only in a small area at the focal spot, which leads to improved 3D resolution of 2PA based microscopy and microprocessing compared to classical one-photon absorption (see Section 3.3).

Different approaches have been proposed to describe the process of 2PA theoretically. In order to get a complete quantum mechanical description, Doppler-free 2PA has been described based on the second-order perturbation theory.[181, 229, 230] Simpler models can be derived from the Heisenberg uncertainty relation and elemental statistics or the electrical susceptibility of

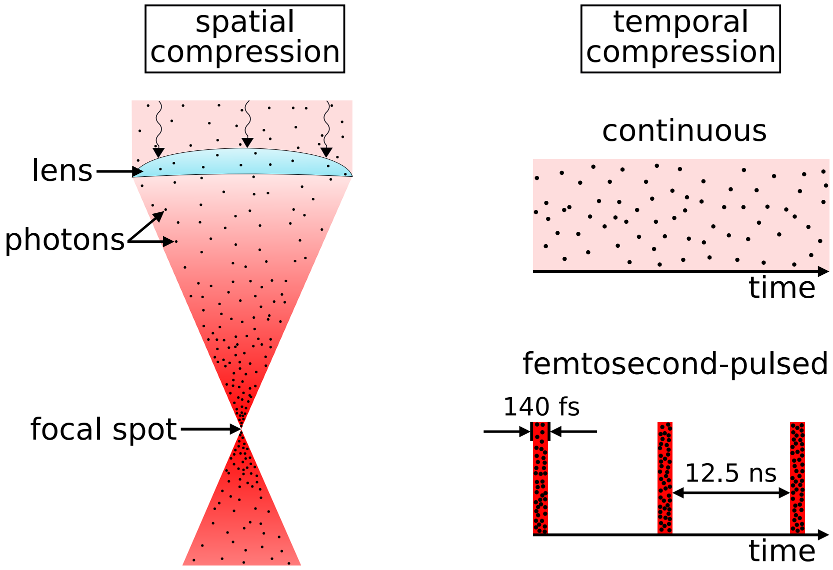

**Figure 3.3.:** Schematic of the two methods to reach increased laser photon density. (a) Objectives with high numerical aperture lead to spatial compression of photons at the focal spot. (b) Femtosecond-pulsed lasers with strong temporal compression of photons compared to continuous lasers are utilized. Adapted from [184]

polarized materials.[227, 228, 231] The later is a suiting approach to emphasize the nonlinearity of the 2PA process as it is connected to the imaginary part of the third order susceptibility.[228, 232] The derivation starts with the general expression for the polarisation of a material in an electric field $E$:

$$P = P_0 + \chi^{(1)}E + \chi^{(2)}E^2 + \chi^{(3)}E^3 + ... + \chi^{(i)}E^i, \tag{3.1}$$

where $P$ is the dielectric polarization density, $P_0$ static polarization, $\chi^{(2)}$ and $\chi^{(3)}$ the second and third order susceptibilities and $\chi^{(i)}$ the susceptibility of the $i$th tensor. Only odd tensors contribute to the resonant process when two photons with identical frequency are absorbed by a centrosymmetric molecule. $\chi^{(3)}$ combines nonlinear refraction $\chi^{(3)}_{\text{real}}$ and nonlinear absorption $\chi^{(3)}_{\text{imag}}$, therefore 2PA is connected to the imaginary part of $\chi^{(3)}$ and the corresponding rate of energy $\mathrm{d}W/\mathrm{d}t$ is:

$$\frac{\mathrm{d}W}{\mathrm{d}t} = \frac{8\pi^2\omega}{n^2c^2} I^2 \mathrm{Im}(\chi^{(3)}), \tag{3.2}$$

where $\omega$ is the incident light optical frequency, $n$ the refractive index, $c$ the speed of light, $I$ the light intensity and $\mathrm{Im}(\chi^{(3)})$ the imaginary part of $\chi^{(3)}$. Equation 3.2 shows a quadratical dependence of the 2PA rate on light intensity.

This mechanism leads to greatly improved spatial resolution compared to classical single photon absorption (see Section 3.4). The number of absorbed photons per unit time is defined as

$$\frac{\mathrm{d}n_{\mathrm{photon}}}{\mathrm{d}t} = \sigma_2 \mathrm{N} F^2, \tag{3.3}$$

where $\sigma_2$ is the 2PA cross section, $N$ the density of molecules and $F$ is the beam flux, which is defined as $F = I/h\nu$, where $h\nu$ is the photon energy. Since the rate of energy in Equation 3.3 equals the number of absorbed photons ($\mathrm{d}w/\mathrm{d}t = \mathrm{d}n_{\mathrm{photon}}/\mathrm{d}t$), the 2PA cross section can be described with Equation 3.3 as

$$\sigma_2 = \frac{8\pi^2 \mathrm{h}\nu^2}{n^2 \mathrm{c}^2} \mathrm{Im}(\chi^{(3)}). \tag{3.4}$$

This model is useful to understand the physical properties related to 2PA. Yet another simplified model, which is focused on the chemical reaction in the molecule with excitation as rate-limiting step, is better suited to illustrate the technical requirements for 2PA.[226] Starting from the simple photochemical reaction

$$\mathrm{N}_0 + 2\mathrm{h}\nu \longrightarrow \mathrm{N}_1, \tag{3.5}$$

where simultaneous interaction with two photons $h\nu$ promotes the ground state $\mathrm{N}_0$ to the first excited state $\mathrm{N}_1$, the rate of production of excited-state molecules is

$$\frac{\mathrm{d}[\mathrm{N}_1]}{\mathrm{d}t} = k[\mathrm{N}_0][\mathrm{h}\nu]^2, \tag{3.6}$$

where $k$ is the rate coefficient, $[\mathrm{N}_0]$ is the concentration of molecules at ground state, $[\mathrm{N}_1]$ is the concentration of molecules at first excited state and $[\mathrm{h}\nu]$ is the concentration of photons involved. Equation 3.6 can be transformed into an expression for the rate of two-photon absorption $R_{2\mathrm{PA}}$. For that purpose, the speed of light is defined as $\mathrm{c} = \mathrm{d}x/\mathrm{d}t$, the interaction volume of excitation is defined as the focal spot path length $l$ multiplied by the focal spot cross sectional area $A$, the two-photon cross section is defined as $\delta = 2k/\mathrm{c}^2$, the number density is changed to molar concentration $C = \mathrm{N}_0/\mathrm{N}_\mathrm{A}$ with the Avogadro constant $\mathrm{N}_\mathrm{A}$, the concentration of photons $\mathrm{h}\nu$ is converted to laser power $P$ and the equation is divided by 2, since two photons are absorbed in the process:

$$R_{2PA} = \frac{\delta}{2}\frac{l}{A}CP^2. \tag{3.7}$$

In case of pulsed lasers, $P$ is the product of peak power $P_{peak}$ and average power $P_{ave}$, where pulse width $\tau$ and pulse repetition frequency $f$ are taken into consideration:

$$P_{ave} = P_{peak} \times \tau \times f \tag{3.8}$$

and

$$R_{2PA} = \frac{\delta}{2}\frac{l}{A}CP_{peak}P_{ave} = \frac{\delta}{2}\frac{l}{A}C\tau f P_{peak}^2. \tag{3.9}$$

Taking the quantum yield $\Phi$ of the reacting molecules into consideration, the magnitude of the 2PA-induced reaction can be sufficiently estimated using Equation 3.9, taking into account the properties of the laser as well as the concentration and absorption cross section of the reacting molecules.[226, 233]

## 3.3. Multi-Photon Polymerization

The main application of MPA processes besides high resolution fluorescence imaging is the construction of detailed 3D structures from liquid photoresist or resin in a MPP reaction. Typically, the two main components involved are a photoinitiator and a monomer. The absorption cross section, which is given in Equation 3.4, defines the efficiency of the photoinitiator in simultaneous absorption of multiple photons, one of the most significant parameters for MPP.[184]

Chemically, MPP is a classical polymerization process with initiation, propagation and termination. It is initiated when an initiator molecule I decomposes into two radicals R as a result of MPA. Subsequently, these radicals react with monomer- and oligomer molecules M. The new radicals RM become part of a chain reaction until the reaction is terminated when two radials meet and react with each other.[184, 189]

$$\begin{array}{ll}
\text{Initiation:} & \mathrm{I} \xrightarrow{2h\nu} 2\,\mathrm{R}^\bullet \\
 & \mathrm{R}^\bullet + \mathrm{M} \longrightarrow \mathrm{RM}^\bullet \\
\text{Propagation:} & \mathrm{RM}_n^\bullet + \mathrm{M} \longrightarrow \mathrm{RM}_{n+1}^\bullet \\
\text{Termination:} & \mathrm{R}^\bullet\mathrm{M}_n + \mathrm{R}^\bullet\mathrm{M}_m \longrightarrow \mathrm{RM}_{n+m}\mathrm{R}.
\end{array}$$

A variety of chemicals can additionally be mixed into the MPP system. Photosensitizers increase efficiency by transferring 2PA excitation energy to photoinitiators through fluorescence.[228] Inhibitors influence the polymerization threshold. Additives such as metal nanoparticles, quantum dots or fluorophores give specific functionality to the polymer.[184] For example, a cationic silver(I) complex has been shown to act as efficient free radical two-photon initiator, enabling the direct fabrication of structures by 2PP composed of metal-polymer nanoparticle composites.[234]

It is important to note, that mechanisms different to pure 2PA have been discussed for 2PP, in particular multi-photon ionization with subsequent avalanche ionization[235] and heat accumulation[236, 237]. However, the influence of these mechanisms on DLW is still under discussion. Fischer *et al.* found that for commonly used DLW setups - such as the one utilized for this thesis - with femtosecond laser pulses and repetition rates above 100 kHz, two-photon absorption rates estimated on the basis of literature cross section values and threshold-scaling perfectly fit the theory of polymerization based solely on 2PA.[238]

## 3.4. Feature Size and Resolution

The biggest advantage that differentiates DLW by 2PP from other available methods for 3D fabrication is an unparalleled sub-diffraction minimum feature size, which is also significantly improved compared to one-photon polymerization (1PP) lithography. Note, it is important to distinguish between feature size and resolution, the first being the width of an isolated line or dot that can be achieved with the next feature in at least a few wavelength distance, and the second being defined as the minimum spacing at which features are completely resolved and separated from each other.[195]

### 3.4.1. Feature Size

To completely understand the limits of feature size and resolution, one must consider the physics and chemistry of the 2PP process. The laser beam can be assumed to have a Gaussian intensity profile given by

$$I(r) = I_0 \exp(-2r^2/\omega_0^2), \tag{3.10}$$

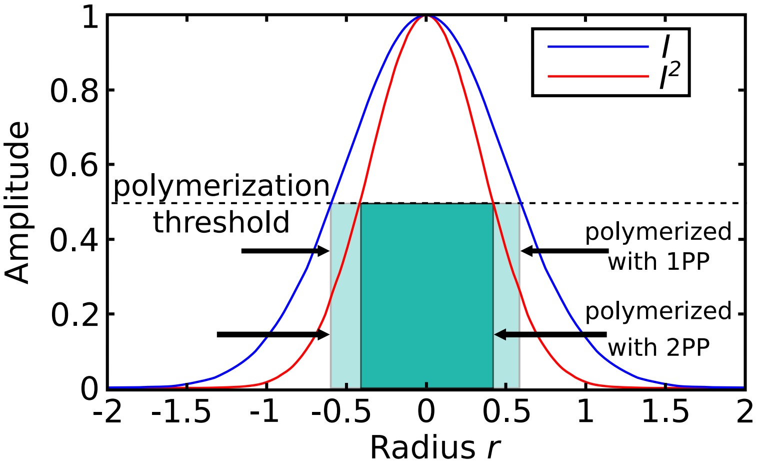

**Figure 3.4.:** Plots of the amplitudes of intensity $I$ (blue) and squared intensity $I^2$ (red) against the radius at the focal point of a Gaussien laser beam. The radius $r$ of $I^2$ is smaller at the threshold intensity for polymerization than the $r$ of $I$, resulting in a smaller polymerized region of 2PP compared to 1PP. (adapted from [239])

where $I(r)$ is the local intensity, $I_0$ is the photon flux intensity at the focus point center, r is the distance from the center and $\omega_0$ is the beam waist. The formalism of 2PA as a non-linear process has been established in Section 3.2. 2PP therefore depends on the squared intensity $I^2$ (see Equation 3.2 and Equation 3.9). Normalized $I$ and $I^2$ with $I_0 = 1$ and $\omega_0 = 1$ of an ideal Gaussian laser beam are shown in Figure 3.4. For fixed exposure times, the width of polymerized area in the resist depends on $r_{\text{threshold}}$ of $I$ for 1PP and $r_{\text{threshold}}$ of $I^2$ for 2PP, which results in a smaller feature size for the non-linear process.[239]

The 3D volume of the intensity profile at the focal spot is called voxel. The probability to initialize radicals is highest at the center spot of the voxel and steadily decreases over its radius, due to its Gaussian shape. The 2PP threshold of the voxel is defined as the intensity limit where the degree of polymerization is sufficient to produce a solid phase that withstands the later development process.[240] Even though the photoresist in direct vicinity to a voxel is not solid, it consists as a result of a lower degree of polymerization not only of monomers and initiators, but also a mixture of oligomers and radicals. Increasing the laser power or exposure time expands the voxel as a result of radical diffusion. Active dangling ends of polymers in the voxel react with further monomers and continue the chain reaction (see Section 3.3). While radicals can also meet the dangling ends and terminate the polymerization process, oligomers and long-chain radicals forming the liquid phase can get entangled or encapsulated in the elongated ends and added to the voxel size.[239, 241]

Reduction of the voxel dimensions is physically not limited. Optical systems with small numerical aperture, ultra short laser pulses and focal intensity that barely exceeds the 2PP threshold at $r = 0$ can be utilized. However, in order to start a chain reaction, the photoresist must contain a critical amount of initiator molecules, which also influences threshold behavior and limits the theoretical smallest feature size.[242] Additionally, real laser do not emit a perfectly constant flux. Small fluctuations of laser power have a big impact on feature width when the maximal intensity barley exceeds the polymerization threshold, resulting in uneven results. While different photoresist differ in tolerance to exposure dose fluctuations, the accessible minimum line width for consistent results is typically about 40 % of the 2PA profile's full width at half maximum (FWHM).[195, 232, 243]

### 3.4.2. Resolution

Since DLW is a serial process with threshold behavior, one could assume, that voxels can be duplicated in arbitrary proximity to each other, enabling sub-diffraction limit resolution with possible spacing between two lines even smaller than the line widths. There would be no fundamental difference between feature size and resolution in that case. As stated in the preceding paragraph, the real threshold is not a hard border, but sub-threshold polymerization occurs close to the voxel, changing the composition of the photoresist. Sequential exposures therefore accumulate instead of being fully independent. As a result, the resolution is fundamentally limited by the Abbe diffraction limit. The Abbe condition in optical microscopy states

$$a_{\mathrm{xy}} \geq \frac{\lambda}{2n \sin \alpha} = \frac{\lambda}{2\mathrm{NA}}, \tag{3.11}$$

where $a_{\mathrm{xy}}$ is the minimum lateral resolvable distance, $\lambda$ is the laser wavelength, n is the refractive index of the material, $\alpha$ is the half-opening angle of the incident light cone and NA is the numerical aperture of the objective.[244] The Abbe condition is closely correlated with the Sparrow resolution limit, which states that two separate lines will resolve in microscopy when the combined signal has a local minimum in its center.[245] Assuming a linear accumulation of sequential exposures, which means the complete dose is remembered by the resist, the squaring of the profiles in 2PP would directly translate into an im-

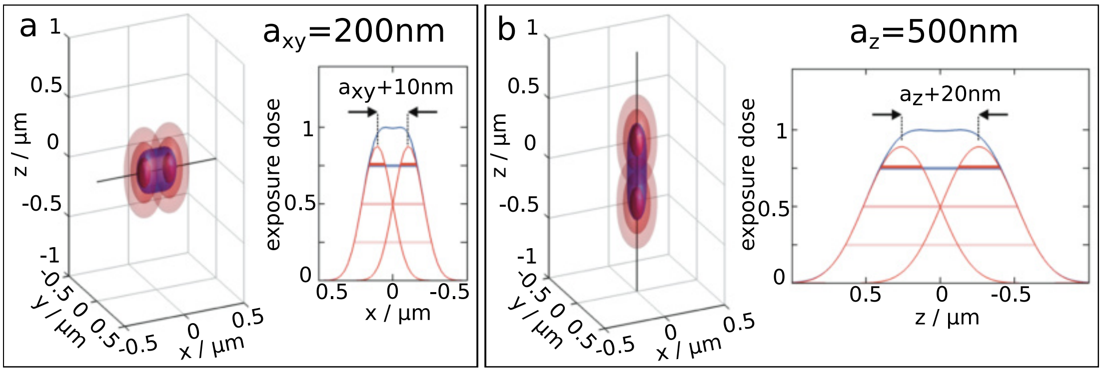

**Figure 3.5.:** Resolution of two-photon polymerization according to the Sparrow criterion. (a) The iso-intensity plot shows two exposure dose profiles with a spacing slightly above of the minimal lateral spacing of $a_{xy} = 200\,\text{nm}$. The normalized exposure doses along the black line are plotted on the right-hand side.(red) A typical polymerization threshold value of 75 % The distance is $a_{xy} + 10\,\text{nm}$ for improved visualization of the local minimum in the center of the sum of the profiles (blue). (b) Plots analogous to (a) for two voxels in axial proximity of $a_z + 20\,\text{nm}$ with $a_z = 500\,\text{nm}$. (adapted from [243])

proved resolution by the factor of $\sqrt{2}$ compared to 1PP. Adapting Equation 3.11 for 2PA results in

$$a_{xy} \geq \frac{\lambda}{2\sqrt{2}\text{NA}}. \tag{3.12}$$

Fischer and Wegener calculated the theoretical minimum resolution based on this model using $\lambda = 800\,\text{nm}$ as laser wavelength and NA= 1.4.[243] In their calculation, the minimum spacing is reduced to $a_{xy} = 202\,\text{nm}$ for 2PP from $a_{xy} = 286\,\text{nm}$ for 1PP. These values are nearly identical with calculations applying the Sparrow limit to the squared electrical-field vector $|\text{E}|^2$ for 1PP ($a_{xy} = 288\,\text{nm}$) and $|\text{E}|^4$ for 2PP ($a_{xy} = 200\,\text{nm}$). The Sparrow limit of $a_{xy}$ for 2PP is schematically shown in Figure 3.5 a. The plot displays a distance of $a_{xy} = 210\,\text{nm}$ to visualize the minimum in the combined two point exposure.[243]

Another factor to note is the ellipsoidal shape of the voxel, which is intrinsic and can not be changed significantly through technological adjustments.[246] The FWHM in axial direction are elongated by a factor of 2.45 - 2.52. Minimum feature size and resolution in that direction are elongated by the same factors. Equation 3.11 can therefore be further modified for the resolvable distance in axial direction $a_z$:

$$a_z \geq \frac{\lambda A}{2\sqrt{2}\text{NA}}, \tag{3.13}$$

where $A$ is the aspect ratio of the focal spot. Using the same criteria as for

$a_{xy}$, the result ($a_z = 505\,\text{nm}$) is once again close to the calculation using the Sparrow limit ($a_z = 500\,\text{nm}$), displayed in Figure 3.5 b. It should be noted, that the actual resolution limit is highly dependent on the choice of photosensitive material and often above the physical limit provided by the utilized DLW system. High-resolution photoresist is needed for optimal results near the resolution limit.[232]

The resolution limit can be further reduced, by optimizing the process, for example with the use of shorter wavelengths in the visible region. However, as long as two exposures in sequential exposure are not completely independent, the diffraction limit will apply to the 2PP process.[243]

### 3.4.3. Shrinkage and Breakdown

A practical disadvantage of 2PP is shrinkage of written structures during development. Even though, the structure is solidified where $I^2$ exceeds the polymerization threshold, the polymerization yield is not at 100%. Especially when a structure is written with low ${I_0}^2$ close to the threshold, many monomers and oligomers will dissolve out of the polymer, resulting in a contraction of the structure, called shrinkage. Shrinkage leads to distortion of structures and the result will not meet the dimensions of the CAD design. For instance, in case of cubical structures which have the base firmly attached to a carrier material, shrinkage will lead to a trapezoidal shape, since, in contrast to the top of the structure, shrinkage of the bottom layer is prevented. This leads to strain in the material.[240]

To solve the problem of deformation, the shrinkage can be taken into account while creating the CAD in form of numerical compensation. In the example of a cubical structure as target, one needs to prepare a top-heavy trapezoidal design exactly countering the amount of shrinkage.[240] Other approaches to the problem include multi-anchor support and single-anchor support combined with supercritical $CO_2$ drying.[247, 248] The ratio of polymerized to dissociable resist depends on the intensity of the exposure. The shrinkage is significantly reduced utilizing higher laser power. As a trade off, resolution is smaller and the minimum feature size increases.[248]

When the laser intensity exceeds a certain value, the polymer is damaged in so-called laser-induced breakdown. Analogous to the polymerization threshold, each material has an individual breakdown threshold. The process window between the thresholds is relatively narrow and does not offer much freedom for adjustments of ${I_0}^2$.[232, 240, 249] Above the breakdown threshold a plasma is generated in an avalanche process, in which the density of free electrons rises abruptly at the focus point. As a result, microexplosions in the material locally destroy the resist molecules. Vaporization of the material leads to gaseous bubbles in the resist that damage polymerized structures and defocus incident light preventing further 2PP reactions.[232]

### 3.4.4. Stimulated Emission Depletion (STED)

Lateral as well as axial sub-diffraction limit feature size and resolution have been achieved by the combination of DLW by 2PP with STED.[195, 196, 250] STED circumvents the limitations given by diffraction resolution with the introduction of a depletion laser.[251] In combination with DLW, STED inhibits the polymerization chain reaction by reduction of the photoresist sensitivity in the exposed area.[252, 253] The depletion laser is usually focused in a donut-shaped profile surrounding the focus spot lateral and a bottle-beam profile entrapping the focus spot from top and bottom. With this arrangement spherical sub-diffraction voxels can be achieved.[243]

While the possibilities provided by STED have been well established in confocal imaging of biostructures [254, 255], STED lithography has not yet reached commercial status. Even though sub-diffraction resolution is a significant technological achievement, the addition of STED to the DLW process is not only technically demanding, but also slows down the writing process significantly. Writing speeds up to 90 µm/s that have been reported for high-resolution structures produced utilizing STED are not feasible for the production of large-scale scaffolds with dimensions that surpass a few tens of microns.[195, 250] For comparison - 3D structures for this thesis were produced with DLW speed of 10 - 20 mm/s.

# Experimental Methods

# 4

In this section, the protocols utilized for cellular culturing and the methods for subsequent analysis of the cell cultures are concisely introduced.

## 4.1. Cell Cultivation

Two profoundly different neuronal cell types are utilized during the course of this thesis. Most research on the formation of *in vitro* neuronal networks is conducted using primary cell cultures, more precisely wild type MCGCs (introduced in Section 2.6.1). Isolation of the granular cells, described in detail in the following paragraph, closely follows the description given by Loers *et al.*[256] For details on the preparation of the solutions and the culture medium, and for further information regarding the bred mice, see Appendix A.

The second cell type utilized are mDANs differentiated from humane smNPCs (see Section 2.6.1). Further details regarding the derivation of smNPCs from iPSCs and background information on the development of iPSCs are given in Section 2.6.2. Preparation protocols for all utilized media are listed in Appendix A.

### 4.1.1. Cell Isolation of Murine Granular Cells

Animal care was performed by Eva Kronberg and cerebellum preparation was performed by Dr. Gabriele Loers, both at the Center for Molecular Neurobiology Hamburg (ZMNH), University Medical Center Hamburg-Eppendorf (UKE). Cell isolation, culturing and all further research was undertaken at the Center for Hybrid Nanostructures (CHyN). All mice were 6 - 7 days old at the time of extraction. In general, two cerebella were used for cell preparation at a time. Due to transport time between the institutes, cerebella were stored in ice cooled Hank's Balanced Salt Solution (HBSS) for up to 1.5 h after extraction before further treatment. To initiate cell separation, HBSS was taken off and the cerebella incubated in 0.66 ml trypsin/DNAse solution for 15 min at room temperature (RT). Subsequently, they were washed 3 times with ice cooled HBSS and submerged with 0.66 ml trypsin-solution, which prevents clustering after separation of the cells. The cerebella were homogenized by pipetting them up and down approx. 10 times each with three flame-polished Pasteur pipettes with decreasing inner tip diameter. 3 mL ice cooled HBSS were added and the cell solution was put on ice for 5 min. 3 ml supernatant were carefully transfered into a new centrifuge tube. Cells that were not thoroughly dissociated, remained on the bottom of the tube and were disposed. The cell solution was centrifuged for 15 min at 100 g at 4 °C. The supernatant was aspirated, leaving a small amount of solution. The cell pellet was resuspended in 3 ml of warm culture medium and filtered (pluriStrainer 20 µm, pluriSelect) to remove potential cell clusters. Culture medium was Neurobasal A (Thermo Fisher Scientific) supplemented with penicillin/streptomycin (1 %), bovine serum albumin (1 %), insulin (10 µg/ml), L-thyroxine (4 nM), transferrin holo (100 µg/ml), sodium selenite (30 nM) (all Sigma Aldrich), fetal bovine serum (6 %, Capricorn scientific - FBS Advanced) and Gibco B-27 (50 X, ThermoFisher Scientific). Cell concentration was determined by cell counting via hemocytometer in 10 µl cell suspension mixed with 10 µl trypan blue solution (0.4 %). If not stated otherwise, cell concentration was adjusted to $2 \times 10^5$ cells/ml. Cells were plated in droplets of approx. 100 $\mu l/cm^2$ suspension and left to settle for 1 h at 37 °C and 5 % $CO_2$ in the incubator. Afterwards, 3 ml cell medium was added per 35 mm Petri dish (FisherScientific, Biolite). To inhibit overgrowth with fibroblasts, cytosine arabinoside (3 µM) was added after 24 h, at which point the granular cells are firmly settled. Medium was completely renewed at 2 DIV. In subsequent medium changes, half of the culture medium was exchanged. Due to the low cell number on the substrates relative to the amount of medium, consumption of nutrients and the consequential pH change was slow and over the timespan of this thesis, medium changes were reduced from every 2 - 3 days to only once at 7 - 8 DIV. Granular cells were cultured in an incubator at 37 °C and 5 % $CO_2$ for up to 14 DIV.

### 4.1.2. Culturing of smNPC Derived mDANs

Stocks of smNPCs originating from dermal fibroblasts at passage six were provided by Michael Glatza (Max Planck Institute for Molecular Biomedicine) and stored at -130 °C until further use.[173] Culturing and differentiation were performed on Matrigel (Corning) coated 6-well plates. Basic medium for smNPCs was exchanged three times a week. Passages were split (1:10 - 1:20) every 4 - 5 days.

For normal passaging, old medium was exchanged with 1 ml accutase (StemPro) to detach the cell colonies. After 15 min of incubation, the cell solution was transfered to 10 ml split medium in a centrifuge tube and centrifuged with 1000 g for 5 min. Supernatant was removed and the cells were resuspended in 1 ml of N2/B27 solution that has been stored in the incubator at 37 °C and 5 % $CO_2$ beforehand. 100 µl of the cell suspension where then mixed with 900 µl smNPC medium. Cell concentration was determined by cell counting via hemocytometer in 10 µl cell suspension mixed with 10 µl trypan blue solution (0.4 %). Between $6 \times 10^5$ cells and $6.5 \times 10^5$ cells were planted in each new well. Excess cells were either frozen down in freeze medium as new cell stocks or discarded.

To prepare smNPCs for differentiation into mDANs, the same protocol was applied up to the point, where the cells were resuspended in 1 ml smNPC medium and the cell concentration was determined via hemocytometer. Cell suspension containing approx. $8 \times 10^5$ cells each were transfered into new wells containing 4 ml patterning medium. Patterning medium was completely exchanged every three days. After six days, patterning medium was replaced by maturation medium, the cells were split by a factor of 1:5 and they were reseeded in 12-well plates. Differentiation was completed 8 days later - after 14 days in total. The resulting mDANs were seeded on 3D cell culture substrates 1 - 3 days before the experiment.

Two different methods were used for cell planting on cell culture platforms. The transfer of the mDANs from the well onto the substrates begins with accutase and subsequent centrifugation following the same procedure as before. In one approach, the cell pellet was resuspended in 500 µl maturation medium. The density of mDANs was determined via hemocytometer and adjusted to $2 \times 10^5$ cells/ml. Droplets of approx. 100 µl/cm$^2$ cell suspension were placed on the substrates and left to settle for 1 h at 37 °C and 5 % $CO_2$, before 1 ml maturation medium was added. In the other approach, the cell pellet was resuspended in 1 ml maturation medium. The Petri dishes with the substrates were filled with 3 ml maturation medium. Subsequently, 100 µl cell suspension were pipetted into the solution in close proximity above the structure.

## 4.2. Confocal Laser Scanning Microscopy

One method to analyze biological tissue through microscopy with high spatial and depth resolution is fluorescence CLSM. For CLSM, neurons were stained using Neurite Outgrowth Staining Kit (Invitrogen, Thermofischer), including cell membrane stain (Thermofischer, 555 nm/ 565 nm ex/em) and cell viability indicator (Thermofischer, 496 nm/ 515 nm ex/em). Growth medium was removed and the substrates were treated with 1x dye mixture in HBSS or Dulbecco's Phosphate-Buffered Saline (DPBS) for 15 min at 37 °C and 5 % $CO_2$. Imaging was performed with a Leica TCS SP8 confocal microscope. Two lasers of 488 nm and 552 nm wavelength were used. Signals were detected with Leica HyD and PMT detectors generally adjusted to a range between 494 - 530 nm and 558 - 610 nm. For evaluation of cellular survival inside of 3D structures, propidium iodide (PI) (10x, Thermo Fischer) was additionally added to the dye mixture. The corresponding signal was detected at 670 - 710 nm. Rendering of images to 2D and 3D stacks was performed using Leica LAS X software or the Fuji distribution of ImageJ.[257, 258] The OrientationJ plugin in ImageJ was used for directional analysis of neurite orientation.[259, 260]

## 4.3. Scanning Electron Microscopy Imaging and Focused Ion Beam Milling

A viable tool to gain further insight on neurite pathways and the overall structure of cultivated neuronal networks is high resolution imaging using SEM. In preparation, cells have to be fixated and dried. Cultured scaffolds were immersed in HBSS with 4 % paraformaldehyde for 20 min in an incubator at 37 °C for fixation. Afterwards, substrates were rinsed three times with purified water and successively submerged in 10 %, 25 %, 50 %, 75 % and 99.5 % v/v ethanol absolute (VWR chemicals) solution for 10 min each. Subsequently, the substrates were either air dried or critically point dried for optimal preservation (Autosamdri-815 Series A, Tousimis). Substrates were stored under vacuum in a desiccator until further use.

All substrates were coated with approx. 30 nm Au by sputter coating (K550 Emitech Sputter Coater) before SEM imaging to avoid charging effects on the isolating material and for improved resolution. Imaging was performed in a Zeiss Crossbeam 550, which includes a gallium focused ion beam (FIB). Via FIB milling, polymer was selectively removed to open cross sections of tunnels allowing for direct SEM imaging of neurites inside the structure.

## 4.4. Electrophysiological Measurements

Direct measurement of electrical and voltage signals inside neurons can be achieved through whole cell patch clamp measurements, where a direct connection inside the cell is established through a glass pipette filled with an electrolyte solution. The seal between cell soma and pipette separates the interior from the outside bath solution with a $G\Omega$ resistance. The voltage and current between an electrode inside the pipette solution and an electrode dipped into the bath solution can be regulated and measured in voltage clamp and current clamp experiments to record the current that flows through the pores of the membrane and the membran potential respectively.

Here, a custom-built upright patch clamp setup was utilized.[261] The setup consists of a microscope (Nikon ECLIPE FN1) equipped with an objective with an extra long working distance of 11 mm (Nikon CFI TU Plan EPI ELWD 50× N.A. 0.60/W.D. 11.00 mm), micromanipulators (Scientifica) to precisely control patch pipettes and a patch clamp amplifier (HEKA EPC 10 USB Double). Patch pipettes were produced fresh for each experiment not more than 24 h in advance from borosilicate glass capillary blanks (GB150T-8P, Science Products) with a fiber puller (P-2000, Shutter Instruments). The tip of each pipette was heat polished (CPM-2, ALA Scientific Instruments) before use. Silver wire was utilized as pipette- and ground electrodes and freshly coated with AgCl before measurements.

Patch solutions for MCGCs were prepared according to Gall et al.[262] The pipette solution contains potassium gluconate (126 mM), glucose (15 mM), HEPES (5 mM), NaCl (4 mM), MgATP (3 mM), $MgSO_4$ (1 mM), BAPTA (150 µM), GTP (100 µM) and $CaCl_2$ (50 µM). The pH is set to 7.2 with the addition of KOH. The bath solution consists of artificial cerebrospinal fluid supplemented with NaCl (120 mM), $NaHCO_3$ (26 mM), glucose (11 mM), KCl (2 mM), $CaCl_2$ (2 mM), $MgSO_4$ (1.19 mM) and $KH_2PO_4$ (1.18 mM). It is equilibrated to pH 7.4 prior to the measurements by perfusion with carbogen gas (95 % $O_2$, 5 % $CO_2$).

Patch solutions for mDANs were prepared according to Reinhardt *et al.*[173] The pipette solution contains K-gluconate (125 mM), NaCl (10 mM), EGTA (1 mM), MgATP (4 mM), HEPES (10 mM) and D-glucose (10 mM). The bath solution consists of NaCl (140 mM), KCl (2.4 mM), $MgCl_2$ (1.3 mM), $CaCl_2$ (2.5 mM), HEPES (10 mM), D- glucose (10 mM) The pH of both solutions is set to 7.4 with the addition of KOH. If not stated otherwise, chemicals were purchased from Sigma Aldrich, VWR Chemicals or Merck Chemicals.

# Fabrication of Cell Culture Substrates 5

Previous work by Dr. Aune Koitmae focused on the formation of ordered 2D-Networks.[115] One main goal of this thesis is to combine the knowledge about neurocages and neurite guidance gained by this approach with fabrication methods for topologically advanced culture platforms and to lift the possibilities for designer neuronal networks literally into the next - third - dimension. To that end, a variety of cell culture platforms were fabricated featuring different 3D properties. The substrates discussed in this thesis can be classified into two categories - 2.5D platforms and true 3D scaffolds. 2.5D platforms are defined as substrates where 3D features such as steps and walls are incorporated through molding of a planar 2D surface. In contrast, the 3D scaffolds are built from scratch in a 3D space with no limitations in any spatial direction and the possibility of complex interior features. The fabrication methods and designs utilized, including further preparation steps necessary before culturing, are discussed in this chapter.

## 5.1. Fabrication of 2.5D Cell Culture Platforms

One way to build neuron culture platforms for contact guiding of neurite outgrowth is the modulation of initially flat surfaces. The modulated features act as orientation or barrier for the growth cone during axon outgrowth (see Section 2.5.3). Two different approaches were utilized to implement 2.5D features to substrates - grayscale lithography (GSL) and reactive ion etching (RIE) - to build surfaces with steps and trenches and force neurite outgrowth not only in plain, but along 2.5D pathways. For rapid fabrication of multiple structures, replicas of finished substrates were produced by ultraviolet nanoimprint lithography (UV-NIL). All samples were prepared in ISO-5 clean room environment.

### 5.1.1. Grayscale Lithography

While standard binary lithography is widely used for 2D structuring, GSL is a less utilized variant which enables the single-step fabrication of 2.5D features out of resist layers with sufficient thickness. The basic principle of GSL is the exposure of different areas with varying intensity which changes the penetration depth of photons into the photoresist. Since the change in intensity can be sharp or fluent, steep step-like structures as well as smooth slopes and curved structures can be shaped with this technique. Variants of GSL are based on ultraviolet (UV) lithography[263], X-ray lithography[264] or e-beam lithography.[265] Specific structures can either be transferred to the resist by utilization of complex grayscale masks combined with light exposure or by direct lithography.[266]

In preparation for GSL, glass wafers were dehydrated at 200 °C for 10 min. AZ 4562 photoresist (MicroResist) was deposited via spin coating at 2000 rpm for 30 s to get 10 µm thick layers and the wafers were kept on level ground at RT for 10 min. Optimal prebake time was 1 min at 60 °C and ramped up to 100 °C for 10 min. After GSL, the samples were developed in AZ 826 MIF (metal ion free; MicroResist) for 3.5 - 6 min, depending on structure depth. Optical GSL is carried out using a DWL66+ laser writer (Heidelberg Instruments) equipped with a 363 nm Ar+ laser (max. 360 mW). The DWL66+ can implement digital grayscale patterns in 256 possible laser intensity increments. The grayscale files were prepared with AutoCAD (AutoDesk). The process needs a photoresist with high viscosity since the layer thickness must be equal to or greater than the depth of the intended features. Laser intensity determines penetration depth of photons into the resist. For small intensities, positive tone resist becomes soluble to photoresist developer only near the top surface of the resist layer, while more resist is removed after exposure with larger laser power. Using maximal intensity, a maximum depth of 20 µm could be achieved during this work. Cross sections of step structures in AZ 4562 as result of exposure tests at 22 mW laser power are shown in Figure 5.1 a. Since photon absorption in the resist is a nonlinear process[264, 265, 267], exposure with linear grading leads to an exponential decrease of step height towards larger depths. If the goal is the production of complex geometries, results of an intensity test can be fed into computational calculation to convert desired features into fitting gray scale values. Correct values for simple structures without the demand for nanoscale accuracy, such as the ones described in this chapter, can be directly estimated based on the test results. An exemplary step structure created by GSL with a targeted step height of 2 µm is shown in Figure 5.1 b. The gray values were set to 42, 122 and 228 to reach 2 µm, 4 µm and 6 µm depths. A profile corresponding to such a step structure is shown in Figure 5.1 c. The profile indicates slightly rounded edges. Figure 5.1 d shows examples of a chessboard

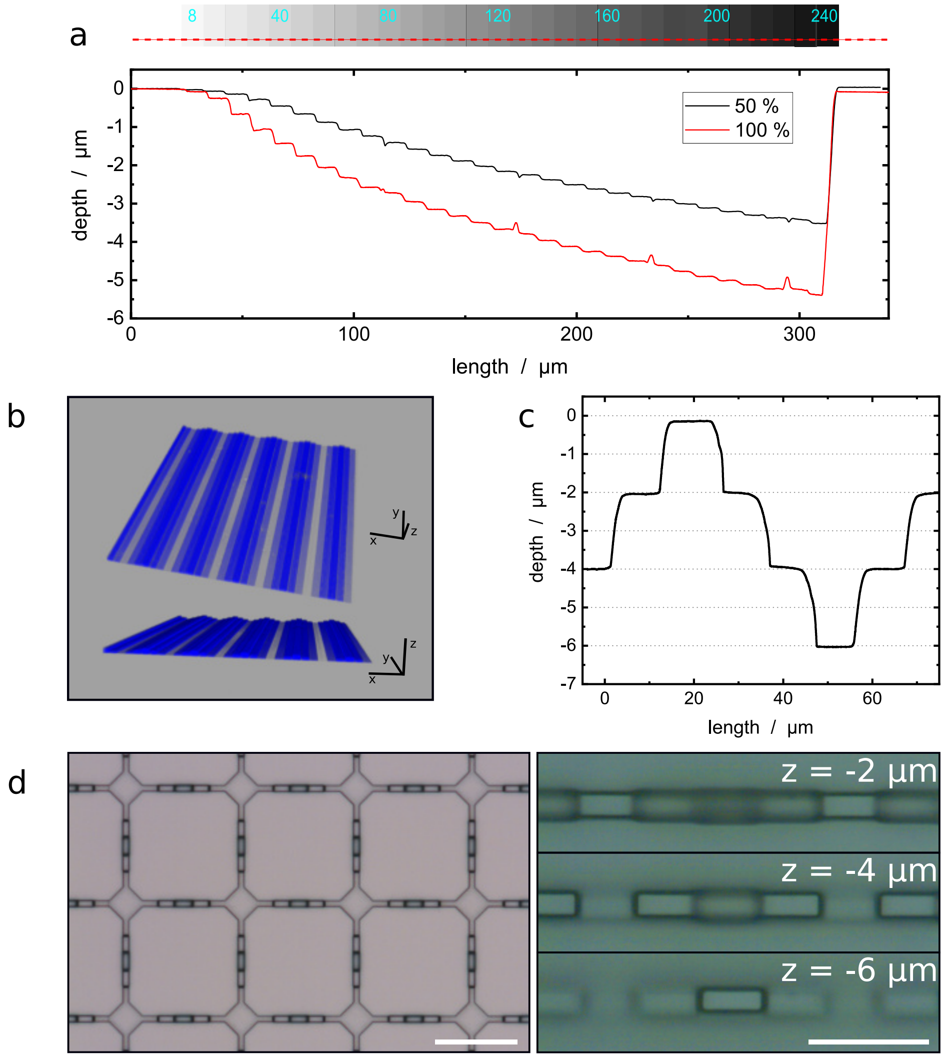

**Figure 5.1.:** Profiles and images of structures produced by GSL in AZ 4562 photoresist with 22 mW laser power. The profiles were measured with a DektakXT profilometer (Bruker). (a) Results of exposure tests. A 50 % filter was installed in the beam path of the laser for the black plot in contrast to no filter for the red plot. The gray bars at the top give a top view onto the gray values of the exposure design. From left to right, the gray values increase in discrete steps of 8, which linearly correlate with the local UV laser intensity during the writing process. The red dashed line represents the profiles displayed in the plot. (b) CLSM 3D stack of the step structure. Scale: 40 µm. (c) Profile of a step structure created through exposed with alternating gray values of 0, 42, 122 and 228. (d) Brightfield images of a chessboard structure, also produced with gray values of 0, 42, 122 and 228. Cavities are connected through channels with steps. The focus of the right images is shifted by -2 µm top to bottom. Scale bars: 50 µm, 20 µm.

structures produced with GSL. The design connects cavities through channels with integrated steps of 2 µm height with each other.

### 5.1.2. Reactive Ion Etching

RIE or plasma-assisted etching is the removal of material from a surface by reaction with material specific ions. Molecules that are stable in the gas phase and a gas with the ability of glow discharge are mixed in a reactor. When gas glow discharge is started, the molecules are dissociated and ionized. They have to be chosen selectively for the targeted material so that the products of the etch reaction are volatile. In contrast to other etch mechanisms such as chemical etching, RIE is an anisotropic process with low selectivity forming steep sidewalls perpendicular to the etch direction.[268]

In this thesis, the etched material is silicon (<100>±0,5°, Czochralski grown, Siegert Wafer). Due to the importance of RIE for the semiconductor industry, etching of silicon is one of - if not the - most commonly applied RIE process:[268, 269] The feed gas used is $SF_6$, which is split into $SF_5^+$ cations, $F^-$ anions as well as $F^*$ radicals after plasma ignition. A radio frequency driven capacity coupled electrode, which serves as holder for the Si wafer, is negatively charged by free electrons in the gas. While reactive intermediates diffuse to the Si surface, cations are accelerated onto the wafer by the electrical field resulting from the electrodes d.c. voltage. The radicals react with Si to volatile $SiF_4$ or their precursors $SiF_x$ ($x < 4$) and the cations remove the resulting $SiF_x$ layer when they hit the surface, which otherwise hinders the progression of the reaction to deeper layers. The removal of inhibiting films can be advanced by introducing additional ions to the gas for ion bombardment via sputtering and to introduce a thin passivation layer onto the etched sidewalls.

Substrates were produced in a Si 500 inductively-coupled plasma (ICP) - RIE plasma etcher (Sentech). The gaseous mixture consisted of 50 standard cubic centimeters per minute (sccm) $SF_6$ feed gas, 70 sccm $C_4F_8$ for sputtering and 5 sccm $O_2$ for glow discharge. The stage temperature was set to 0 °C, ICP power was set to 400 W and radio frequency was set to 15 Hz with a chamber pressure of 1.02 bar. In preparation for RIE, Si wafers were spin coated with LOR5A at 4000 rpm and AZ 4562 for 30 s at 4000 rpm. Prebake time was 1 min at 60 °C, ramped up to 100 °C for 6 min. Transferring the desired structures into the resist through contact lithography, the coated wafers were exposed for 15 s with 13 mW/cm of 365 nm UV light using an MJB4 mask aligner (Süss MicroTec). Photomasks were previously produced with the DWL66+ laser writer using

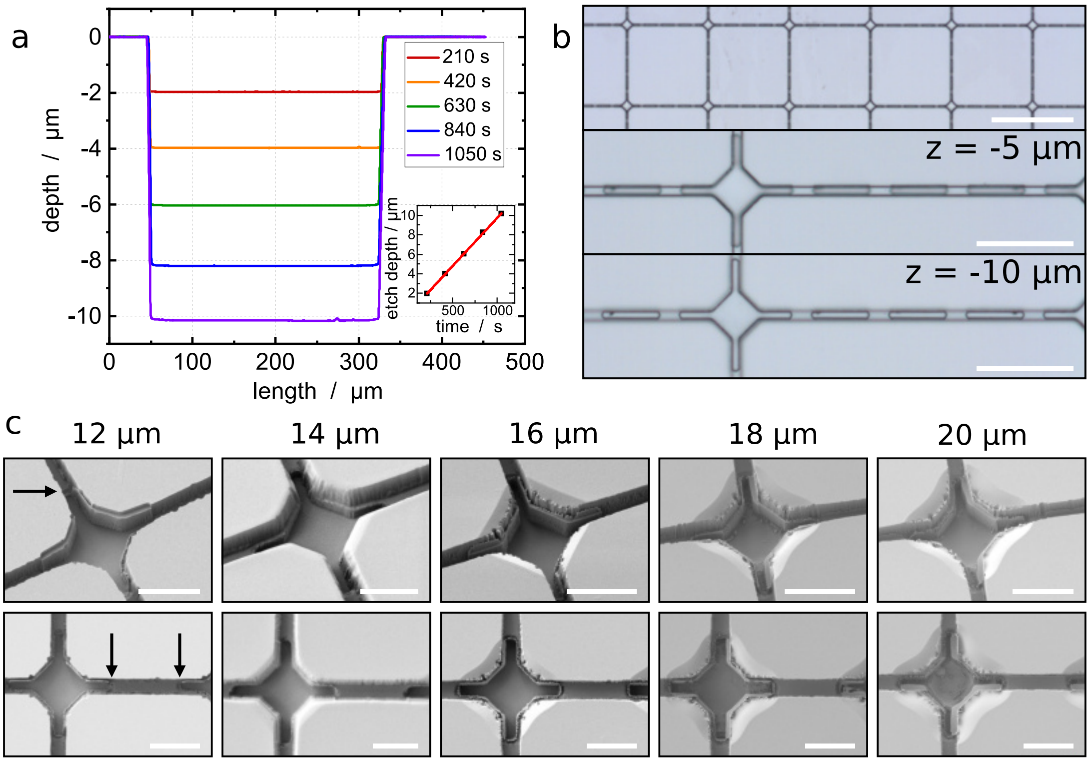

**Figure 5.2.:** Profiles and images of structures produced by RIE in silicon. (a) Cross section profiles of grooves measured with a profilometer. A plot of the etch depth against time is shown in the small graph. The etch rate is (9.8 ± 0.1) nm/s. (b) Optical images of a chessboard pattern created by two consecutive etch steps. Cavities are connected through channels with steps. The focus is set to -5 µm in the middle and -10 µm in the bottom image relative to the silicon surface. Scale bars: 200 µm (top), 50 µm (middle and bottom). (c) SEM images of chessboard structures with isolated cavities with increasing depth from 12 µm to 20 µm from left to right etched in a first step and cavities connected by continuous channels with 10 µm depth edged in a second step, resulting in steps at the cavity exits accordingly (indicated for 12 µm cavities with arrows). Scale bars: 20 µm.

prefabricated photo maskblanks (G Materials) metalized with Cr and coated with 530 nm MICROPOSIT S1800 photoresist (MicroChem). The respective exposure patterns were prepared with AutoCAD. The wafers were heated to 115 °C for 50 s for postbake and developed in AZ 826 MIF for 3.5 min. Following the RIE process, photoresist was removed with acetone in an ultrasonic bath. A plot of etch depth in dependence to process time is shown in Figure 5.2 a. In contrast to GSL, where the accessible depth of structures is limited by the maximum laser power and photoresist, structure depth after RIE is solely depending on time with a linear etch rate. Slight variations in the etch rate can be attributed to temperature fluctuations in the reaction chamber. The etch rate determined by linear regression of the etch depths is (9.8 ± 0.1) nm/s. To obtain multiple steps in one structure, up to three consecutive cycles of contact lithography and RIE were executed. An example of a structure resulting from two cycles is shown in Figure 5.2 b. Etching of channels with 10 µm gaps every 40 µm in one and overlaying continuous channels in the other cycle results in steps with the height defined by RIE in the cycle with the gaps included in the design. Figure 5.2 c shows multiple substrates for which the described principle was utilized to produce identical boundaries of 10 µm height defining channels that connect cavities with 2 µm - 10 µm additional depth, resulting in distinct steps at the channel entrances/exits. Isolated cavities were etched first, followed by the design including the channels. Steep sidewalls form 90 ° corners at the bottom of the structures. Slight misalignment of the exposure designs and interference patterns are visible due to limited accuracy of contact lithography with mask aligners during the second RIE circle. At high overall depth of 18 µm and 20 µm, deviations from the design increase with residues and uneven surface inside the cavities.

### 5.1.3. UV Nanoimprint Lithography (UV-NIL)

Even though technical solutions such as GSL and RIE enable the fabrication of demanding 2.5D structures with high resolution and fine feature sizes, the production of a multitude of substrates is time-consuming. Each sample has to be processed individually, even if the targeted design is identical. One production cycle takes hours to complete. This problem can be addressed by UV-NIL, a potent high-resolution technique for rapid and cost-efficient reproduction of substrates with 2.5D topological features.[270]

Thermal NIL was first introduced in 1995 as a new technology to produce structures with sub-25 nm feature size.[271] One year later, the first publication on UV-NIL was released.[272] The technique has further evolved since then. The basic idea of NIL is to transfer the negative of a 2.5D surface structure into another structure by deformation. NIL can be performed either by using a stamp material harder than an applied deformable material, by utilizing changing thermomechanical properies by variations in temperature or by inserting a stamp in a liquid material which is hardened in a curing process.[273] The latter is applied in UV-NIL. In two variations UV-NIL UV-curable resin is either dropped or drop-casted onto a mold (Figure 5.3 a) or a flat substrate

(Figure 5.3 b). A transparent counterpart is placed on top of the resin, leading to even distribution of resin between substrate and mold. Mold filling happens through capillary action in case of resin with very low viscosity or by small applied pressure, either externally or through sufficient tare weight of the mold. The resin is then cured by exposure to UV light. Subsequently, the resin layer is separated from the mold. It is essential for a successful UV-NIL process that the resin can be easily separated from the mold and sticks tightly to the substrate. Any resin residues on the mold after curing are nearly impossible to remove without causing damage to the structure.[274] This impairs feature quality and quickly renders the mold useless. As a preventive measure, the mold has to be covered with an anti-sticking molecule layer. The flat substrate on the other hand is covered with a bonding agent prior to UV-NIL for improved lifetime of the resulting product. The topography of the completed resin substrate is the exact negative of the mold. If executed correctly, no residue of resin is left on the mold and it can instantly be utilized to start over with the UV-NIL process and produce further resin substrates. One UV-NIL cycle only takes a few minutes to complete, enabling the rapid production of multiple substrates in a very short amount of time. Samples successfully prepared with one mold will be identical to each other, which is important for later statistical evaluation of experiments where UV-NIL produced substrates are used.

#### Experimental Process

To start UV-NIL, a structure with the desired 2.5D surface topography has to be produced beforehand to serve as parent mold. Here, UV-NIL was utilized for the duplication of structures previously produced by GSL (Section 5.1.1) and RIE (Section 5.1.2). These structures served as master stamps for the UV-NIL production. The master stamps were covered with a layer of fluorosilane (1H,1H,2H,2H-Perfluorodecyltrichlorosilane, 96 %, Alfa Aesar) as anti-adhesive coating by chemical vapor deposition (CVD). For deposition of a perfect layer without flaws, the stamps were first cleansed by sonication in acetone and isopropyl alcohol (IPA), followed by 2 min ozone exposure in an UV/ozone cleaner (UVO Cleaner Model 144AX Series, Jelight Company). The ozone treatment dehydrates the surface and leaves free hydroxyl goups on the surface of the glass substrate. CVD of fluorosilane was performed in a Vacutherm vacuum oven (Fisher Scientific) for 30 min at 80 °C and 0.4 bar, during which the fluorosilane reacted with the hydroxyl groups building a hydrophobic

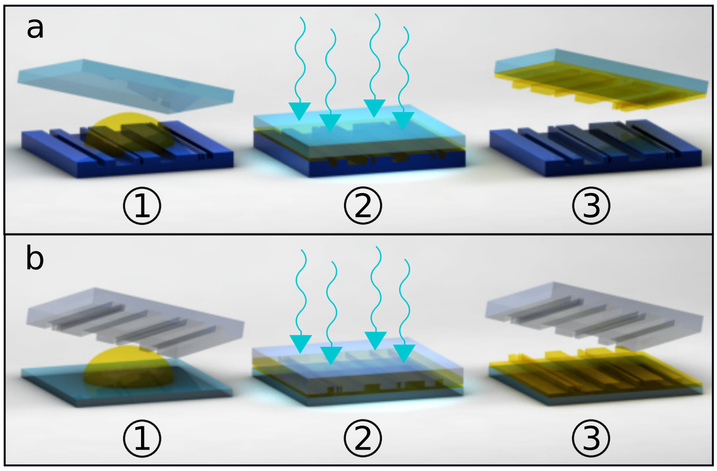

**Figure 5.3.:** Schematic of two variations of the UV-NIL process. (a) A transparent substrate is placed onto a mold with a droplet of UV-curable resin on top. UV light cross-links and hardens the resin that is now trapped between substrate and mold. The mold is separated from the resin. (b) A process similar to (a), but mold and substrate are switched. The mold material has to be UV-transparent in this process. The UV-curable resin can be cast onto the substrate beforehand to build a flat layer.

monolayer ontop of the stamp. Common glass coverslips (20 mm, #1, CarlRoth) were utilized as resin substrates. The substrates were cleansed and exposed to ozone plasma for dehydration analogous to the stamps. OrmoPrime 08 (MicroResist) was applied as adhesion layer through spin coating for 1 min at 4000 rpm and hardbaked on a hotplate for 5 min at 150 °C. OrmoStamp (MicroResist), a polymer with glass-like properties and high UV-NIL resolution, was used as resist. Single droplets were positioned centrally on the stamps, before glass substrates were placed on top without additional pressure. UV-curing was performed in an MJB4 mask aligner for 2 min with 13 mW/cm of 365 nm UV light. Separation of resin substrates and stamps were done by heating the sample to 60 °C on a hot plate and carefully inserting a sharp razor blade in between the layers. The resulting negatives of the original master stamps function as replica stamps in a second UV-NIL step. All parameters are identical to the first UV-NIL step. If performed correctly, the substrates resulting from the second process are identical in surface structure to the original master stamps. These are the UV-NIL-produced substrates that were later utilized as cell culturing platforms (see Chapter 6).

Defects commonly observed in UV-NIL on cavities and pillars are bubble defects as a result of trapped air. If not avoided, air entrapment results in unintentional molds or hillocks in the final structure.[275] The chessboard

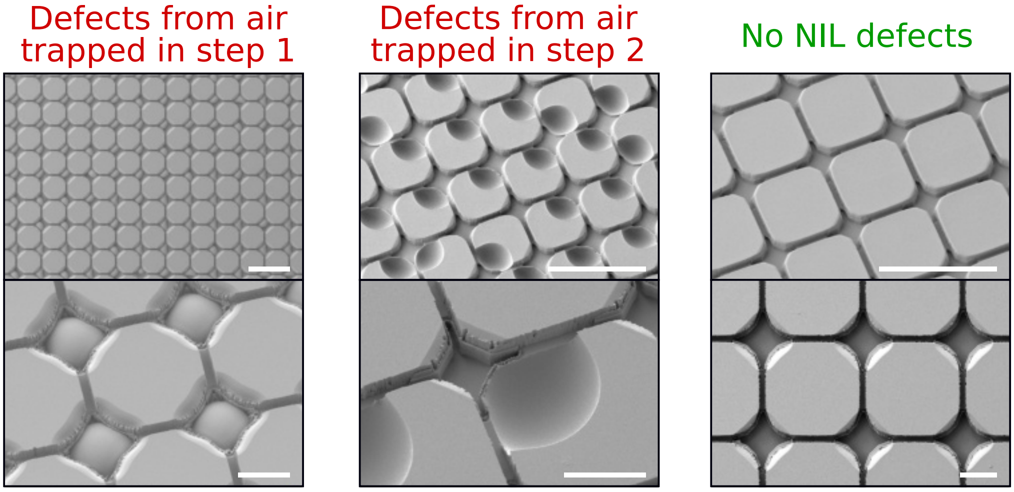

**Figure 5.4.:** UV-NIL processing errors resulting from air entrapment between stamp and resist. (left) Hillocks inside the cavities formed by air bubbles trapped between master stamp and resist during the first step. (center) Molds in the platforms formed by air bubbles trapped between replica stamp and resist during the second step. (right) Without trapped air, UV-NIL results in perfect replicas of the master stamp. Scale bars: 100 µm (top), 25 µm (bottom).

structures produced in this thesis are especially prone to enclosure of air bubbles. Examples of observed errors are shown in Figure 5.4. If air was trapped in the cavities during the production of the master stamp in the first UV-NIL step, the bottoms of the final cavities are arched towards the center with less depth. In the second UV-NIL step, air can be trapped in the cavities between the features on the inversed master stamp. The trapped air results in molds in the platforms surrounding the cavities and channels. Thus, channel walls are partially missing due to this defect. While in thin films, air bubbles can be eliminated through squeezing or gas condensation, such procedures are not possible in this case due to the size and depth of the structures.[275, 276] However, the amount of bubble defects was significantly reduced through heating of the stamps with the liquid OrmoStamp droplet before the placement of the glass substrates on top.

## 5.2. Fabrication of True 3D Scaffolds

The goal of substrates that support complex but distinctly ordered 3D *in vitro* neuronal networks cannot be achieved with manufacturing techniques such as GSL or RIE. DLW by 2PP is the only available technique to date to fabricate true 3D structures with complex inner geometry with sub-diffraction-limit resolution. Therefore, DLW was utilized in this thesis for the production of true 3D scaffolds. The technique is discussed in detail in Chapter 3.

### 5.2.1. Experimental Approach

All DLW-produced 3D microstructures described in the following sections were written with the laser lithography system Photonic Professional GT (PPGT) from Nanoscribe GmbH. The PPGT is equipped with a 780 nm femtosecond laser. The structures were written with Dipin Laser Lithography where the objective is directly dipped into a liquid droplet of the photoresist. A 63x objective was employed. The following requirements must be met to build complex 3D structures with DLW for neurite guiding. Most obviously, the resist must not be cytotoxic to be suitable for cell culturing. Additionally, it needs to have high resolution and sufficient stiffness to achieve complex structures with small embedded microtunnels. Lastly, the structures have to be stable for days to weeks in cell culture medium.

First, Ormocomp® (micro resist technology GmbH) was tested for suitability for this work. Ormocomp, an inorganic-organic hybrid polymer, is known for its biocompatibility [277] and has been used for neurocages [17] and a variety of other cell scaffolds [135, 136, 278] built by DLW. Free tunnels at the scale of 2 - 3 µm inner diameter could not be achieved in the tests with Ormocomp.

As a result, IP-Dip (2-(Hydroxymethyl)-2-[[(1-oxoallyl)oxy]methyl]-1,3-propanediyl diacrylate; Nanoscribe GmbH) was chosen in subsequent tests, a commercial negative tone photoresist known for high resolution. The elastic modulus of IP-Dip is highly dependent on writing speed and laser power. Written with the PPGT, it has been shown to be comparable to the modulus of Ormocomp close to the lower polymerization threshold, but significantly larger at high laser power.[279] A cubical with integrated tunnels serves as design for the tests. The CAD-Design of the test structure is displayed in Figure 5.5 a. The tunnels have either round or square cross sections and measure 10 µm, 5 µm 3 µm or 1 µm in diameter and width respectively. Achieving free, perfectly shaped tunnels turned out to be nontrivial. In fact, it was not sufficient to stay in the small laser intensity range between the polymerization threshold and burning of the polymer. Partial clogging of tunnels can be observed even slightly above optimal intensity parameters (Figure 5.5 b). Shrinkage after development, determined by comparing the dimensions of the produced structure with the

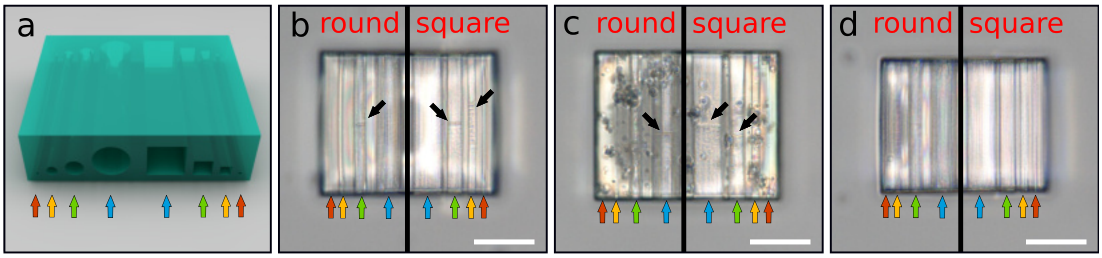

**Figure 5.5.:** Schematic and light microscopy images of intensity test results on horizontal tunnels in a cuboid. The test design has tunnels with round (left) and quadratic (right) cross section. The arrows point to tunnels of 10 µm (blue), 5 µm (green), 3 µm (yellow) and 1 µm (red) diameter. The microscopy images show a top-view onto the cuboids. (a) CAD graphic of the tunnel test. (b) Already slightly exceeding the optimal intensity leads to partial clogging of the 5 µm and 3 µm tunnels (black arrows). The 1 µm tunnels are completely clogged. (c) At too high intensity, the polymer is partially destroyed, and some tunnels are clogged (black arrows). (d) At optimal laser intensity, even the 1 µm tunnels have a clean shape and are unclogged. Scale bars: 20 µm.

CAD, is about 10%. Figure 5.5 c shows a cubical where defects caused by small gas bubbles during exposure indicate burning of polymer in addition to clogged tunnels due to too high laser intensity. The cubical is noticeably larger with shrinkage below 5%, which can be attributed to higher degree of polymerization and consequently less shrinkage during development. Also, the CAD-design with sharp corners and straight edges is conserved to a higher degree, confirming the predicted increase of the elastic modulus. The optimal laser intensity for the test structure is close to the minimum polymerization threshold (Figure 5.5 d). All tunnels have a well defined shape and are free of errors. The structure has large shrinkage of above 10%.

Based on the successful printing of the test structure, IP-Dip was the photoresist of choice in the experiments described in the following chapters. Applicability of IP-Dip as substrates for neuronal cultures is discussed in Section 6.2.

### 5.2.2. 3D Scaffold Design

To achieve the goal of a culturing platform for the easy construction of small neuronal networks with a predefined 3D pattern, the design has to meet two central conditions. First, cells should not be distributed on the substrate randomly. Specific areas for cell adhesion have to be defined in advance. Second, these adhesion areas have to be connected to each other through defined pathways that dictate the direction of neurite outgrowth. Additionally, the design is

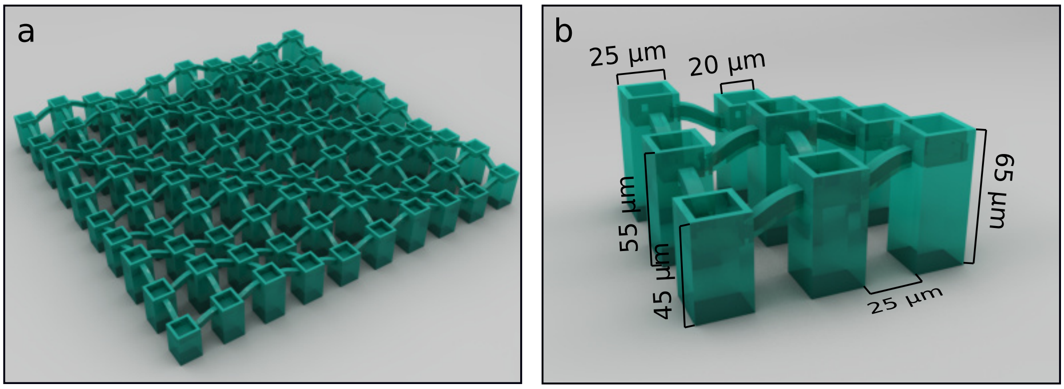

**Figure 5.6.:** CAD graphics of the 3D structure design. (a) The structure consists of 10 × 10 pillars that are connected by freestanding tunnels. (b) Close-up of a section of the structure. Pillars of 45 - 65 µm height and 25 × 25 $\mu m^2$ width with 20 × 20 $\mu m^2$ cavities on top are connected to direct neighbors over a lateral distance of 25 µm by freestanding tunnels.

supposed to be easily adaptable to create different 3D network layouts.

Koitmäe *et al.*[115] have shown that clusters of only a few (MCGCs) each can be confined in microboxes connected by 2D tunnels (displayed in Section 2.5.3, Figure 2.6) Characteristic firing of action potentials after 4 DIV was measured. In absence of any planar alternative, neurites only grew through the tunnels. The design proposed in this thesis incorporates confinement in a similar way, while obtaining complete freedom of the tunnel pathway in 3D and therefore enabling increased complexity in future designs. The design is displayed in Figure 5.6. It consists of pillars and suspended tunnels. The pillars are of three different heights, 45 µm, 55 µm and 65 µm, and stand 25 µm apart. At the top of the pillars are quadratic cavities of 20 $\mu m^2$ width, enclosed by 2.5 µm thick and 10 µm high walls. Each cavity is connected to the nearest neighbors through freestanding tunnels. The interior of the tunnels is 4 × 5 $\mu m^2$. The wall thickness of the tunnels is 1.5 µm. Neighboring pillars always have a height difference of 10 µm, so that each tunnel covers a distance of 25 µm in x- or y-direction and 10 µm in z-direction. The complete design consists of 10 × 10 pillars.

A central aspect of the chosen design are the freestanding tunnels. As the exposure tests on the test structures have shown, tunnels embedded in solid polymer are easily clogged due to scattering effects (see Section 5.2.1). With a volume of polymerization for the tunnel walls of only 1.5 µm in the design, the probability of clogging is drastically reduced. In fact, no clogged tunnels have been observed for this design, even though variations in laser power have been tested. Higher possible laser power in turn enables larger moduli, leading to more stable structures and less shrinkage during development. Despite the overall scale of the structure, fabrication time is kept at a feasible level - 2 h 40 min with 10 mm/s write speed - due to minimized exposure volume. Freestanding tunnels can easily be designed to lead into all directions desired for the respective network studies. An additional advantage of freestanding tunnels is the small surface area outside of the tunnels which reduces the probability of soma attachment on top of the tunnels during cell plating.

Another aspect of the design, partly chosen as a consequence of the exposure tests, is the use of tunnels with quadratic cross section instead of round tunnels. Quadratic tunnels have two advantages in comparison to tunnels with circular cross section: First, in optical microscopy quadratic tunnels are visually clear with sharp boundaries while round tunnels are more obscure due to refraction effects (see Figure 5.5) Thus, the visibility of neurites in confocal imaging might also improve. Second, trenches and corners have previously been shown to direct neurite outgrowth as topological cues.[104, 109, 113, 121]

In summary, the scaffold design combines enclosed areas in form of cavities of different height that are conceived as potential neurocages with freestanding tunnels that are intended to act as design specific 3D neurite guides between the somata.

### 5.2.3. Fabrication and Optimization

The feasibility of the design with DLW was first tested on a simplified model with pillars of the same height. The tunnels in this test design have 4 µm inner diameter in horizontal and 5 µm in vertical direction. They are horizontal, with a slight bending of 1.5 µm upwards towards the center. The structure was written at 10 mm/s and approx. 17 mW laser power. Slicing distance was set to 0.3 µm. Hatching and contour distance for the tunnel structures was 0.2 µm. The samples were developed in MR-Dev 600 (1-methoxy-2-propanol acetate, micro resist technology) for 30 min and subsequently immersed twice in isopropyl alcohol (99.9 %) for 60 s. Optical microscopy images of the results are shown in Figure 5.7 a. The structure was written rotated by 45° (compared to the x-y-orientation shown in the figure) with write fields of 71.71 µm and 2 µm overlap. That way, pillars are placed at the borders of write fields and have to be stitched. All tunnels are completely inside the write fields and can therefore be written without risk of stitching errors. Each write field is written layer by layer.

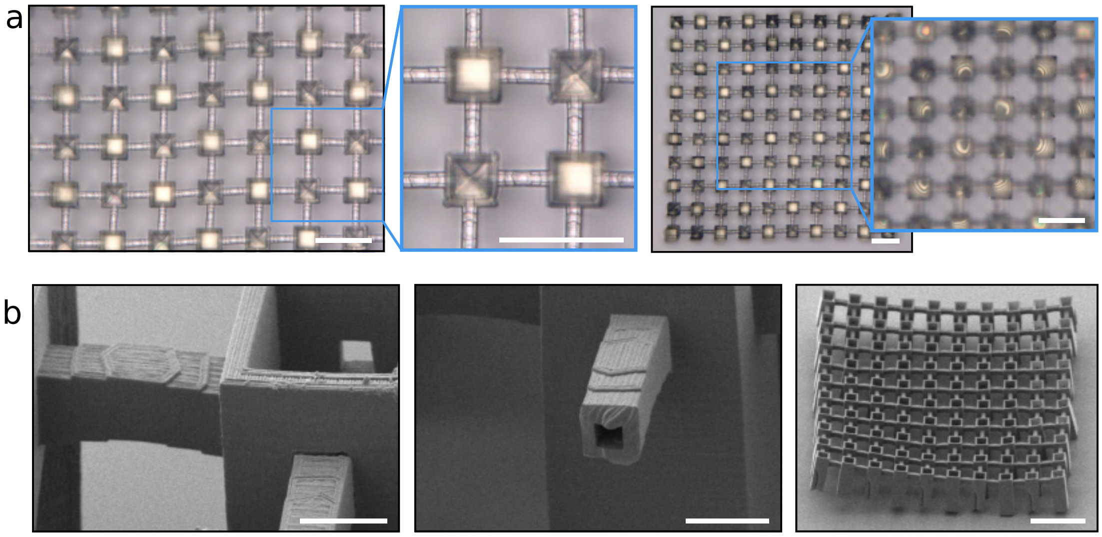

**Figure 5.7.:** Images of a simplified 3D structure with horizontal tunnels written with DLW. (a) Optical images of well defined structures with free tunnels between quadratic cavities. One write field (45° rotated in the image) contains one whole pillar and four pillar sections that are stitched during the writing process. As a result, half of the pillars are stitched from four parts. Stitching slightly reduces the volume of cavities. The chessboard pattern of the design is slightly deformed and the corners are out of focus if focused on the middle part. A zoom with focus on the glass/polymer interface reveals interference patterns. Scale bars: 50 µm. (b) SEM images of 3D structures. The CAD design was adequately reproduced within the resolution set by the thickness of the written lines. The tunnels have a well defined quadratic inner cross section. The structure is stable, but the corners are lifted from the glass carrier. Scale bars: 10 µm, 10 µm, 100 µm.

The tunnels appear to be completely free and open at the ends, connecting one cavity with the next. Considering the whole structure, slight deformation in all directions can be observed. The structure is attached to the glass carrier only at a small spot towards the middle, which is shown by interference patterns at the interface between scaffold and glass.

SEM imaging confirms the conclusions drawn from optical microscopy (Figure 5.7 b). Well defined cavities and tunnels were written. The small elevation towards the middle of the tunnel is realized through process-inherent steps. To analyze the inner dimensions, the structure was cut open by FIB milling. The inner cross section of the tunnels in the CAD template is $4 \times 5\,\mu\text{m}^2$. The cross section of tunnels in the completed structure is nearly quadratic with interior dimensions reduced to $3.5 \times 3.5\,\mu\text{m}^2$. The width of the tunnel walls is between 2 µm and 2.5 µm. The corners of the scaffold are lifted from the carrier glass

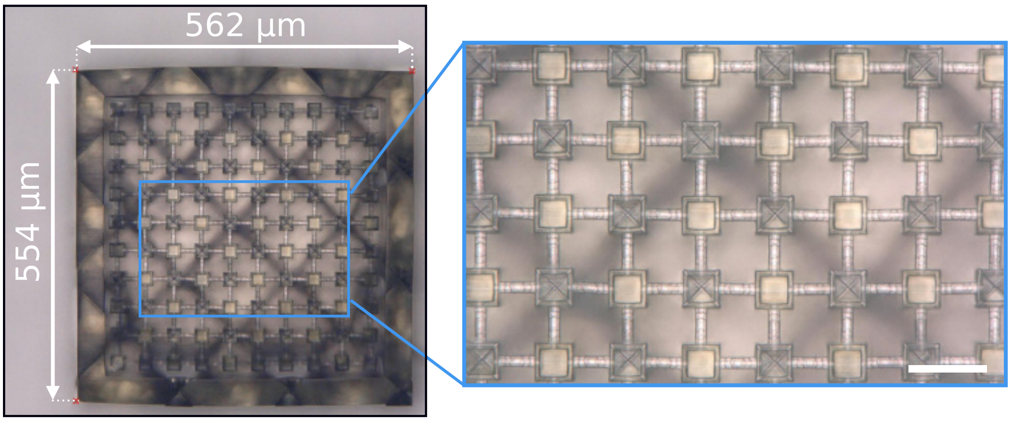

**Figure 5.8.:** Optical images of a simplified 3D structure, written inside a polymer box. The chequered pattern is well preserved and all boxes are at the same height. The box is 7 % smaller than the original CAD-design. Scale bar: 50 µm.

surface, which is caused by contraction of the polymer during development and consequential detachment of the structure as relief of strain (see Section 3.4.3 for more details on shrinkage and resulting strain).

### Optimization Step 1

The strain leading to detachment is caused by shrinkage adding up to tens of microns over the entire structure. The shrinkage stands in contrast to a solid carrier material. So, in order to prevent strain inside the structure, some alteration needs to be performed regarding either the carrier or the structure itself. The single-anchor support proposed by Maruo *et al.*[247] is not feasible in this case due to the scale of the design. Numerical shrinkage compensation, that works conditionally well on a simple woodpile structure, is also not feasible in this case.[240] Instead, in a first approach, the structure has been placed inside of a polymer box. Thus, glass as carrier material for the structure was effectively replaced by IP-DIP. The box of 600 × 600 µm$^2$ is written first and the actual design is then written inside of the box afterwards (Figure 5.8). Lacking fine features, the box can be written at higher speed with 20 mm/s and slightly increased laser power. After development, the size of the box is reduced to approx. 560 × 560 µm$^2$, a shrinkage of ~7 %. The pillars are thereby firmly attached to a ground that shrinks simultaneously at approx. the same amount and rate as the written design itself and stay in straight lines towards each other.

For optimized fabrication time, the box was written in 140 × 140 µm$^2$ write fields and the actual 3D design (Section 5.2.2) was written in write fields set to

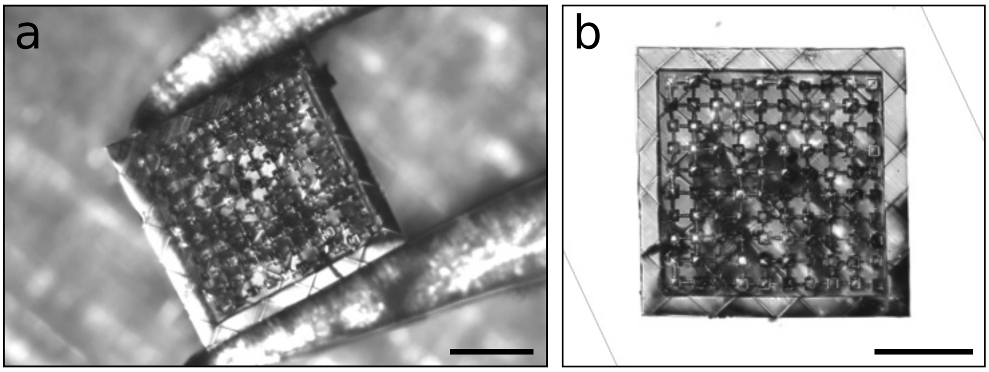

**Figure 5.9.:** Optical images of the transfer of a 3D structure onto another glass carrier. (a) The structure clamped between reverse action tweezers and lifted from the glass carrier. (b) Structure after the transfer onto a new carrier substrate. Scale bars: 200 µm.

$141.42 \times 141.42\,\mu m^2$. Fabrication time of one 10 × 10 cell culture scaffold with the distance between written lines adjusted to 100 nm is 2.5 h. One carrier box with the line width adjusted to 700 nm is written in 3/4 h. The write fields of the box were stitched diagonally. Even though the boxes have rough stitching, they are sturdy and can even be transfered onto a different substrate with reverse action tweezers (Figure 5.9). As long as only the walls of the box are clamped, the culturing scaffold is not affected.

However, after several days in solution during culturing experiments, the boxes themselves detach from the carrier glass. To prevent detachment of the boxes in wet medium, the concept of multiple anchors utilized by Ovsianikov *et al.*[248] was refined for scaffolds with these relatively large dimensions. Flexible springlike spirals with high flexibility were written onto the glass prior to the boxes, connecting the boxes to the glass surface. Optical images of a simplified 3D structure inside a box attached to the carrier through spirals are shown in Figure 5.10. Prepared this way, scaffolds have been recycled for multiple culture cycles, sticking firmly to the glass carrier.

The first design of the 3D structure with pillars of different heights was written successfully inside boxes. SEM images of the structure are displayed in Figure 5.11. The main difference to the simplified model in this first design is the incorporation of height differences between the pillars and the placement of larger write fields of $141.42 \times 141.42\,\mu m^2$. With this change, stitched pillars are only composed of two parts, which reduces stitching errors end enhances stability. The height difference covered by the tunnels between pillars is realized in multiple small steps. The structure is firmly attached to the bottom of the box without deformation. Culturing experiments using these structures are discussed in Section 6.2.2.

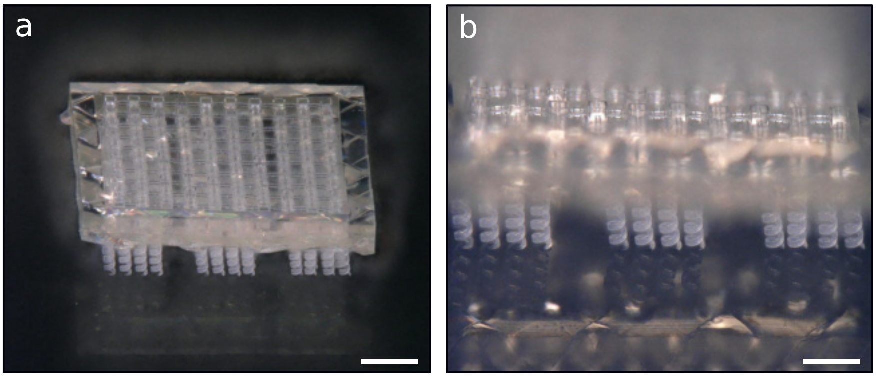

**Figure 5.10.:** Optical microscopy images of a simplified 3D structure inside a box that is attached to the glass carrier through polymer springs. (a) Isometric view onto the structure written inside a box. The box is not in direct contact to the carrier glass, but stands on springs, also written with DLW beforehand. Scale bar: 100 µm. (b) Side view of the scaffold on springs. The tunnels and cavities are transparent to light. Rough stitching of the box is clearly visible in the reflection. Scale bar: 60 µm.

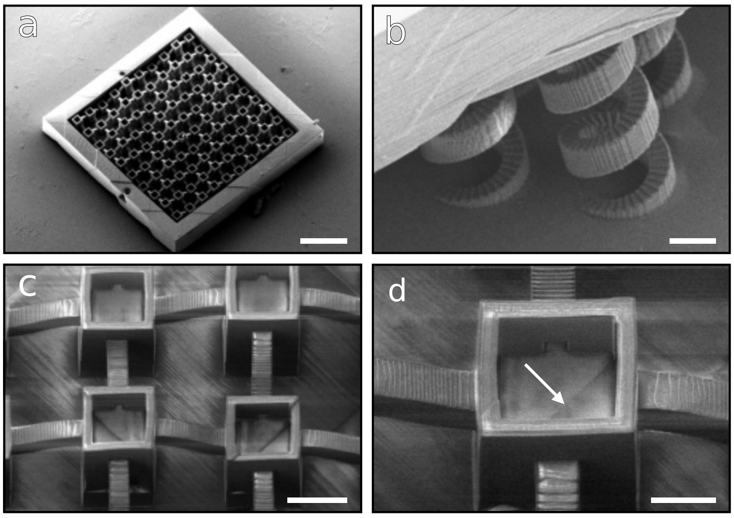

**Figure 5.11.:** Scanning electron microscopy images of the first 3D structures for cell growth studies. (a) The structure written inside a box. (b) Spring structures, compensating shrinkage with flexibility. They are slightly bend towards the center of the box and connect it firmly to the glass carrier. (c) Pillars of different height inside the box. (d) A pillar of medium height. The tunnels on the left and back lead to higher pillars, while the tunnels on the right and front go downwards. The arrow points to a diagonal line through the cavity, which is an artifact of write field stitching. Scale bars: 150 µm, 10 µm, 20 µm, 10 µm.

### Optimization Step 2

Two improvements of the design were made following the first culturing results leading to the final design described in Section 5.2.2. First, the tunnel diameter in the CAD was further reduced by 1 µm from $4 \times 5\,\mu m^2$ to $3 \times 4\,\mu m^2$ for enhanced confinement of the neurites. Second, the height of the cavity sidewalls was reduced from 15 µm to 10 µm. The reduction was foremost motivated by the necessity of accessibility of cell somata for electrophysiological measurements (see Section 4.4). A positive side effect might also be a better supply of nutrients due to improved diffusion of fresh medium to the neurons.

The improved structure inside a box is displayed in Figure 5.12. SEM images were taken after culturing and cleaning with 70 % ethanol. For improved contrast, the scaffold was sputtered with approx. 40 nm Au prior to imaging. After residing in solution for days and being exposed to ethanol multiple times for sterilization and cleaning, the box has notable defects along the writing direction of the laser during DLW (Figure 5.12 a). In contrast, the cell-scaffold itself is visually not affected. Since the complex is designed to stick to one carrier glass with no need of transfer with tweezers, the height of the box walls was reduced, giving access to the patch clamp pipette to all cavities independent of the direction (Section 6.4) as well as speeding up the writing process The springs, partly overgrown by cellular material, are still firmly attached to the glass carrier (Figure 5.12 b). The scaffold itself is still well defined, with reduced size of the tunnel entrances of 2.3 µm width (Figure 5.12 c). The walls of the cavities are slightly bend outwards. As described in Section 3.4, the amount of shrinkage during development is linked to the polymerization yield. When the scaffold is written with less intensity than the box, shrinkage is not identical and the walls are slightly bend as a result. To determine the quality of the tunnels, the structure was selectively cut open by FIB milling (Figure 5.12 d-e). The layer-by-layer writing results in small round hillocks in the magnitude of ~100 nm. Apart from that, the tunnels are well defined over the whole length with height and width of about 2.0 - 2.2 µm (Figure 5.12 f), a magnitude that has proven favorable for single neurite guiding in previous guidance studies.[100, 101, 115]

Even though the manufacturing of springs and boxes as carriers for the structure has proven to be an effective tool to provide stability, it increases time and cost of the production. Evaluation of neuron cultures in the structure by optical microscopy is impaired by the underlying springs and patch clamp

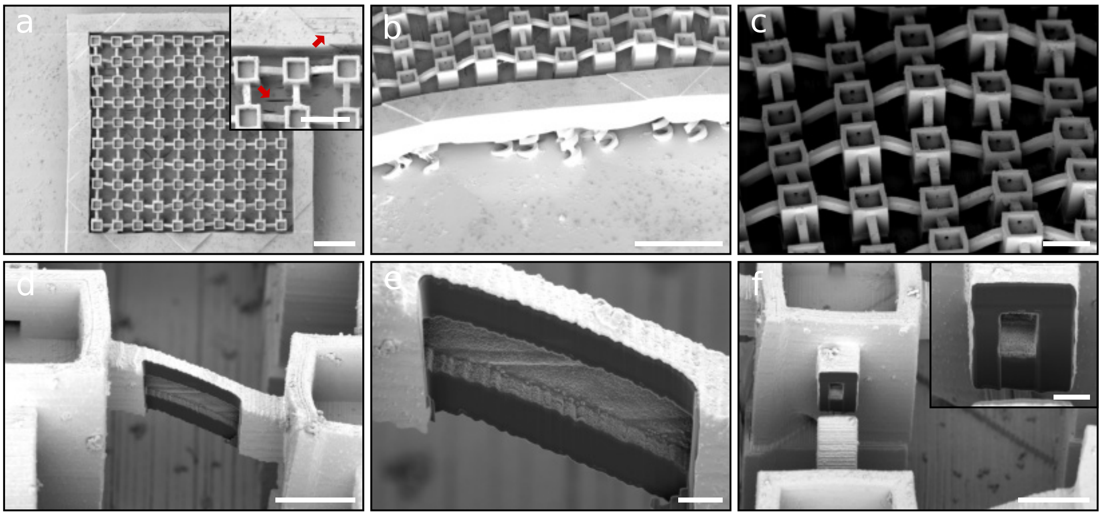

**Figure 5.12.:** Scanning electron microscopy images of 3D structures printed with the final design and covered with approx. 40 nm Au. (a) The structure written inside a box. The red arrows in the insert point to defects of the box. (b) Side view onto the structure. The height of the box sidewalls is reduced to 25 µm. Springs connect the box to the carrier glass after shrinkage. (c) Pillars of different height inside the box. The entrances to the tunnels are nearly quadratic with approx. 2.3 µm width. The walls of the cavities are slightly bend outwards. (d-f) Tunnels cut open by FIB milling. The tunnels have rounded steps on the outside as well as the inside. The cross section of the tunnels has a well defined rectangular form throughout the whole length. Scale bars: 100 µm (a,b), 50 µm (a inset), 30 µm (c), 10 µm (d f), 2 µm (e,f inset).

experiments are significantly more difficult due to poor visibility of the somata (see Figure B.1). In order to replace the box as an extra carrier, the structure itself needs to compensate shrinkage and firmly stick to the glass carrier. The observations above show how reduction of the cavity wall height enables the structure to release stress through slight inherent deformation. The use of higher laser power closer to the burning threshold additionally reduces shrinkage due to higher degree of polymerization. Lower cavity walls combined with reduced shrinkage were successfully utilized to keep the scaffolds in place on the glass carrier without detachment or deformation during development (Figure 5.13). Even though the raised laser power also leads to larger elastic modulus and the strain, still present, slightly bends the outer pillars towards the center, all pillars stick firmly onto the glass surface. In contrast to the deformation shown in Figure 5.7, the pillars stand in perfectly straight lines as defined by the CAD-design. Stitching errors are reduced due to increased stability of the footing. Slight roughness of the structure's surface is induced by the slicing, which is defined previous to the DLW process.

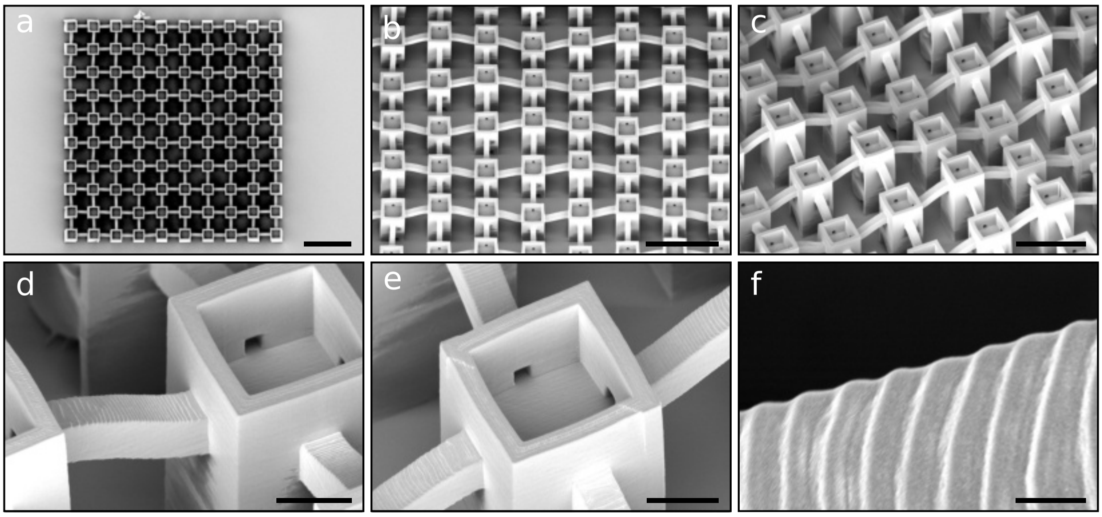

**Figure 5.13.:** SEM images of 3D structures for cell growth studies written directly onto glass carriers. All pillars are firmly attached to the glass surface. (a) Outer pillars are slightly bent inwards due to stress arisen through polymer shrinkage. (b-c) Inner pillars stand completely straight and in line. The form given by the CAD design is preserved. (d) A tunnel leading 10 µm downwards into a cavity. Slight surface roughness inside the cavity created by chosen line width during DLW is visible. (e) A pillar of medium height. Small diagonal misalignment of approx. 100 nm is visible as a result of write fields stitching. (f) Close-up on the top of a tunnel, showing uniformal rounded steps. Scale bars: 100 µm, 75 µm, 50 µm, 10 µm, 10 µm, 1 µm.

While the depicted optimizations significantly improved the quality of structures directly written onto the glass carrier, they are not sufficient to connect the structures to the glass as efficiently as deformable springs. Most structures stay in place for one culturing experiment, but when cleansed with the intend to reuse for further cell cultures, most structures detached and were lost. This problem is solved by coating with a biocompatible layer before utilization as culture platforms (Section 5.3).

### 5.2.4. Variants

Scaffold fabrication utilizing DLW by 2PP allows for easy adaption of produced geometries by simply changing the CAD. Therefore, the pillar scaffold is designed with the aim to be easily adjusted to the requirements in diverse cell culture studies. A variation of the structure with increased diversity in pillar height, tunnel length, and tunnel orientation was written as proof of principle for adaptability (Figure 5.14 a). The tunnel length in this design varies from

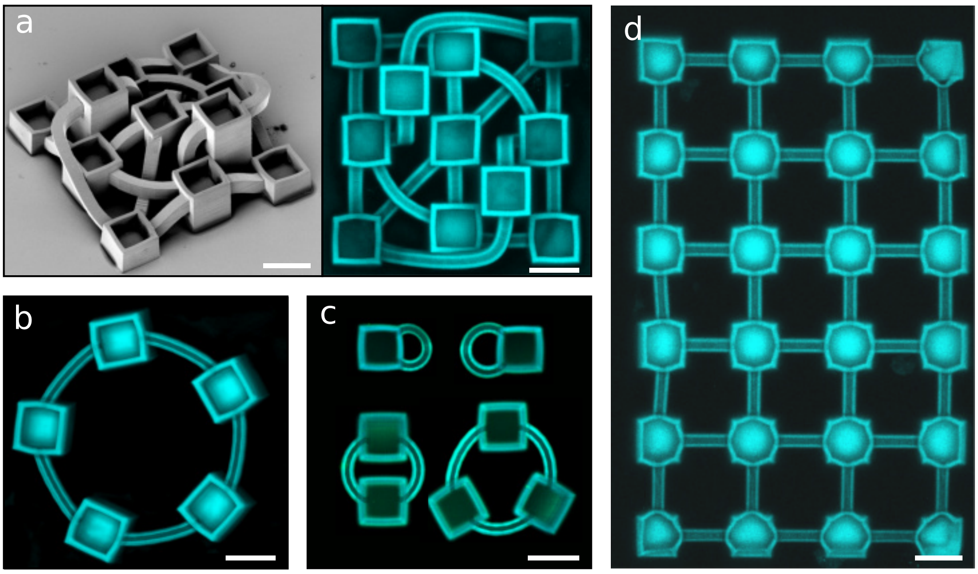

**Figure 5.14.:** SEM and CLSM images of alternative variants of the 3D scaffold design. (a) Structure with various pillar heights and tunnel pathways to support neurite guidance on varying distances and 3D directions. (b) Ring-shaped pillar structure to support circular network formation. (c) Single pillars with tunnels connecting cavities with themselves and two or three pillars and tunnels arranged circularly. (d) Structure with 4 × 6 cavities and planar tunnels written in one write field for fast production of scaffolds and facilitated analysis of culturing results. Scale bars: 25 µm.

25 µm to 100 µm with up to 30 µm distance covered in z-direction and changing slopes between 0 ° and 90 °.

In another variation a low number of pillars are connected in a ring-shaped arrangement (Figure 5.14 b and c) with the motivation to test the formation of autapses, the synaptic connection of a neuron to its own dendrites or soma,[280, 281] or circular connections of only a few neurons. Such connections could act as neuronal feedback loops in future designer neuronal networks, a concept utilized in the brain to tune synaptic feedback for memory storage.[282]

The final variation applied in cell culture studies during this thesis are 4 × 6 pillar structures in a planar chessboard arrangement (Figure 5.14 d). This simplified design was chosen with the objective of rapid production of multiple scaffolds on the one hand and streamlined analysis of cell cultures on the other hand. The planarity ensures that all cells are in focus simultaneously in optical microscopy images and it significantly reduces expenditure of time during confocal imaging. The scaffolds were written in single write fields without stitching. While stable in the center, it has a reduced degree of polymerization towards the edges as a result and cavity walls are partially sagged. The total height of all pillars is set to 30 µm for this structure for additional reduction of fabrication time to approx. 12 min each.

## 5.3. Substrate Coating

Cultivation of neurons *in vitro* is a demanding task, because primary neurons are very sensible to environmental conditions. If roughness or chemical composition of the culture platform are not favorable, cell adhesion and viability can be impaired.[283] Additionally, the concentration of trace elements in the culture solution has to be well defined. Atoms, molecules or ions dissolving out of substrate materials can disturb cellular functions and lead to cell death.

A solution to both of these aspects, allowing for even toxic materials such as GaAs to be used as basis for culture platforms[18, 115], is pin-hole free coating of the surface with a biocompatible material with favorable properties. In case of DLW by 2PP, pin-hole free coating overcomes the limitation of biocompatible photoresists for cell culture platforms. On complex 2.5D surfaces and 3D structures with interior surface areas, suitable methods for the application of these coatings are limited. The two methods utilized here are CVD and atomic layer deposition (ALD). Unlike directed deposition methods such as physical vapor deposition (PVD), where shadowing effects can create hillocks and gaps, the covering material reaches the surface through non-directional diffusion in the gaseous phase. As a result, layers of material are deposited all over, even on complex surfaces. Two materials were tested as cover material, parylene-C (ParC) (Section 5.3.1) and $Al_2O_3$ (Section 5.3.2).

A positive effect of coating with ParC or $Al_2O_3$ besides improved culturing conditions is the adequate compensation for the omission of springs to keep the structure attached in solution. The pin-hole free layer prevents any interaction between the liquid and the polymer/glass interface and adds extra stability. Structures printed with the final design described in Section 5.2.3, step 2, stayed in place for multiple culture cycles with cleansing in between.

Biocompatible surface quality is a precondition for cell culturing. For neurons to actually settle and to build neuronal networks on a substrate *in vitro*, an additional attractive chemical factor is usually needed.[284] Here, substrates are coated with PDL (Section 5.3.3), which has been well established as effective surface coating in bioneurology for several decades.[97, 99, 285]

### 5.3.1. Chemical Vapor Deposition of Parylene-C

ParC is a crystalline thermoplastic polymer. Parylene has some unique properties that make it predestined as coating for a wide variety of applications. It builds transparent, pin-hole free coatings that can act as dielectric barrier, it is chemically inert, is resistant to high temperatures and adds negligible weight to the covered device. Most importantly for this work, parylene has excellent biocompatibility and biostability.[286] The highest standards of biocompatibility are met for plastic materials (ISO 10993 and USP Class VI).[287] Since the formation takes place from the gaseous phase one molecule at a time, very homogeneous layers are deposited onto the surface of the substrates, preserving fine features in topology. Parylene has been used for more than 40 years as coating material for medical devices and implants. Especially in the field of neural recording on electrode arrays, ParC is widely used. [286–292]

ParC was coated on cell culture substrates by CVD in a SCS Lab-coater® 2 (Speciality Coating Systems), a vacuum system specifically designed for the purpose of parylene deposition. The deposition takes place in three main steps. First, ParC dimers in the form of granulates are heated under vacuum conditions at 150 °C and 0.1 Torr and build a dimeric gas through vaporization. Second, the gas is heated to 680 °C and the dimers are pyrolized to monomers. In the final step, the monomeric gas is released into the chamber with the scaffold substrate. At 25 °C, the ParC monomers are deposited and form a transparent polymer film on the surface. In previous experiments with 0.7 g ParC all surfaces of structures, including interior surfaces of microtubes, were coated with a layer of approx. 130 nm thickness.[115] In this work, 0.5 g were used for coating.

### 5.3.2. Atomic Layer Deposition of $Al_2O_3$

Alumina ($Al_2O_3$) is deposited by ALD utilizing trimethylaluminum [$Al(CH_3)_3$] and water as precursors.[293, 294] The ALD process produces conformal, dense and pin-hole free layers.[295] $Al_2O_3$ coating has high abrasion resistance and hardness, and it is bioinert.[296] Thin layers of nm-thickness are sufficient to cover substrates completely. Cell proliferation and activity has shown to be promoted on $Al_2O_3$ covered glass substrates *in vitro* compared to plain glass control.[297] $Al_2O_3$ has also been used as cover material for implants, such as for microelectrode arrays for neural recording.[298–301]

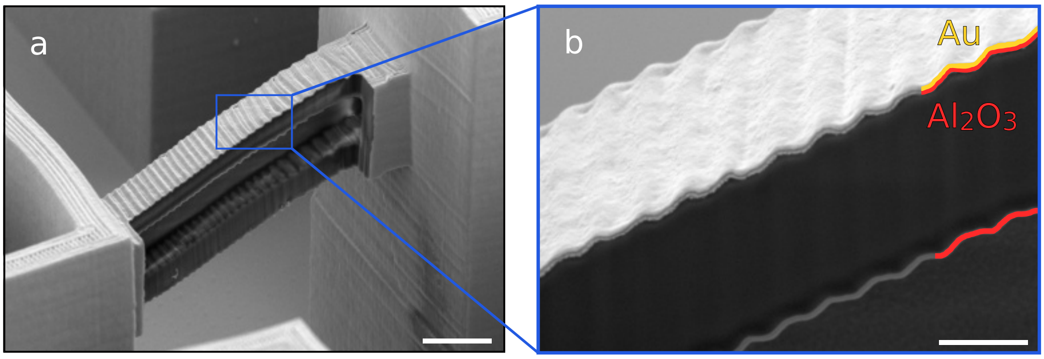

**Figure 5.15.:** SEM images of a tunnel cut open by FIB milling. To prevent the scaffold from electrical charging and obtain the necessary resolution for milling, a layer of gold was sputtered on top of the structure beforehand. (a) Cross section of a tunnel, milled nearly over the entire length. (b) Side view on the ceiling of the tunnel. On the top, two layers of coating material are visible - the sputtered gold layer on top and $Al_2O_3$ underneath. Inside of the tunnel one layer of $Al_2O_3$ is visible. Scale bars: 5 µm and 1 µm.

$Al_2O_3$ was deposited in a custom-built ALD system. On planar control substrates, a layer thickness of 15 nm was determined by spectral ellipsometry. The deposition on a 3D scaffold was analyzed by FIB milling. In Figure 5.15 a tunnel cut open by FIB milling is shown, confirming that the surface of the scaffold is covered with a uniform layer of $Al_2O_3$. It is deposited outside as well as inside of the tunnels, covering the polymer surface completely.

### 5.3.3. Coating of Poly-D-Lysine

An important factor on artificial culture platforms besides topology is the chemical composition of the surface (see Section 2.5). Specific chemical cues can promote and direct the attachment of neuronal somata and the outgrowth of neurites. For this thesis, PDL, a cationic polymer promoting cell adhesion and neurite outgrowth[285] as well as laminin, a protein promoting neurite outgrowth and neuron viability [90], were applied to the substrates. PDL was applied in three different ways, depending on the objective. Regardless of the PDL deposition method, all substrates were treated with ozone plasma at 3.5 - 5 W for 3 - 5 s in a plasma system (Femto, Diener Electonic) in advance to increase the hydrophilicity of the surface. Directly before cultivation, all substrates were additionally coated with laminin by incubation with laminin solution (10 µg/ml for MCGCs and 50 µg/ml for mDANs) for 20 min.

### Unspecific Coating

In the simplest case and on control substrates, nonspecific coating onto the whole surface of the culture platform is required. A droplet of approx. 100 µl/cm$^2$ PDL solution (0.01 g/l, mol wt 30k - 70k, Sigma Aldrich) was pipetted onto the substrates. 3D scaffolds were treated with droplets of 20 µl PDL solution each. Resting time was at least 30 min. After removing the PDL solution, the substrates were cleansed with DI-water (18.2 MΩ) two or three times to remove excess PDL molecules.

### Selective Coating with a Material Printer

To confine cell attachment and neurite outgrowth on some 2.5D substrates to more specific areas, patterns of PDL were printed utilizing a Dimatix Materials printer DMP-2831 (Fujifilm). PDL solution is filled into cartridges with 16 nozzles. Each nozzle ejects 1 pl droplets of liquid. The write head moves across the stage in x- and y-direction and releases droplets according to a pattern programmed beforehand. The formation of droplets is controlled by a piezo element. Piezo-element voltage was set to 20 - 25 V, with a jetting frequency of 2.5 kHz. The temperature of the nozzle chamber as well as the sample holder was set to 21 °C. The distance between write head and substrate was set to 600 µm. With these settings, areas of 20 - 30 µm diameter each could be selectively covered by individual PDL droplets. The viscosity of PDL solution, estimated based on droplet velocity and piezo-element voltage, is approximately 13 cP. [302]

This method was successfully applied to flat surfaces and stair case structures, but could not reliably be utilized for chessboard patterns and the 3D scaffolds, which require precise coating of small cavities. A minimum droplet size of 1 pL completely fills up one cavity of $10^3$ µm$^3$. Since the droplets fall onto the samples with a velocity of 10 -15 m/s, printing of these cavities is impossible without massive spillage, even using larger cavities of $20 \times 20$ µm$^2$ side length. Additionally, the precision of the stage alignment is limited to ±25 µm, thus rendering reliable loading of the cavities impossible. Therefore, this approach is not well suited for these substrates.

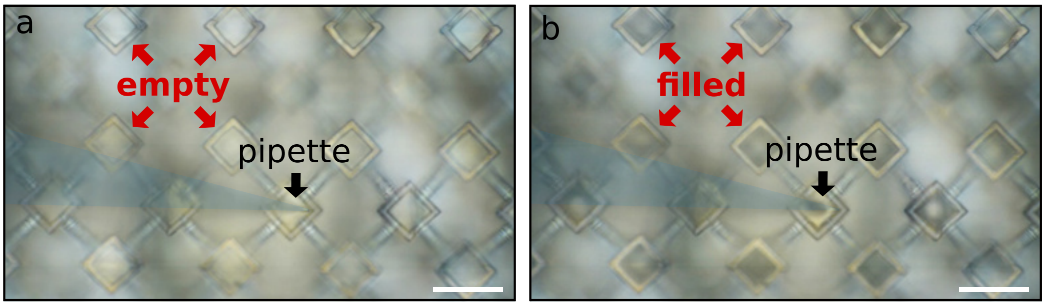

**Figure 5.16.:** Optical images of the PDL coating process in 3D substrates. The pipette is slightly colored for higher visibility. (a) Pipette filled with PDL solution hovering above the substrate with the tip inside of a cavity without physical contact. The tip is carefully approximated to a bottom corner. (b) Upon contact with the cavity corner, surface tension breaks and cavities and tunnels are filled with liquid. Scale bars: 40 µm.

### Selective Coating with Micromanipulators

Since the material printer is not suited for precise PDL coating of cavities, a more direct, manual method was applied. An upright patch clamp setup was utilized for site specific PDL coating. The setup consists of a microscope, an objective with a large working distance, a micromanipulator and freshly prepared glass pipettes with an opening of down to $< 1$ µm. For more details on the setup see Section 4.4.

The general procedure to treat the 3D scaffolds with PDL is as follows: a pipette filled with PDL solution is carefully approximated until the tip of the pipette is hovering inside a cavity. The scaffold is oriented in such a way that the tip directly points to a corner. Upon contact, surface tension at the tip of the pipette is broken and the solution is released into the cavity without additional pressure. Connected tunnels and cavities are automatically filled with solution through capillary forces. The height difference of the cavities to each other has no negative impact. All cavities are completely filled without overflow. No leakage was observed, showing that the cavities are without major defects. After a few seconds, the pipette is removed from the cavity and the solvent evaporates within $1 - 2$ s. This way, only cavities and tunnels are coated at the inside, where cell adhesion and growth is desired, while all outside surface is free of PDL adhesive factor.

Chessboard patterns were selectively coated utilizing the same approach. Different to the 3D structures, cavities and channels of these 2.5D substrates exert less strong capillary forces. To fill a multitude of cavities in one step, air pressure was gently applied to the pipette containing the solution. However, this method is highly sensitive when applied to 2.5D substrates and prone to large-scale spillage of PDL solution.

# 6

# Analysis of Culturing Results

In this chapter, the results of cell culturing are presented with a focus on regulated soma adhesion and neurite guidance. First, cell culture results on modulated 2.5D surfaces produced with GSL, RIE and NIL are presented. Second, results of neuronal network formation in 3D structures produced with DLW by 2PP are discussed.

## 6.1. Culturing on Modulated Surfaces

The influence of step cues on neurite behavior has been investigated in the past for a variety of cell types such as chick embryo cerebral and murine embryonic cortical neurons.[303–305] Here, the potential of step cues serving as guides and barriers for the formation of ordered neuronal networks in 2.5D pathways is examined.

### 6.1.1. Steps and Channels by Grayscale Lithography

#### Steps

First, network formation of MCGCs seeded on surfaces modulated to step structures by GSL is discussed. Vital neuronal networks have developed on the substrates after 4 DIV (Figure 6.1 a - c). A tendency to settle on lower levels on the structure rather than on the top steps is observable. 32 % of the cells are seeded in the pits, 34 % on the lower steps, 27 % on the higher steps and 8 % on the top steps. The overall cell density on the displayed substrate is $(648 \pm 114)$ cells/cm$^2$. The pits and top steps each make up 1/6 of the total surface area, while lower and higher steps each make up 1/3. Thus, the measured cell density is highest in the pits with $(1086 \pm 264)$ cells/cm$^2$. Network formation over the total substrate surface shows that the steps do not present a barrier for neurite outgrowth. However, the outgrowth is significantly influenced by the topography and many neurites are oriented in the direction of the step edges. Only a few neurites cross the top steps. A large part of neurite trajectories is oriented in an angle of ±15 ° towards the step edge direction (Figure 6.1 d).

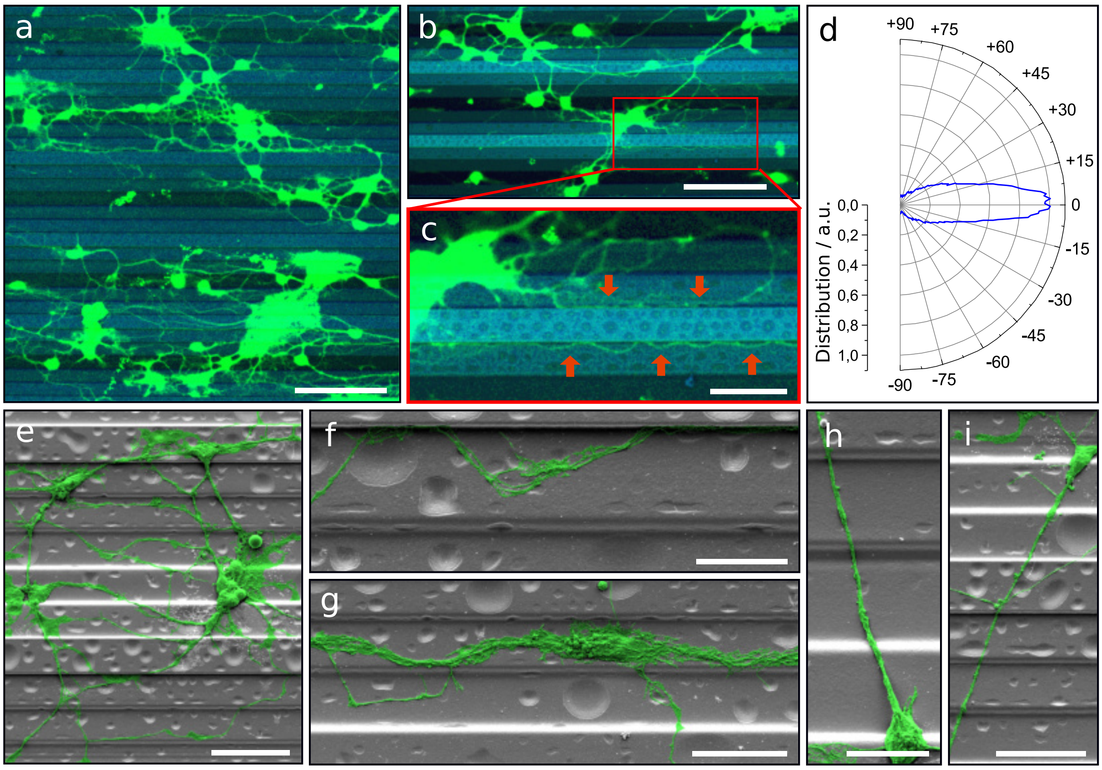

**Figure 6.1.:** (a-c) CLSM images of MCGCs cultured on ParC coated step structures produced by GSL at 4 DIV. Brightness of the steps correlates with the height: Light top steps and dark bottom pits. Red arrows point to neurites guided along edges. Scale bars: 75 µm (a,b), 25 µm (c). (d) Circular histogram of the normed distribution of neurite orientations in (a) relative to the step edges. (e-i) False-colored SEM images of neurons on step-structures after 4 DIV. Scale bars: 25 µm (e), 10 µm (f,h), 20 µm (g,i).

Further insight on the network geometry is provided by SEM analysis of the same culture. Most neurites are roughly oriented in step edge direction for a large portion of their paths. However, when steps are crossed, neurites are predominantly not deflected (Figure 6.1 e). Many thin neurites as well as neurite bundles are guided and deflected by step edges (Figure 6.1 f-g). A majority of observed neurites that cross multiple steps both upwards and downwards without deflection have a trajectory over 60 ° relative to the step edges (Figure 6.1 h-i).

In summary, vital and large networks of MCGCs were cultivated on the GSL-produced step structures. Somata settled on steps of varying heights as well as neurites extended over steps introduce 2.5D modulation to the neuronal network. However, additional guidance is needed to define neurite pathways that cross the steps and cultivate ordered 2.5D networks.

### Channels

One possibility to introduce order to neuronal networks cultivated on step-structures is the addition of further topological contact guidance. To this end, chessboard structures of cavities connected by channels with steps produced by GSL were utilized as cell culture platforms for MCGCs. The height difference between consecutive steps is 2 µm. Two neurons in adjacent cavities after 6DIV are displayed in Figure 6.2 a. Neurites in the channels show exemplary behavior for pathfinding observed on these substrates. Neurites originating from cell somata that are settled in cavities are mostly extended towards the channels. Over a certain distance, the neurites are guided over the steps along the bottom of the channels (1). At some point, typically after crossing one of the top level steps, the neurites attach to the channel wall and do not follow the steps back downwards (2). Some neurites subsequently leave the channels. In the displayed case, the main trajectory remains inside the channel and leads back down onto the channel bottom. Other neurites leave the channel after crossing the channel bottom towards the other edge when approaching a higher step level (3).

The general guidance effect of the channels is showcased in Figure 6.2 b. Most neurites originating from a cell cluster settled near a cavity, as well as the neurites of somata settled on the top rim of a channel are extended into the channels. Guided neurites appear to be longer than neurites without contact guidance, which might indicate an acceleration of the neurite outgrowth through contact guidance in the channels similar to the effect shown for neurites inside of tubes.[38] Nearly all observed neurites leave the channels at some point and extend onto the substrate surface without 2.5D structuring. Observed neurites of somata settled inside of cavities typically exit the channels before reaching an adjacent cavity (Figure 6.2 c).

While neurite guidance along the channels is observed in the cases described above, a majority of the somata is settled on the flat surface (Figure 6.2 d). Single neurites from these somata are extended into the channels, but large parts of the neuronal networks are formed on the surface without modulation. Neurites of these networks, especially in case of neurite bundles, build suspended bridges over the channels (Figure 6.2 e) or extend down on one side wall and up on the other side wall without changing the trajectory (Figure 6.2 f ,g). Some small somata are settled inside of a channel. Neurites can be extended into the channels as well as onto the flat surface in this case (Figure 6.2 h).

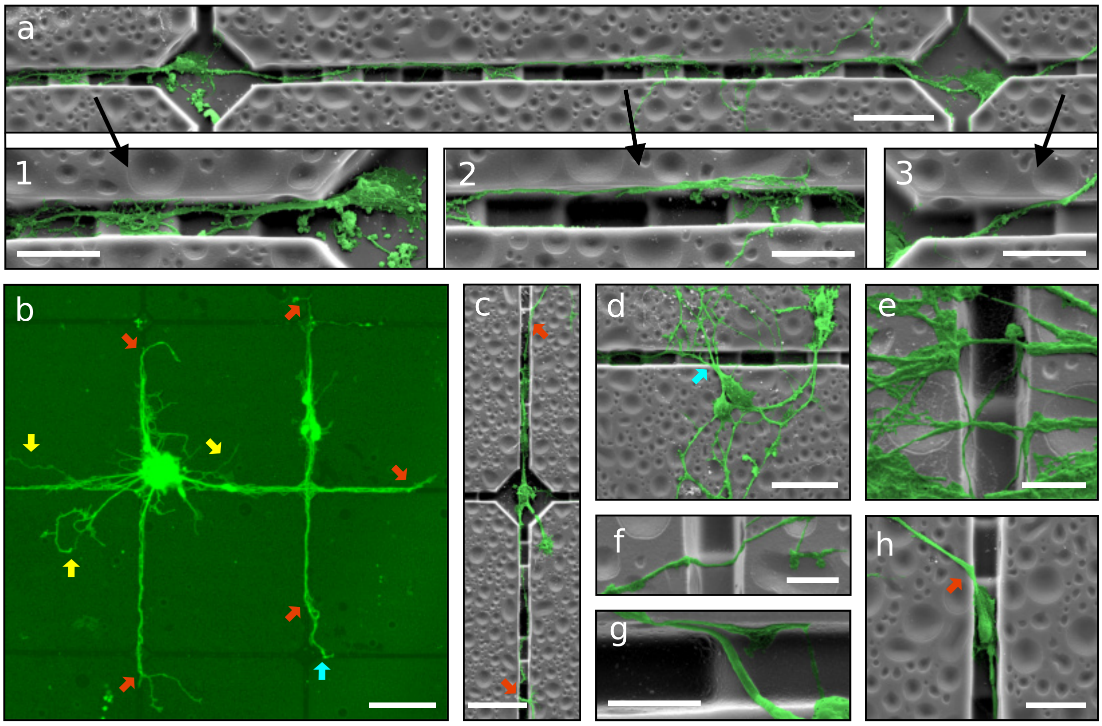

**Figure 6.2.:** False-colored SEM images and a CLSM image of MCGCs on chessboard structures produced by GSL after 6 DIV. Red arrows indicate spots, where neurites leave the channels. Yellow arrows indicate neurites, that are not guided. Blue arrows indicate reentering of neurites into channels. (a) Two connected neurons. Three magnified areas of interest show (1) guidance along the bottom of a channel, (2) guidance on the side-wall of a channel and (3) a neurite pathway exiting a channel. (b) Neurites originating from a cell cluster and somata that are settled on top of channels. (c - h) Examples of neurites exiting, entering and crossing channels. Scale bars: 20 µm (a), 10 µm (1-3, h), 75 µm (b), 25 µm (c), 20 µm (d), 5 µm (e - g).

The observations show that steps and walls produced by GSL are sensed by the growth cone. The effect is not strong enough to reliably build ordered 2.5D networks on the structured surfaces, but some neuron caging and neurite guidance is given. The path chosen by neurites after encountering the border of a step or a channel is dependent on angle of approach. At large angles, neurites tend to cross steps and channels without change of trajectory. At small angles, they tend to follow the step edge direction or channel. This behavior is analogous to stripe 'tracking', observed for neurites encountering stripes of fixed chemical guidance cues laminin and fibronectin.[44] High probability of neurites exiting the channels at some point can be attributed to frequent directional changes of the trajectories induced by the step structure inside the channels. Neurites have previously shown to cross boundaries more often on surfaces with multidirectional patterns than neurites on unidirectional patterns.[111] The observation of longer neurites when extended through channels fits previous findings where axons on anisotropic patterns where significantly longer than axons on flat surfaces.[112]

### 6.1.2. General Effect of Poly-D-Lysine

The common method to promote adhesion and neurite outgrowth on artificial substrates in *in vitro* cell cultures is modification of the surface chemistry: Selective adhesion coating can support topological guidance.

The effect of selective surface coating with PDL on MCGCs is first evaluated in isolation on flat substrates without contact guidance to evaluate it as chemical guidance factor. The neurons were cultivated on glass substrates with an $Al_2O_3$ surface coating. Droplets of PDL solution printed with a material printer (see Section 5.3.3) resulted in a pattern of circles with approx. 36 µm diameter. Confocal images of culturing results after 7 DIV for circles printed every 90 µm are shown in Figure 6.3 a - c. $89 \pm 5\,\%$ of all somata are settled directly on or are attached to circular areas covered with PDL. A network of neurites spans between the circles. In the case of somata that are located between circles, their neurites are directly extended to the nearest circles. In the coated areas, somata and neurites are more likely attached and extended on the outer rim than in the center.

The results indicate a very strong PDL dependence of cell attachment and migration of somata on the substrate. Cell adhesion near the edges of circles indicate an uneven distribution of PDL residue in the rings, likely due to the so called coffee-ring effect, known to occur in ink-jet printing of polymers.[306] During neurite outgrowth, PDL clearly functions as a guidance cue. Orientational analysis of the neurite growth directions in case of PDL droplets with 90 µm periodicity (Figure 6.3 d - e) reveals that the simple quadratic pattern is sufficient to introduce a certain order to the network. Dominant neurite orientation towards 0 ° and ± 45 °. Spreading of most neurites between nearest and second-nearest circles (Figure 6.3 f) results in preferred directions either parallel or diagonal to the printed pattern.

Figure 6.3 g - i show close-ups of cultivated circles printed every 190 µm. Here, nearly all cellular material is attached at the PDL spots. Neurites of vital cells are exclusively extended inside the boundaries of the coated area. This result indicates that the minimal distance of 154 µm exceeds the maximal distance

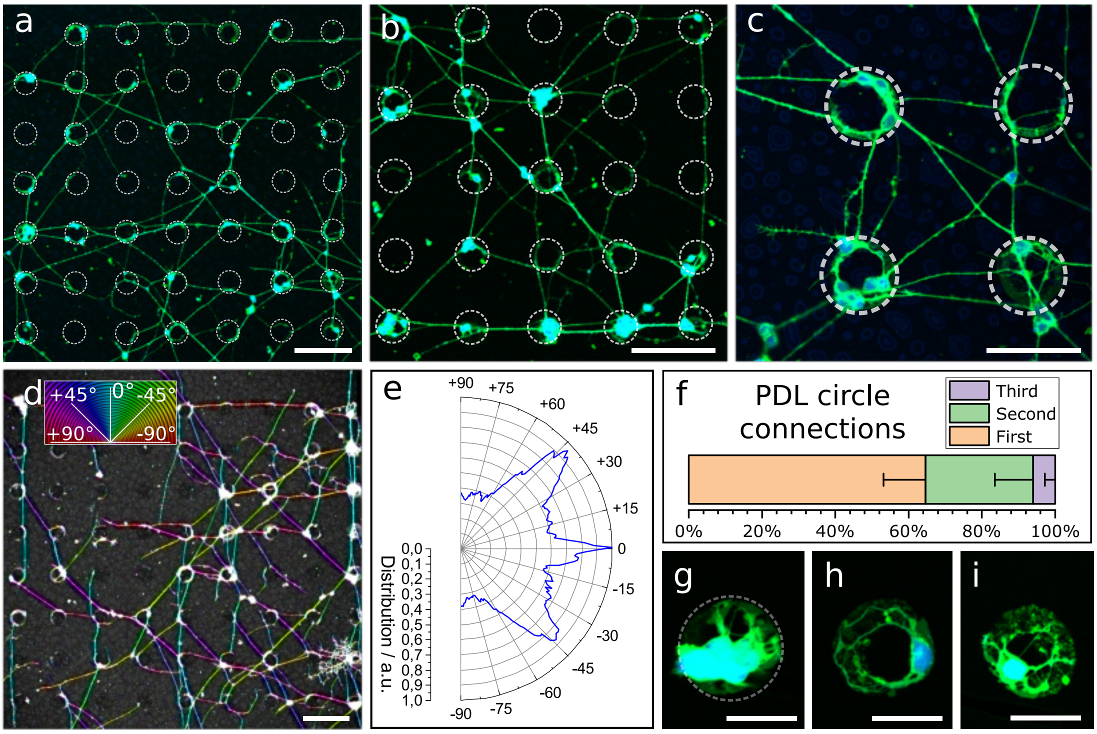

**Figure 6.3.:** CLSM images and orientation analysis of neurons cultured on PDL circles with diameters of approx. 36 µm printed on $Al_2O_3$ surface (7 DIV). (a-c) Circles printed in a pattern of 90 µm and an average distance between two circles of 54 µm. (d) Color-coded confocal image of neurons cultured on PDL circles in a pattern of 90 µm. Coloration of neurites corresponds to the neurite direction relative to the pattern. (e) Circular histogram of the normed distribution of neurite orientations on the pattern. (f) Percentage share of neurite pathways between nearest (first), second-nearest and third-nearest circles. (g-i) Circles printed in a pattern of 190 µm and an average distance between two circles of 154 µm. Scale bars: 100 µm (a,b,d), 50 µm (c) and 25 µm (g - i).

neurites of MCGCs span without attractive chemical guidance cues. When the distance between PDL-covered areas is too large, neurites retract and start sensing in a different direction. As a result, no neuronal networks can be formed over PDL coating with large distance spacing. In literature, the critical distance neurites will span without attractive cues in between is given in the range of 60-80 µm, depending on type of neuron. A single vital cell inside a circle is a special case. The only possibility to interact for such a neuron is with itself - the autapse.[280] Autapse has been shown to occur in *in vitro* experiments with isolated neurons in 2000 by Rao *et al.*[281]

### 6.1.3. Steps and Channels by Reactive Ion Etching

#### Steps

In contrast to GSL-produced steps, steps produced by RIE have sharp, well defined edges with 90 ° angles. Thus, they are well suited to assess neurite pathfinding along competing growth options when exposed to barriers of different heights. Three different cases are observed on steps of 3 µm, 6 µm and 9 µm height and 12 µm width with overall PDL coating (Figure 6.4). On 3 µm steps, the orientation of neurites in the network is statistically random with the neurites freely extending over the steps. On 6 µm steps, neurites in networks have a predominant orientation along the edges of the steps and somata are mostly settled on lower steps and in pits. However, cross-linkage over the top steps is sufficient for network connections between the pits. Interestingly, neurites of single or only a few neurons are switching between perpendicular and parallel orientation along the step edges. On 9 µm steps, no network formation across the steps is observed. Neurites are deflected when approaching a lower step edge, which leads to confinement in the pits and guidance along the step edge direction.

Li *et al.* reported a threshold height of 10 - 11 µm for cortical cell cultures in the crossing and turning on steps coated with PDL.[305] They noticed, that the threshold is of the same magnitude as the growth cone dimensions of cortical neurons. Here, the results indicate that the scale of the growth cone might also be the defining factor for the threshold for MCGCs in crossing steps. The growth cones of the cultured MCGCs have typically 5 - 7 µm width (see also Figure A.4). When encountering a step of larger vertical dimensions, the cone

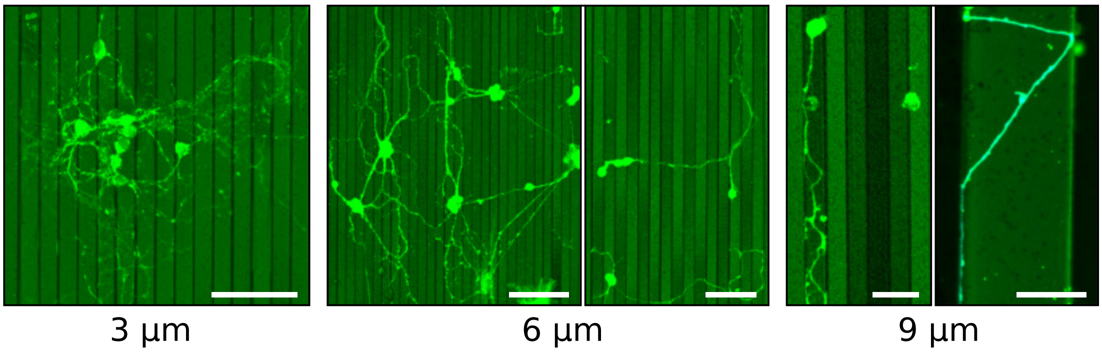

**Figure 6.4.:** CLSM images of MCGCs at 10 - 11 DIV on steps produced by RIE. Steps of 3 µm, 6 µm and 9 µm height and 12 µm width, coated with ParC and PDL. Scale bars: 50 µm, 75 µm, 50 µm, 25 µm, 20 µm.

would need to turn in a 90 ° angle to cross onto the next step while turns in plain offer alternative pathways with smaller bending angles. Thus, neurites are entrapped by vertical walls of 9 µm. When encountering smaller steps, the bending angle needed to extend onto the next plane is reduced which in turn increases the likelihood of crossing.

The orientation of neurites perpendicular to 6 µm steps for low density cell cultures may be explained by the presence of topology as single guidance cues in the absence of other cells nearby. When the growth cone senses an edge, it can either align with the edge or continue its trajectory across the edge to sense for the next cue. The closest way to the next cue in form of the next step edge is directly 90 ° across the step. This form of perpendicular contact guidance has previously been observed on grooves of sub-micron dimensions and on radial neurite bundles.[307–309]

Lines of PDL printed perpendicular to the step edges was additionally tested for 6 µm and 9 µm steps in order to force neurons to form ordered networks with neurites extended over multiple steps. However, this method results in reduced network formation - probably due to unequal PDL coating. See Section A.1.4 for further details.

### Channels

Analogous to the culture platforms produced by GSL, chessboard structures of cavities and channels with steps were produced by RIE and NIL, and cultivated with MCGCs to obtain ordered 2.5D neuronal networks. Unlike previously, PDL was not coated onto the entire surface, but specifically printed to enhance the selectivity of cell adhesion. Figure 6.5 a shows a sample, where PDL was coated with a materials printer aimed to the cavities and channels. It is reasonable to assume that droplets with PDL solution spread through the channels through capillary forces before evaporation of the solvent, leading to PDL coating that is distributed in the whole modulated area. Using this surface treatment, guidance in the confined area is achieved and a neuronal network spans through the channels and cavities. However, neuronal somata are mostly not settled in the cavities, but on top of or in the channels.

Figure 6.5 b highlights a downside of PDL coating with the material printer, exemplarily shown on an alternative chessboard design with a periodicity of 70 µm, 14 µm cavity depth and only one step of 4 µm height per channel. Droplets of PDL solution aimed at the cavities were deposited onto the channels

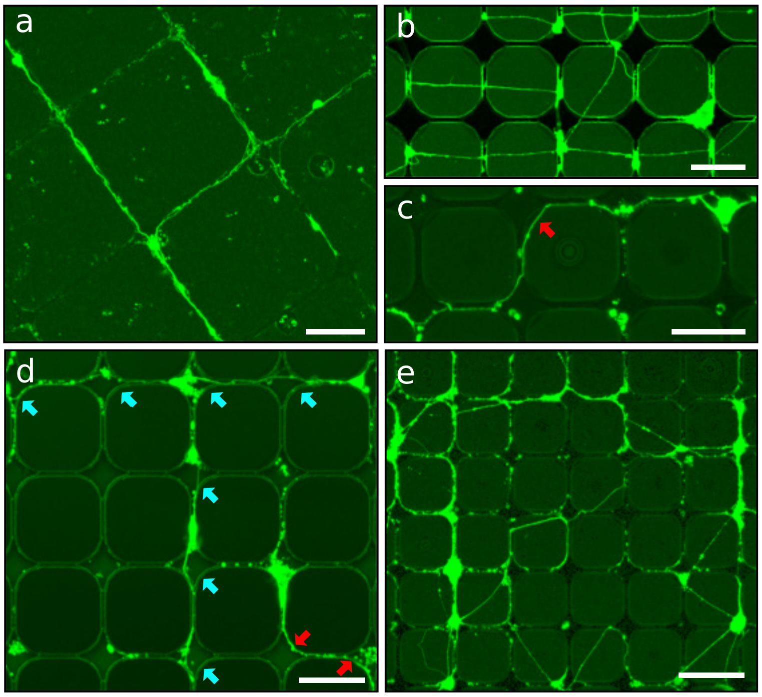

**Figure 6.5.:** CLSM images of MCGCs at 6 - 8 DIV on chessboard structures produced by RIE and NIL. (a) Cavities of 10 µm depth and steps in channels of 5 µm height coated with PDL with a materials printer. (b - e) Cavities of 14 µm depth and steps in channels of 4 µm height. PDL coated by a material printer (b) and with a micromanipulator (c - e). Red arrows indicate neurites guided at the top edge of cavities. Blue arrows indicate neurites at the bottom of cavities. Scale bars: 75 µm (a, e), 50 µm (b - d).

due to the insufficient accuracy of the stage alignment. As a result, somata are settled in the channels and neurites are spread on straight lines across the surface of the sample.

Figure 6.5 c - d shows examples of the same design with PDL deposited by a micromanipulator directly into the cavities and channels with a micromanipulator. With this setup, neuronal networks with somata exclusively attached to the cavities and several neurites that spread through the channels and along the bottom of the cavities are formed. Some neurites are partially guided along the top edges of the channels and cavities. When clusters of several cells are settled in cavities, some neurites are spread across the surface towards different cavities (Figure 6.5 e).

The design was tested with step heights between 2 µm and 10 µm. Overall, the neuronal networks in the RIE etched structures have a high degree of order and guidance along 2.5D pathways for step heights of 4 µm and below. In accordance to the findings on step structures, step heights above 6 µm hinder neurite elongation and observed neurite guidance occurs mostly for clusters along the top edge.

### 6.1.4. Lessons for 3D Scaffold Design

From the culturing results on modulated surfaces, the following conclusions are taken and transferred to the design and handling of 3D scaffolds for ordered networks:

- Vertical walls with sufficient height and sharp 90 ° edges can confine neurite extension in a defined space on the bottom plane. For MCGCs, heights of $\geq$ 9 µm are sufficient for neurite caging.

- Guidance through channels with changing trajectories: Every change raises the probability of the neurite extending along the side wall and exiting the channel over the top edge. Therefore, guidance exclusively through a 3D design can only be ensured by tunnels.

- Selective chemical coating reduces potential cell adhesion spots and areas of neurite outgrowth predominantly to the coated areas. Coated cavities act as efficient neurocages.

## 6.2. Murine Neuronal Networks in 3D Structures

In this section, culturing results on and in the 3D substrates produced with DLW by 2PP are presented and analyzed.

### 6.2.1. Topological Guidance Effect of Tunnels

During axon extension, the growth cone extends and retracts depending on the sum of all environmental factors or cues it senses in close proximity. The direction of further extension is influenced by chemical guidance and contact guidance (Section 2.5). Here, the topological guidance induced by 3D structures and tunnels is evaluated.

To study the direct effect of the scaffold design on cell adhesion and the neurite path, all structures were completely coated with PDL, so no gradient of attractive chemical cues is present. Simple cubes written onto a glass slide were cultivated to test cell survival and adhesion in the presence of the IP-DIP resist. An exemplary image of the culturing result at 8 DIV is displayed in Figure 6.6 a. Cell somata are adhered around the sides of the cubes at the interface between

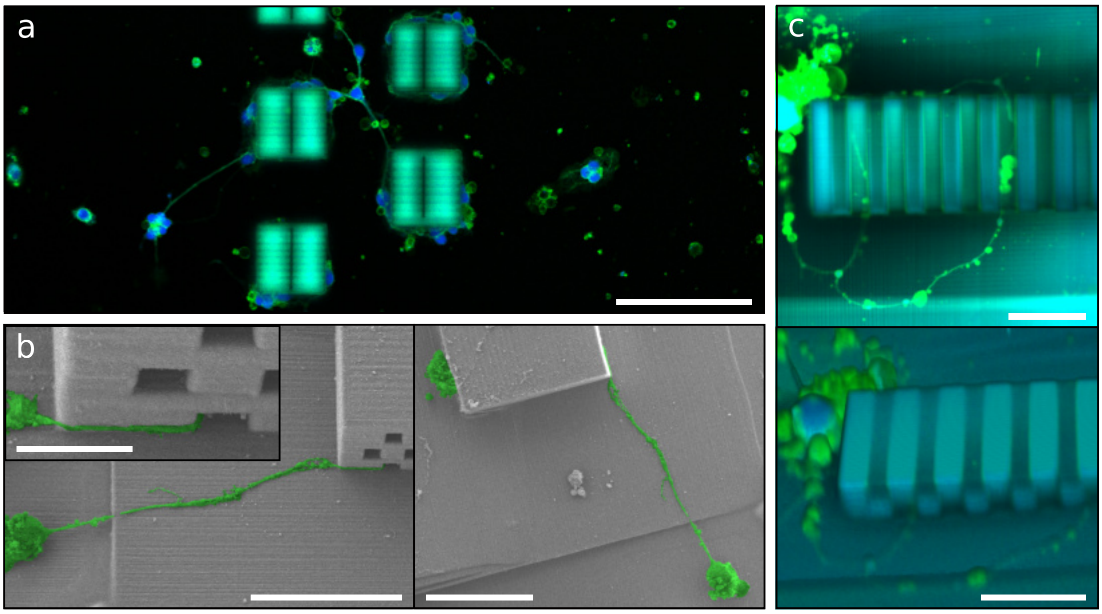

**Figure 6.6.:** Results of cell adhesion and neurite outgrowth tests with cubical test structures written by DLW. (a) CLSM images of stained granular cells cultured on a glass slide with cubical structures at 8 DIV. (b) False-colored SEM images of a neuron with a neurite extending inside a tunnel with a cross section of 2×2 µm$^2$. The insert shows a close up of the neurite and the entrance of the tunnel. (c) CLSM images of a living cell (yellow/green soma) with neurites extended through tunnels with a cross section of 4×4 µm$^2$. Scale bars: 100 µm (a), 20 µm (b, c), 5 µm (b insert).

glass carrier and polymer, with neurite connections in between. High density of vital cells at the cubes shows that the polymer is not cytotoxic. Low cell density on the flat glass carrier in proximity to the cubes indicates cell migration towards the structures after cell planting.

Even though neuronal network formation around the polymer cubes is observed, no cells or neurites are directly attached on top or on the sidewalls of the cubes. However, in the targeted pillar structures, cells are supposed to attach inside of polymer cavities. Therefore, flat IP-DIP surfaces were utilized as platforms for cell adhesion to test attachment directly on polymer. The IP-DIP platforms are connected with springs to the glass carrier analogous to scaffolds in boxes (see Section 5.2.3). Cubical structures with straight tunnels opening to opposing sides were written on top of these platforms to evaluate their function as neurite guides.

The cell density on top of the polymer substrates is very low compared to control cultures on the bottom of Petri dishes (Appendix Figure A.3). Cell vitality on the IP-DIP platforms is significantly diminished to the extent that only single vital neurons can be found on top of the material. Figure 6.6 b shows one exemplary neuron settled on the polymer at 7 DIV. The neurite is extended towards an edge of a cubical over a distance of approx. 40 µm and further along the low edge between cube and flat substrate. With a turn of 90 °, it enters the first bottom tunnel and extends towards cellular material on the other side of the cube. The small step crossed by the neurite is an artifact caused by write field stitching. Figure 6.6 c shows one living cell attached near the side of a cube. Neurite outgrowth has occurred through the first and the fifth bottom tunnel of the cube, forming two closed loops. The cell soma is enclosed by dead cellular material originating most probably from dead neurons.

In conclusion, adjustments are mandatory to significantly improve cell attachment and vitality on cell culture platforms for neuronal network building that consist of IP-DIP polymer. In case of surviving neurons, a majority of axons extended towards and through cubes and tunnels, confirming a guidance effect of tunnels produced by DLW. In contrast to axons in microchambers, where a straight trajectory prevails over edge guidance for turns over 84 ° and edge guidance prevails only for turns under 26 ° (see Section 2.5.3), the observed axons entered tunnels independent of the entrance angle.[113] The growth cone more likely extends into tunnels than further along the open flat area, which indicates a dominance of edge guidance over trajectory, if the edge leads to additional confinement. Once inside a tunnel, neurites are guided completely to the opposite side. Reversal of neurites inside the tunnels is not observed at all.

### 6.2.2. Culture in 3D Structures Depending on PDL Coverage

As a basic idea of the scaffold design, cell adhesion onto the 3D pillar structures is only desired inside of the cavities. That premise is a requirement for guided growth on tailor-made routes defined by tunnels. In the first approach, coating of PDL and laminin was applied nonspecifically on the entire sample. In accordance to the low cell attachment observed on flat IP-DIP polymer, cultivation of a bare IP-DIP tower structure in this configuration does not result in network building or neurite guidance due to the near absence of vital granular cells attached to the structure. Possible reasons for this effect can be unfavorable roughness and stiffness of the structure surface and a surface chemistry of IP-DIP that is unfavorably for cell adhesion and survival. As a first approach for improvement, the structures were coated with ParC and $Al_2O_3$ before culturing

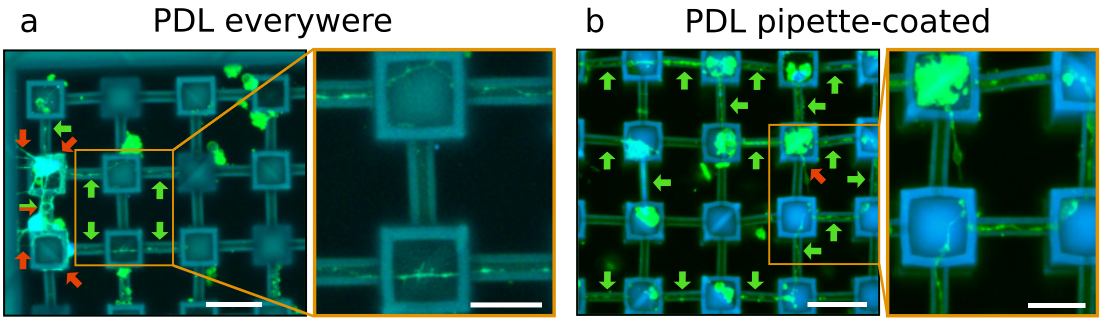

**Figure 6.7.:** CLSM images of a cultured 3D scaffolds. Green arrows point to neurites inside of tunnels. Red arrows point to neurites grown outside of the tunnels. (a) Scaffold coated with ParC at 7 DIV. A PDL droplet covering the entire structure was incubated for 1 h before culturing. (b) Scaffold coated with $Al_2O_3$ and PDL coated directly into the cavities and tunnels before culturing using a glass pipette (10 DIV). The ratio of neurites inside the tubes is significantly improved compared to (a). Intensity differences are caused by slightly different imaging settings and use of different detectors. While (a) was detected by two HyD detectors, in (b) the range of 494 - 540 nm was detected with a photomultiplier tube (PMT) detector with gain set to 900. Scale bars: 40 µm and 20 µm (zooms).

(see Section 5.3). Figure 6.7 a shows a representation of the culturing results for these substrates at 7 DIV. Some neurons are settled on the substrates - on the inside as well as on the outside of the cavity walls. Neurites on the outside of the cavities are extended around the cultured towers and also attach to the box surrounding the tower structure. Neurites from somata settled on or near the bottom inside the cavities are extended through the tunnels. All neurites extended through tunnels stayed inside the cavities, indicating topological neurite guidance inherent to the structure design. Overall, while some neurons settled inside the cavities by chance, the number of neurons attached to the outside of the pillars in a randomly distributed fashion is larger. Settling on top of the structure might be preferred by the cells due to increased surface area and the possibility to freely move and agglomerate, which is in contrast to the confinement inside of the cavities.

The results show that with purely statistical adhesion of the cells onto the scaffold, the attraction of cavities for soma adhesion is not sufficient to build ordered neuronal networks in 3D. To give additional chemical guidance of the cells towards the cavities during the settling process, PDL solution is directly filled into cavities and tunnels with glass pipettes controlled by a micromanipulator (described in detail in Section 5.3.3). Utilizing this method, PDL as a cue for cell adhesion is only present inside of the cavities and tunnels. As before, laminin is still coated onto the entire sample directly before culturing. Figure 6.7 b shows an example of the culturing results with selective PDL coating on a $Al_2O_3$ surface. Most cell attachment to these structures is confined to the cavities. Many somata are attached to the bottom of the cavities. A vast majority of neurites is extended through the tunnels, leading to formation of neuronal networks in the structure. Single neurites leaving the targeted area over the cavity walls can only be observed when clusters of multiple cells are attached in one cavity. The fact that the scaffold is still completely coated with laminin verifies the predominant effect of PDL for soma attachment and neurite guidance of MCGCs in the 3D structures. The combination with selective PDL coating turns the cavities into effective neuro-cages. If a soma was settled in a cavity, it stayed in that cavity for an examined period of up to 14 DIV.

Note, $Al_2O_3$ coating resulted in slightly more cell attachment compared to ParC coating, which is in accordance to reference measurements, where $Al_2O_3$ coating resulted in higher cell attachment and vitality (see Section A.1.2). Thus, all scaffolds cultured with MCGCs discussed henceforward are coated with a $Al_2O_3$ surface layer.

### 6.2.3. Neurite Guidance and Network Building

The previous section successfully established the efficiency of the proposed structure design of alternating cavities and tunnels as neuro-cages and neurite guides. In this section, the pathway of neurites inside of the tunnels and the efficiency for the formation of neuronal networks is analyzed.

Z-stacks obtained by confocal imaging are used for evaluation of neurite pathways inside the scaffolds. The intensity of single neurites inside the structure in stacked images can be insufficient for clear visibility against the fluorescence signal of the scaffold, especially for neurites with small diameter. However, in cross sections of these stacks, no visual information is lost and the exact positioning of all neurites over the entire path can be visualized. Examples of stacked CLSM images and corresponding cross sections from two different cultures at 8 DIV that display neurites in the structure are shown in Figure 6.8 a b and Figure 6.8 c d, respectively.

In Figure 6.8 a and b, cross sections 1 - 3, 9 - 10 and 14 - 15 display adhesion of neurites in changing edges throughout the tunnels, while 5 - 6 and 7 display neurites sticking to one edge. 1 - 3 show multiple edge switching of a neurite in a single tunnel from the bottom right (1) to the top left (2) to the bottom left

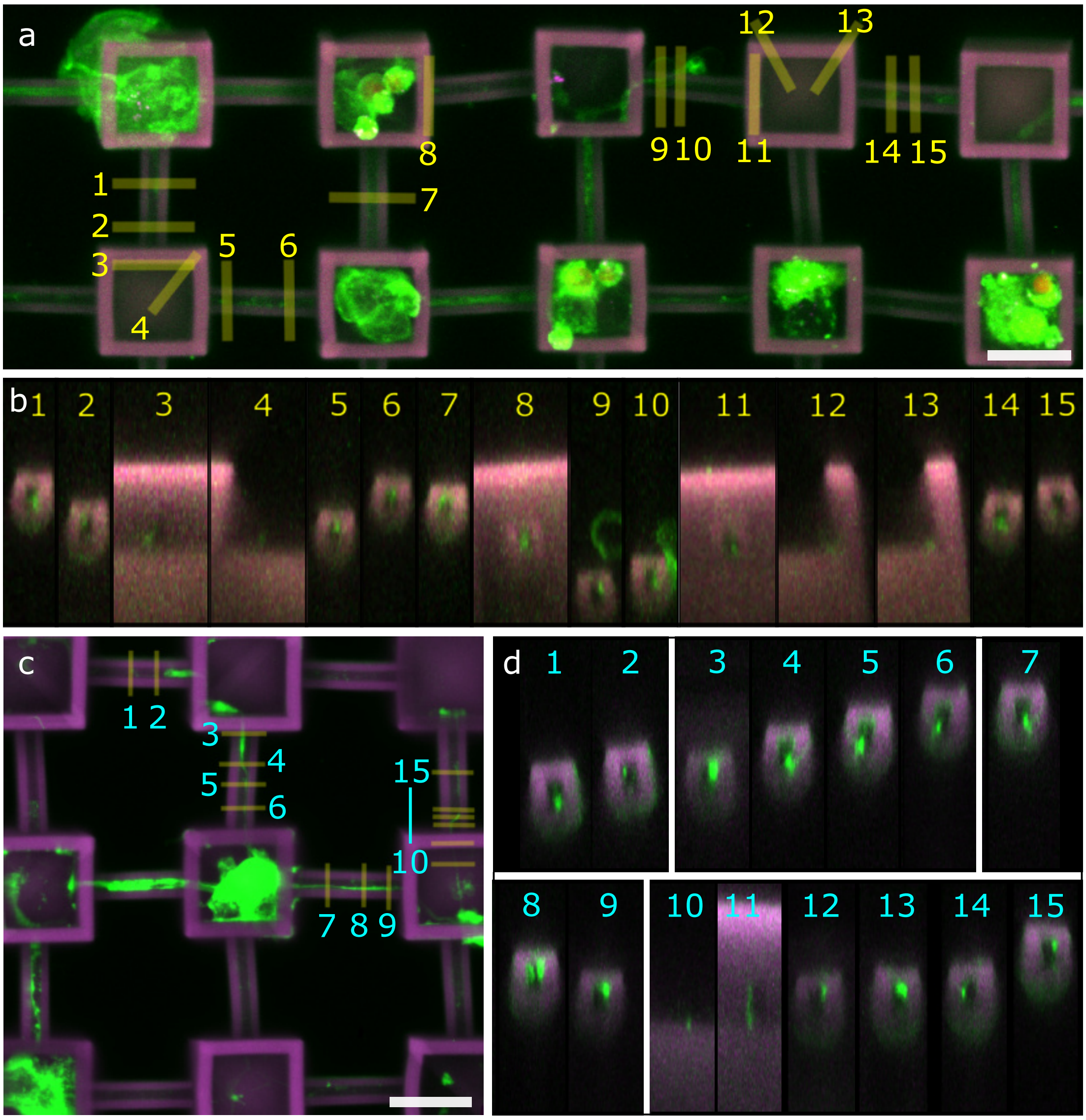

**Figure 6.8.:** Stacked CLSM images of neurons at 8 DIV inside of 3D structures. (a) Top view onto a culture scaffold. Numbered lines mark positions of the corresponding cross sections displayed in (b). (c) Top view onto a culture scaffold and (d) the corresponding cross sections. Scale bars: 20 µm.

(3). Cross sections c 9 - 15 show a neurite that is hidden in the stacked image (a 9 - 15), but clearly visible in the cross sections. The neurites inside tunnels displayed in Figure 6.8 c and d change edges multiple times. Cross sections b 9 - 10 display a single neuron attached outside of the tunnel. One neurite from this neuron is extended directly into the next cavity. A second smaller neurite is extended into the other connected cavity, visible as a green dot on top of the cavity wall in b 11.

When crossing a cavity before entering another tunnel, two distinct behaviors of the neurites can be observed. Most neurites are extended on a relatively straight path through the cavity towards the next opening, (b 4 and d 10). In rare cases, neurites inside cavities stick to the edges between cavity ground and wall before entering the next tunnel (b 12 - 13). Cross sections d 10 - 15 show a neurite that at the opening of a tunnel appears to originate from d 10 and at d 11 directly extends from the cavity bottom to a top edge of the tunnel.

Samples were fixated, dried and sputtered with gold to allow for high resolution SEM images of cell cultures in 3D substrates and to further analyze the network formation. Figure 6.9 shows paths on which axons of immature MCGCs at 3 DIV and mature MCGCs at 8 DIV are extended through tunnels and cavities. The utilized scaffolds are directly written onto glass carriers. The depicted neurons well exemplifies typical behavior of neurons observed inside the scaffolds. Originating from the axon hillock, a majority of axons is directly extended towards the tunnels. Axons enter and leave the tunnels directly at the edges. Neurites were previously observed in CLSM to not only attach to bottom edges at the entrances of tunnels, but to pass over directly from the cavity bottom to top edges. The SEM images confirm that axons can directly attach to top edges of tunnels originating from the soma. Two different behavioral settings can be observed inside the tunnels. Axons keep attached to the same edge over the entire length of tunnels or detach from one edge, cross a sidewall of the tunnel and attach to another edge. Note, since FIB milling is needed to visualize the interior with SEM, neurites switching edges in lateral direction are partially removed with this method (Figure 6.9 d). In between the tunnels, axons mostly take the direct path in between. They either extend straight across the bottom of the cavities or take two turns of roughly 45 °. In some cases, an axon pathway has a fork and leads to three or four tunnels. In accordance to the critical release angle of 84 °, reaching the tunnel exit, where the edge leads in a right angle, the growth cone of an axon detaches from the edge and extends the axon into the cavity.

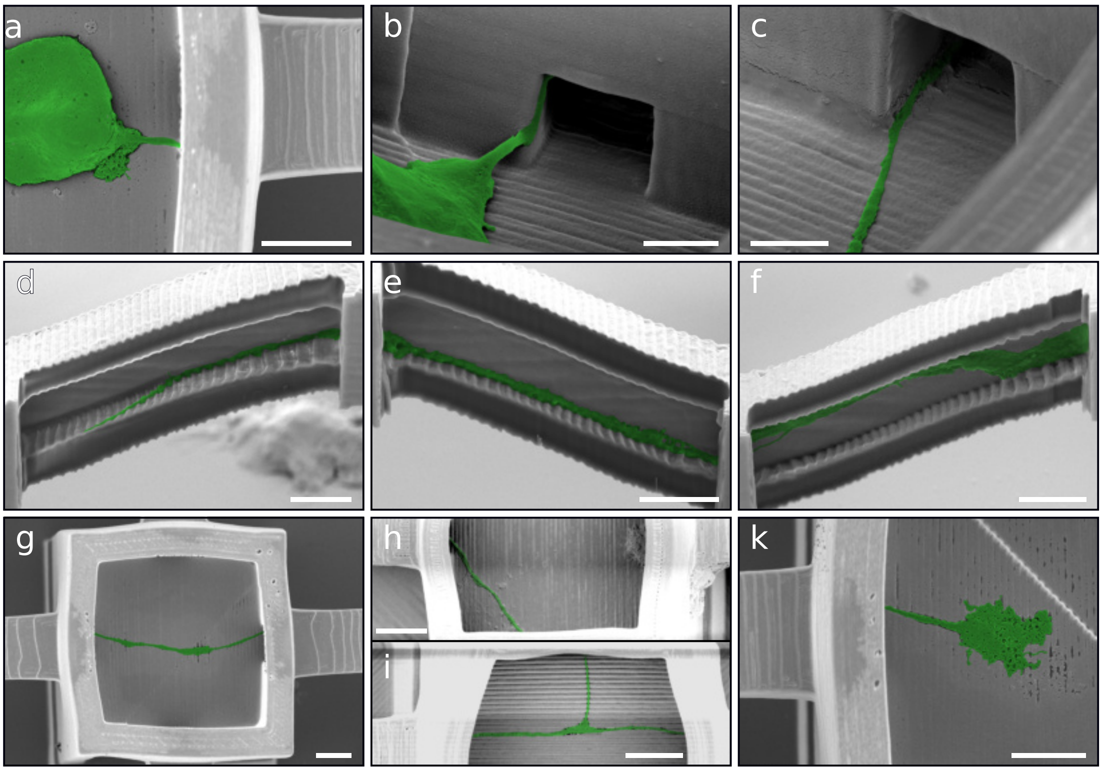

**Figure 6.9.:** False-colored SEM images of depicted neurons after 3 DIV (a-g,i) and 8 DIV (h) inside of 3D structures. Cross sections were obtained by FIB milling. The cellular extensions are clearly identifiable as axons by growths cones and axon hillock origin. (a) Top view of cell soma and axon in a cavity with the axon entering a tunnel. (b) Side view of cell soma and axon in a cavity with the axon extended into the top left edge of a tunnel. (c) Axon enters a tunnel at the bottom left edge after crossing a cavity. (d) An axon in a tunnel changing diagonally to the bottom left edge and sticking to that edge until it reaches the next cavity. (e) The same axon as in (d) crossing a second tunnel. It sticks to the bottom left edge over the whole distance. (f) A bundle of neurites guided first in the top left edge, switching to the bottom. The cellular material widened during the edge change, likely consists of growth cones fixated in the process of sensing the tunnel exit. (g) An axon crossing one cavity and entering a second tunnel on the opposite side. (h) Axon turning towards a tunnel connected in a right angle inside a cavity. (i) Axon pathway splitting in a cavity and leading both straight across as well as in a 90 ° angle. (k) An axon leaving a tunnel, ending in the growth cone. Scale bars: 4 µm (a,d-k), 2 µm (b-c).

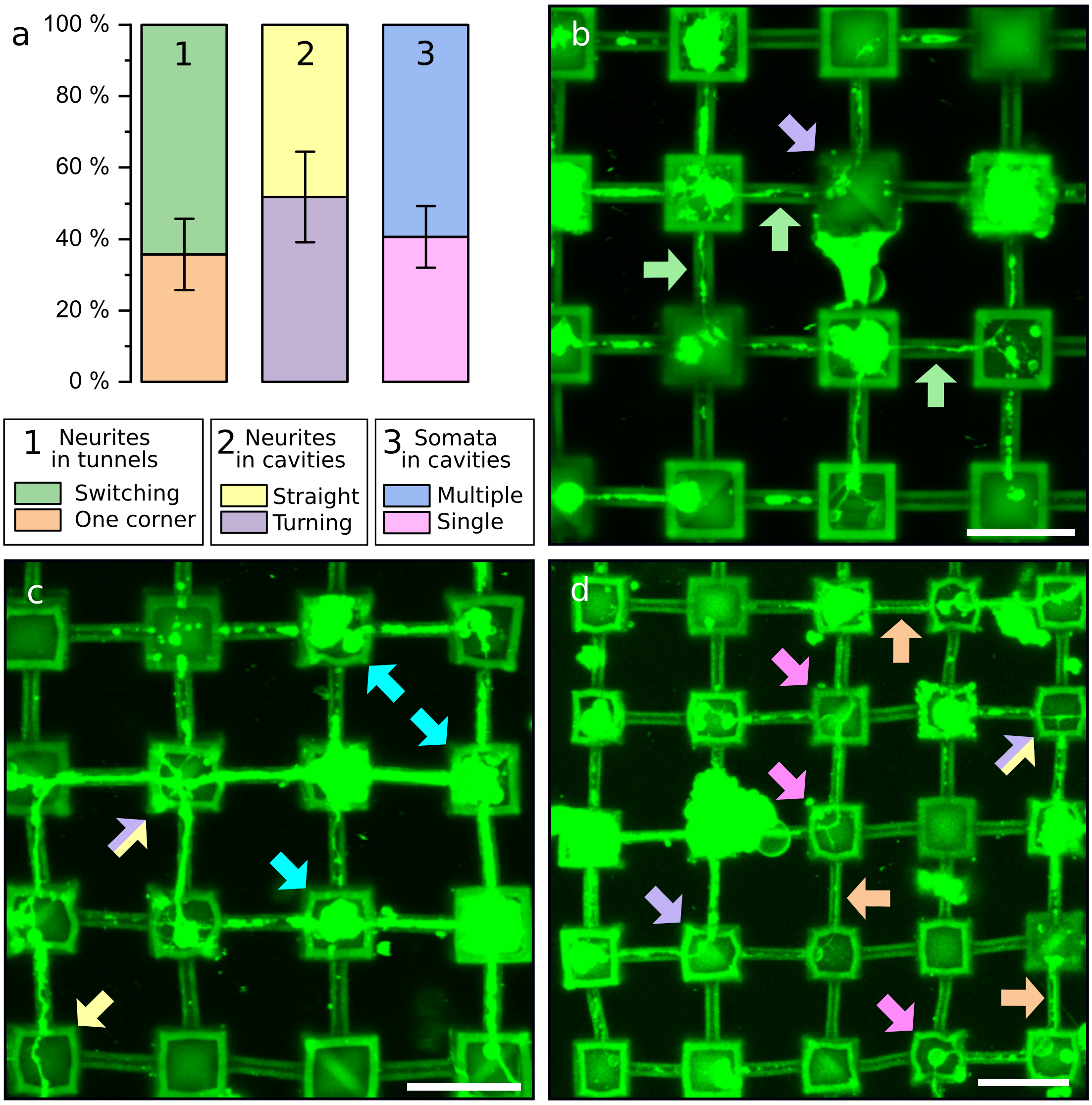

**Figure 6.10.:** (a) Distributions of (1) neurites crossing tunnels in a single edge and switching between multiple edges ($n = 85$), (2) neurites extended through cavities straight towards the tunnel on the opposite side and turning 90 ° towards a tunnel connected in a right angle ($n = 85$), (3) cavities containing single and multiple somata ($n = 121$). Values are distribution ± 95 % confidence level (adjusted Wald interval). (b-d) CLSM images of neuronal networks inside of 3D scaffolds (10 DIV). In order to visualize single neurites with small diameter despite intrinsic autofluorescence of the IP-Dip polymer in the stack, only one wavelength (552 nm) was used for excitation. Examples for neuronal behavior analyzed in (a) are marked by correspondingly color-coded arrows. Mixed purple/yellow arrows point to cavities containing both straight and turning neurites. Scale bars: 40 µm.

The neurite pathway in tunnels and cavities as well as soma attachment in cavities are further characterized based on data obtained by CLSM (Figure 6.10 a). Figure 6.10 b - d displays stacked CLSM images of parts of neuronal networks at 10 DIV. Examples of the analyzed features of the network are highlighted in the images by arrows in colors corresponding to the plots. Only single extensions with a clearly defined path are included in the count of neurite pathways in tunnels. More neurites switching edges in tunnels (64 %) are observed than neurites attached to only one edge (36 %). For the characterization of pathways of neurites between tunnels, cavities containing somata in addition to neurites are excluded. Cavities that contain straight and turning neurites are included with one count for each category. The count is equally distributed, with 52 % of the neurites turning towards a tunnel on the left or right and 48 % following a straight trajectory to the tunnel on the opposite site. 41 % of cavities in which neurons have settled contain one single soma, while 59 % contain two or more somata.

The size distribution of the neuronal networks in the 3D structures is plotted in Figure 6.11. At least two neurons in separate cavities have to be connected to each other to be included in the count. The smallest observed network ranges over three cavities with two somata connected over the distance of two tunnels and one cavity. The largest analyzed network has somata settled in 26 cavities with a total of 45 cavities and 47 tunnels involved in the network. The mean network range is 13.4 for cavities and 15.2 for tunnels. Somata were settled in a mean of 7.6 cavities per network.

In summery, neuronal networks have successfully been cultivated inside of the 3D structures. Neurites have spread through the tunnels and build networks within the boundaries defined by the scaffold design. Single somata attached to tunnels outside of the structure have extended their neurites over the cavity walls into the confinement of the design and contribute to the neuronal networks. Since this behavior is not observed without selective PDL coating, it can be concluded that the neurites are guided into the structure by chemical attraction. A vast majority of somata are settled inside the cavities. Thus, the goal to combine neurocages and neurite guides in one 3D scaffold is fully satisfied.

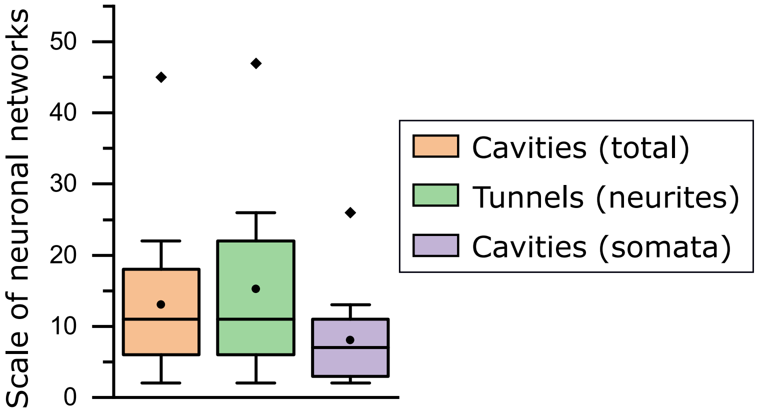

**Figure 6.11.:** Box plots of the scale of MCGCs neuronal networks in 3D structures analyzed with CLSM ($n = 13$). The plots represent the total number of tunnels and cavities as well as the number of cavities containing somata within individual continuous networks. At least two individual neurons in seperate cavities have to be connected to be included. Boxes: 25 % - 75 % range, line: median, dot: mean, whiskers: range within 1.5 $*$ interquartile range, diamonds: outliers.

## 6.3. Humane Neuronal Networks in 3D Structures

In succession to successful culturing of ordered neuronal networks of MCGCs, the 3D scaffolds are tested as culture platforms for humane mDANs. Humane neurons derived from smNPCs are of major interest for medical research (see Section 2.6) and the perspective of obtaining ordered neuronal networks on adjustable 3D substrates from these neurons can be a first step to the fabrication of innovative new medical devices.

### 6.3.1. Approach 1

In the first approach to transfer mDANs from a well plate onto the scaffold, small droplets of cell suspension are deposited and left to settle for 1 h, before maturation medium is added. Surface coating with $Al_2O_3$ as well as ParC is tested. PDL is selectively coated into the structure with the use of a micromanipulator.

With $Al_2O_3$ coating, most somata are settled inside the scaffold and neurites are guided inside the tunnels (Figure 6.12 a). Some cell extensions that form bridges with a trajectory out of one cavity, running parallel above a channel towards a second cavity and leading over the wall back down into this cavity (Figure 6.12 b - c). The overall attachment of cells outside of the scaffold is

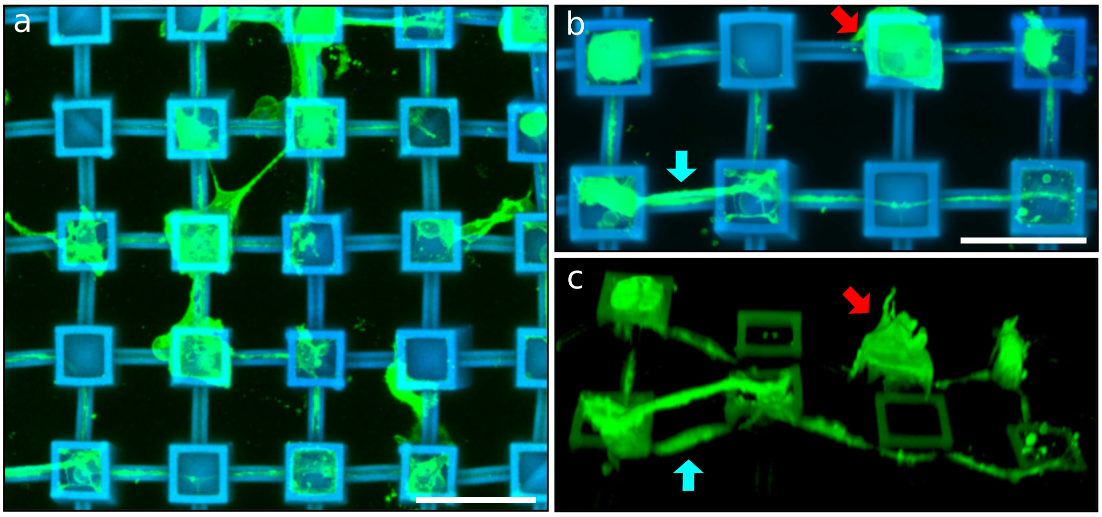

**Figure 6.12.:** CLSM images mDANs transferred using approach 1 onto 3D structures coated with $Al_2O_3$. PDL is selectively coated inside of the structure. (a - b) Top view onto cultured scaffolds. (c) Side view of the section displayed in (b). Blue arrows indicate a cell bridging between cavities running parallel above a channel. Red arrows indicate a divergent cell on top of a cavity. Scale bars: 50 µm.

higher than for MCGCs. However, it is important to note, that during the differentiation of smNPCs into mDANs part of the cells form different cell types.[173] Detailed analysis of gene expression patterns beyond the scope of this work is needed to determine the distribution of cell types in and on the substrates with certainty. But by evaluation of the CLSM images available, a majority of cells outside the scaffold appear to be cells different to neurons, while most cells settled inside the scaffold have the morphology of neurons. Attachment of divergent cells might be preferable outside rather than inside of the scaffold, in order not to hinder the formation of neuronal networks.

With ParC coating, only a low degree of neurites are observed inside of the structure (Figure A.2). Most of the cellular network expands on top of the scaffold. Thus, $Al_2O_3$ is utilized as coating material for all cultures described henceforward.

### 6.3.2. Approach 2

In the second approach to transfer mDANs onto 3D scaffolds, medium is first added onto the structure and cell suspension is subsequently pipetted into the medium. Simplified structures with 4 × 6 pillars of identical height are cultured this way with humane mDANs. Characterization of the networks is

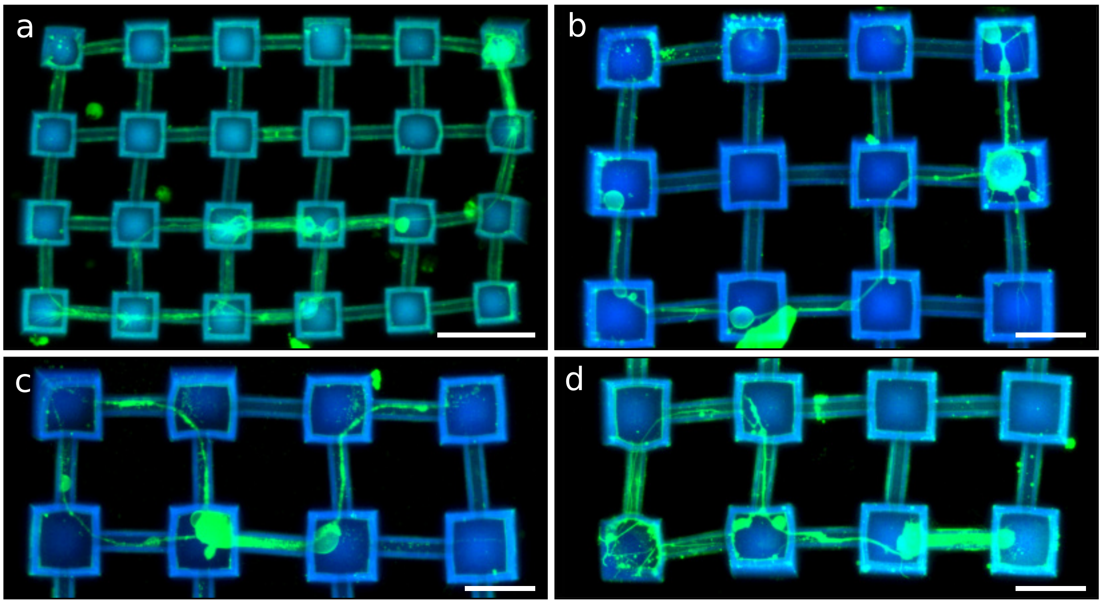

**Figure 6.13.:** CLSM images mDANs cultured on 6 × 4 pillar structures using the second approach. Scale bars: 50 µm (a), 25 µm (b-d).

facilitated in these structures due to reduced fabrication and imaging time (see Section 5.2.4).

Small, well defined networks of connected neurons expand through the interior of the structures (Figure 6.13). The occurrence of divergent cells attached to the scaffold is significantly reduced. Note, the cells cultivated in this approach originate from a different passage than the cells examined in the previous paragraph with higher efficiency in the differentiation of mDANs. However, control cultures from this passage using the first approach show that the second approach also results in reduced attachment of divergent cells for the identical passage.

Figure 6.14 a shows characterization results for soma attachment and neurite pathways through tunnels and cavities in the simplified structures analogous to the previously described evaluation of murine networks in 3D structures (see Figure 6.10). CLSM and optical microscope images were analyzed to determine the proportion of single vs. multiple somata inside the cavities. Additional statistics are solely based on CLSM evaluation of cultured scaffolds. 57 % of the observed neurites switch edges inside of tunnels, 43 % stay in one edge. The number of straight and turning neurites in cavities is nearly equal with 51 % straight and 49 % turning. A clear 70 % majority of cavities contain single somata, while 30 % of cavities contain clusters of two or more somata.

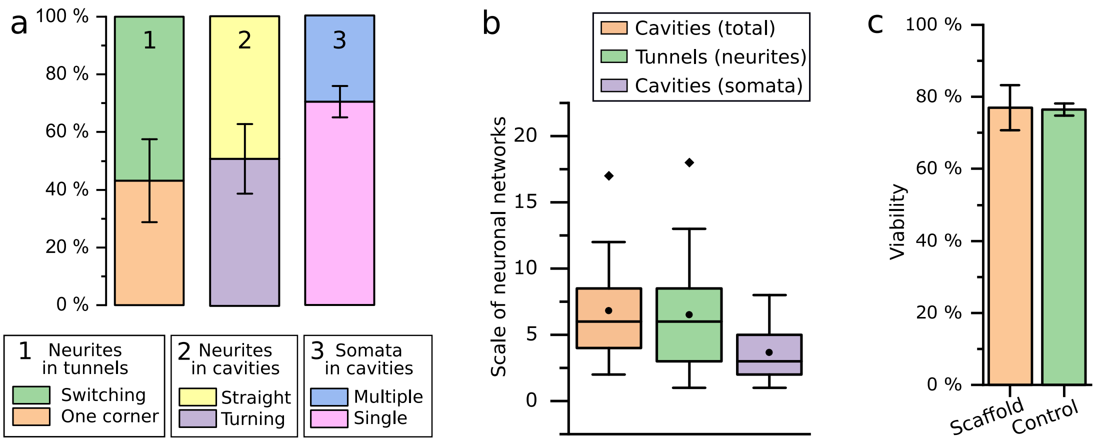

**Figure 6.14.:** Characterization of humane neuronal networks in 6 × 4 pillar structures. (a) Distributions of (1) neurites crossing tunnels in a single edge and switching between multiple edges ($n = 42$), (2) neurites extended through cavities straight towards the tunnel on the opposite side and turning 90 ° towards a tunnel connected in a right angle ($n = 63$), (3) cavities containing single and multiple somata ($n = 273$). Values are distribution ± 95 % confidence level (adjusted Wald interval). (b) Box plots of the scale of neuronal networks 1 - 4 days after transfer in simplified 3D structures analyzed with CLSM ($n = 24$). The plots represent the total number of tunnels and cavities as well as the number of cavities containing somata within individual continuous networks. At least two individual neurons in seperate cavities have to be connected to be included. Boxes: 25 % - 75 % range, line: median, dot: mean, whiskers: range within 1.5 × interquartile range, diamonds: outliers. (c) Cell viability in scaffolds and controls 1 - 4 days after transfer. Values are mean ± SEM.

The behavior of neurites inside the structure is consistent with the results for MCGCs with slightly less switching of corners inside the tunnels. The proportion of single somata settled inside of cavities is significantly increased, which leads to the formation of simpler networks with more defined order.

The analyzed networks range from two separated somata that are connected through one single tunnel to neuronal networks spread through 18 tunnels and a total of 17 cavities (Figure 6.14 b). A maximum number of eight cavities that contain somata was observed twice. The mean network range is 6.8 cavities and 6.5 tunnels. Somata were settled in a mean of 3.7 cavities per network. Cell viability in these networks is equal to viability in control cultures (Figure 6.14 c).

Overall, well defined neuronal networks formed inside of the 6 × 4 pillar scaffolds. The outgrowth behavior of neurites in the scaffolds shows no significant difference from MCGCs. The rate of single somata is significantly higher than in cultures with MCGCs, leading to a higher degree of order in the networks.

## 6.4. Neuronal Activity

The main property of neurons is the ability to receive and transfer information in form of electrical impulses over long distances in a neuronal network. In general, the electrophysiological behavior and activity of neurons is highly dependent on their environment.[310, 311] Therefore, verification of proper neuronal behavior of cells inside the structure, i.e. the ability of the neurons to transmit electrical signals in form of action potentials, is of high importance for future experiments on neuronal networks cultured inside of scaffolds based on the design presented in this work. The electrophysiology of MCGCs and mDANs was recorded with patch clamp measurements. Figure 6.15 displays the patch clamp process inside the pillar structures. MCGCs as well as mDANs show characteristic neuronal activity in the firing of action potentials. The electrophysiology of the mDANs is analyzed in detail in the following paragraphs. Exemplary current clamp recordings of MCGCs are displayed in Figure A.6.

### Activity of Humane mDANs Derived from smNPCs

Neuronal networks in $6 \times 4$ pillar structures, such as the ones characterized in Section 6.3.2, were utilized for a detailed statistical analysis of the electrophysiological response of humane mDANs in the scaffolds. Besides the capability of the neurons to fire action potentials, inward and outward currents through the cell membrane were recorded to test the electrophysiological maturation of the

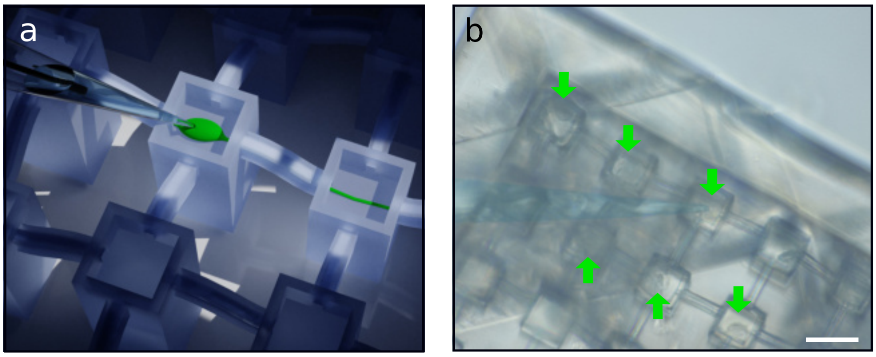

**Figure 6.15.:** (a) CAD graphic of the patch clamping process in the 3D structure. The patch pipette approaches the substrate in an angle of 45°. One electrode is inside the patch pipette, the ground electrode is outside of the structure in the bath solution. (b) Optical microscope image of a patched neuron inside the structure. The arrows point to cavities that contain single somata. The pipette is false-colored for visibility. Scale bar: 25 µm.

neurons. An exemplary recording of current clamp measurements of mDANs in the scaffolds is displayed in Figure 6.16 a. Small injected currents from 6 pA upward lead to sufficient depolarization of the cell membrane to trigger firing of action potentials in the cells. Voltage clamp measurements (Figure 6.16 b) reveal fast-activating and -inactivating inward currents at the beginning and subsequent slow-activating and -inactivating outward currents. These recordings demonstrate regular activity of voltage-gated $Na^+$ and $K^+$ channels of cells cultures within the structures. (see Section 2.3).[312, 313] The inwards currents can be associated with $Na^+$ channels that quickly move into an open configuration upon depolarization of the membrane, which leads to influx of $Na^+$ ions, swiftly followed by another conformational change towards the inactive channel state. Slow $K^+$ channel activation leads to increasing $K^+$ ion outward current in a delayed response to depolarization of the membrane. The correlation of the peak inward and outward currents with the respective ion channels is supported by characteristic I-V plots of the peak currents (Figure 6.16 c).

Signature properties of neurons that are derived from patch clamp recordings of mDANs in the scaffolds (Sc.) as well as mDANs of control cultures (Co.) are plotted in Figure 6.16 d.[314] Reference data for typical values in mammalian neuron types can be obtained as comparison from NeuroElectro.[315, 316] The mean input resistance of the cells is $4.8 \pm 0.9\,\mathrm{G\Omega}$ (Sc.) and $4.8 \pm 0.8\,\mathrm{G\Omega}$ (Co.). It is affected by the size of the cells and the number of open ion channels in the membrane. Typical magnitudes for mature mammalian neurons range from high MΩ to low GΩ depending on the neuronal type. The values obtained here are exceptionally high, which fits small somata, but additionally indicates a low amount of open channels at RMP. The mean membrane time constant - indicating the time the membrane needs to repolarize after the injection of small currents - is above average with is $61.5 \pm 16.3\,\mathrm{ms}$ (Sc.) and $62.4 \pm 16.8\,\mathrm{ms}$ (Co.). The membrane capacitance is linearly related to the membrane time constant and input resistance and thus is also near to equal in scaffold and control cultures with $8.6 \pm 1.3\,\mathrm{pF}$ and $8.8 \pm 1.7\,\mathrm{pF}$, respectively. The values are typical for neuronal cell types with small somata. The RMP of cells in the scaffold is slightly higher ($-58.9 \pm 2.4\,\mathrm{mV}$) than the RMP of cells of the control ($-53.2 \pm 1.9\,\mathrm{mV}$). It is normal to above-average for mammalian neurons. The mean spike threshold ($-29.7 \pm 2.0\,\mathrm{mV}$ (Sc.) and $-28.7 \pm 1.2\,\mathrm{mV}$ (Co.)), the mean spike amplitude, which is the difference between action potential thresholds and peaks ($76.4 \pm 4.5\,\mathrm{mV}$ (Sc.) and $74.1 \pm 4.4\,\mathrm{mV}$ (Co.)) and the mean spike duration, defined as the FWHM between threshold and peak ($4.6 \pm 0.4\,\mathrm{ms}$ (Sc.) and

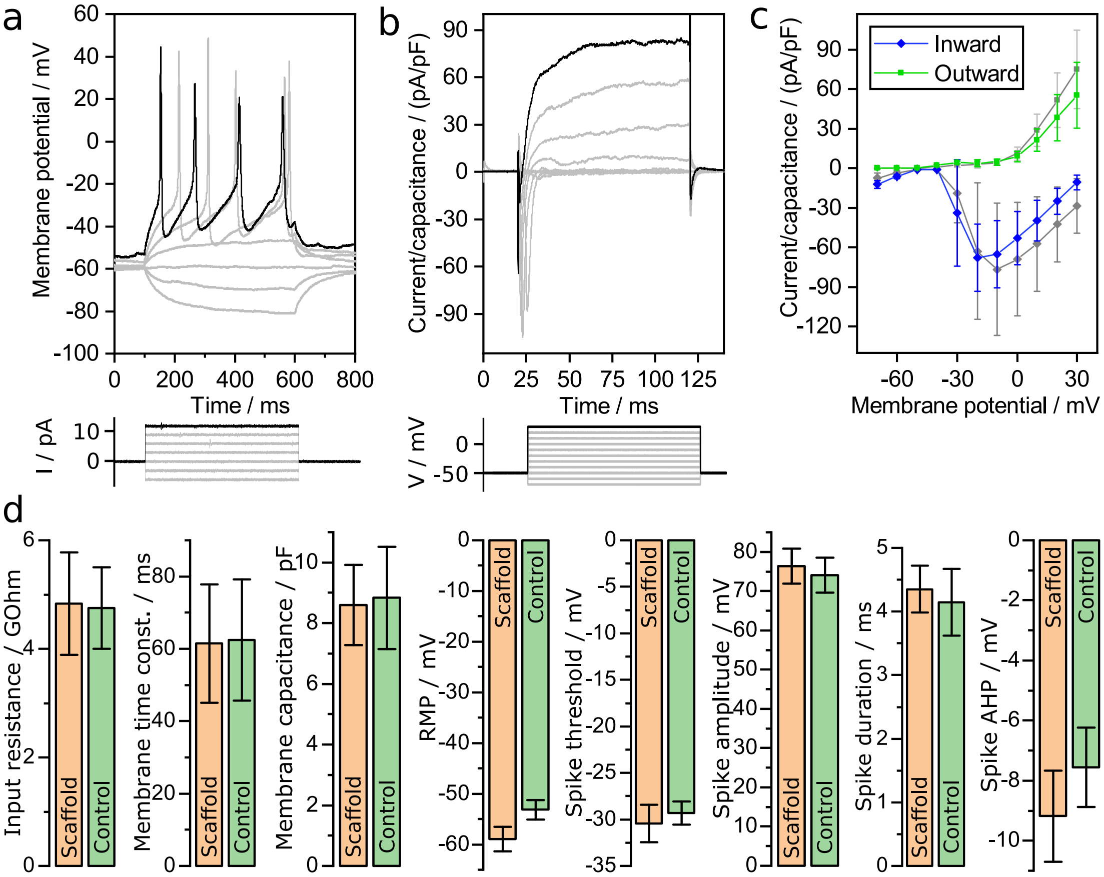

**Figure 6.16.:** Electrophysiological characterization of humane mDANs in 6 × 4 pillar structures. (a) An example of current clamp recordings of action potential spikes. Current steps were applied for 500 ms from -6 pA to 12 pA in 3 pA increments. (b) An example of voltage clamp recordings of inward and outward currents through the membrane channels. Voltage steps were applied for 100 ms from -70 mV to 30 mV in 5 mV increments. (c) Current-voltage characteristics of inward and outward currents of cells in scaffolds (n = 6, black) and control cultures (n = 6, gray) measured on the peak and normalized to cell capacitance. (d) Data analysis from current clamp and voltage clamp recordings of the cells in scaffolds (n = 6, orange) and control cultures (n = 9, green) show (from left to right): input resistance, membrane capacitance, resting membrane potential (RMP), spike amplitude, spike duration, spike threshold, spike after hyperpolarization (AHP) and membrane time constant. Values are mean ± standard error of mean.

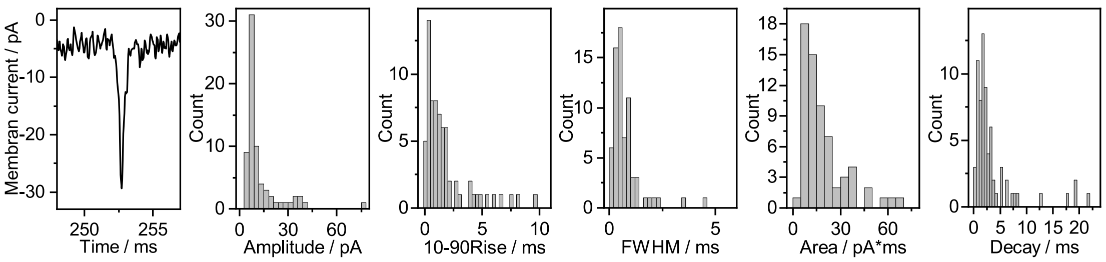

**Figure 6.17.:** Spontaneous synaptic activity. (a) Exemplary recordings of a spontaneous postsynaptic current of mDANs in scaffolds. (b - f) Distributions of characteristic properties of postsynaptic currents of mDANs in scaffolds (n = 5). Means ± standard error of the mean: Amplitude: 13.9 ± 1.9 pA; 10 - 90 Rise: 1.8 ± 0.2 ms; FWHM: 0.8 ± 0.1 ms; Area: 27.2 ± 4.0 pA × ms; Decay:3.5 ± 0.5 ms. Analyzed with MiniAnalysis, event detection threshold: 5x RMS Noise, n = 5 cells.

4.4 ± 0.5 ms (Co.)) are all in the normal range of mammalian neurons with little to no difference between scaffold and control. The spike after hyperpolarization is slightly higher for cells in the scaffolds (-9.5 ± 1.5 ms) as for cells of the control(-7.5 ± 1.3 ms). Both values are in the average range.

Cells in scaffolds and cells from control cultures have very similar electrophysiological properties. No significant deviations are identified by analysis of variance with $P < 0.05$. Only the RMP and spike after hyperpolarization vary more than one standard error from each other. The RMP standard errors do not overlap. In both cases, the lower values in the scaffold are in favor of neuronal activity of mDANs after maturation. Overall, all analyzed values are in the expected range for mature neuron with the exception of the mean input resistance. However, a high input resistance means that the cultivated humane mDANs are sensitive to small voltage changes, which might be favorable in the signal transmission through low density neuronal networks.

Existential for neuronal function is not only the proper activity of membrane channels and the firing of action potentials with correct electrophysiological properties, but also the ability to transmit the action potential signals through the network via synaptic activity. The formation of functional synaptic connections, and thus the potential of neuronal network activity, is tested by the recording of spontaneous postsynaptic currents.[317] The recordings were performed on mDANs (n = 5 cells) in the scaffolds in voltage clamp mode with a constant holding potential of −70 mV (Figure 6.17). Spontaneous postsynaptic currents were measured with a mean amplitude of 13.9 ± 1.9 pA. The analysis shows that the kinetic parameters of the spontaneous postsynaptic currents are comparable to different mammalian neurons.[318–320]

All in all, the results of the electrophysiological measurements show that the pillar structures are well suited as cell culture platforms. The mDANs derived from iPSCs in the scaffolds have electrical properties of mature neurons. Spontaneous postsynaptic currents show that the neurons have developed synaptic connections. Thus, the patch clamp measurements demonstrate successful cultivation of low-density humane neuronal networks with network activity inside of the pillar-tunnel structure.

# Summary and Future Perspective

7

## 7.1. Summary

A new type of cell culture platform was realized utilizing the state-of-the art 3D micro- and nano-fabrication technology of DLW by 2PP. The concept combines chemical with topological guidance to define designated cell adhesion spots in form of cavities on top of towers with distinct 3D pathways for neurite outgrowth in form of free-standing tunnels that connect the cavities with each other. The formation of neuronal networks in the presence of topological and chemical constraints was evaluated with 2.5D neuron cultures on modulated surfaces produced with GSL, RIE and NIL The obtained findings served as base in the design of the 3D platforms. Cultivation experiments were performed with MCGCs as well as humane mDANs derived from smNPCs and confirm that the 3D cell culture platforms, when selectively coated with PDL, successfully combine caging of neuronal somata inside the cavities with guidance of neurite outgrowth through the tunnels. The neurons formed ordered neuronal networks within the limits defined by the structure. Neurons in the structure demonstrated electrical activity with electrophysiological properties similar to control cultures in patch clamp experiments. Postsynaptic currents verified the capability of the cultured neurons for network activity.

Cultivation of design variations of the introduced 3D cell culture platform showed that the design can easily be modified to change the geometry of the obtained neuronal networks with pillars of different height and tunnels whose path is freely arranged in all room directions. Thus, specific network requirements such as circular loops and 3D complexity are easily incorporated into the design. Low density neuronal networks with specific geometries can be cultivated on adapted 3D scaffolds based on the presented design.

## 7.2. Future Perspective

In the following, possible future experiments and approaches are presented to further improve the quality and scope of the 3D designer neuronal networks.

### Variations leading to Increased Complexity and Scale

As stated above, the presented design of towers and tunnels lays the foundation for complex designer neuronal networks in 3D. The arrangements chosen in this work were kept close to simple chessboard patterns to simplify the analysis of the obtained network patterns and ensure easy access to the cells for patch clamp recordings of the cells. The variety in tower heights and placements as well as tunnel length, orientation and number can easily be changed in the design to increase the complexity of formed networks and obtain 3D neuronal network configurations. The scale of the scaffolds and thus the resulting neuronal networks can be raised in xy-direction as well as in z-direction. State of the art DLW by 2PP technology can help to write scaffolds with millimeter dimensions in one single write field without stitching.

First tests on variations have already been performed as proof of concept that the base design can easily be adjusted to meet demands upon envisioned geometries of cultivated neuronal networks. A test-design with varying tunnel lengths and orientation was cultivated with MCGCs. Examples of culturing results in structures with this design are displayed in (Figure 7.1). Neurites grow through each type of tunnel present in the structure, from 25 µm to 100 µm tunnel length and through orientations from 0 ° to 90 °. The results demonstrate that a large variety of tunnel trajectories is feasible in future designs.

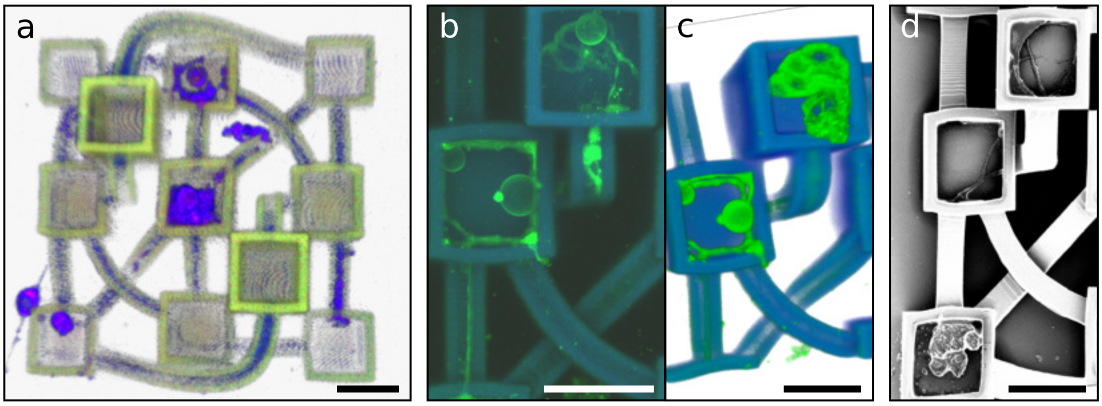

**Figure 7.1.:** MCGCs in a 3D scaffold with alterations in cavity heights and tunnel pathways. (a) CLSM top view onto a scaffold. (b) CLSM top view and (c) 3D projection of a scaffold section with a neurite extended through a horizontal and a vertical tunnel. (d) SEM image of a neuron extended horizontally and vertically through a structure. Scale bars: 20 µm.

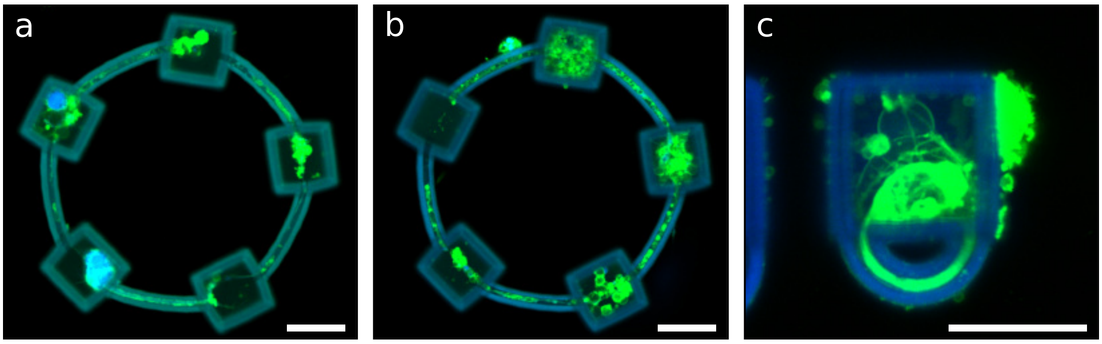

**Figure 7.2.:** CLSM images of neurons in ring structures. (a-b) Top view onto MCGCs in rings of 5 cavities and tunnels each. (c) Top view onto a single cavity with one semicircular tunnel connected to the same cavity with both entrances, cultivated with mDANs. Scale bars: 20 µm.

One additional pillar arrangement tested are ring structures (Figure 7.2 a - b). Neurite extensions in these rings are grown in a circle, potentially connecting only a few neurons with each other in a closed loop. These structures could be used to study action potential propagation and changes in excitability in neuronal feedback loops. The concept is amplified with tunnels leading back to their origin (Figure 7.2 c). The behavior is similar to previous observations for single neurons on isolated PDL circles (Section 6.1.2). The only possibility to interact for such a neuron is autapse - building synaptic connections between the axon terminal and its own dendrites or soma.[280] Autapse formation and neuronal loops could be important aspects in the construction of functional tailor-made neuronal networks to incorporate functionality of oscillators into neuronal networks and to provide the possibility to tune synaptic feedback when excitatory and inhibitory burst inputs are added.[282, 321]

### Improvement of Network Structure

One possible longterm perspective for the application of designer neuronal networks are logical circuits build from neurons. For this, a maximum of control over neuronal network formation is required. Ideally, only one neuron should be attached in each cavity and the direction of neurite outgrowth should be predetermined.

A rate of single somata in cavities of 70 % was achieved for humane mDANs in this thesis. Single cell placement could potentially be achieved on a laboratory scale utilizing an upright patch clamp setup with glass pipettes of respective size and controllable liquid stream with the addition of a syringe pump. On a larger scale, this task could be efficiently performed in the future with inkjet-based cell printing technology.[322]

Control over the direction of neurite outgrowth could be gained by utilizing angular-dependent edge guidance, a principle already applied in 2D cultures (see Figure 2.6 c - d).[113, 121] The cavities can be adapted - for example to arrow-shapes - to tune the likelihood of neurites entering specific tunnels. Loops branching off the tunnels could hinder neurites to pass through in one direction while not affecting neurites approaching from the other direction.

Autapse could also be incorporated by circular tunnels to build short term analog memory storage by tuned synaptic feedback loops into the neuronal networks.[282]

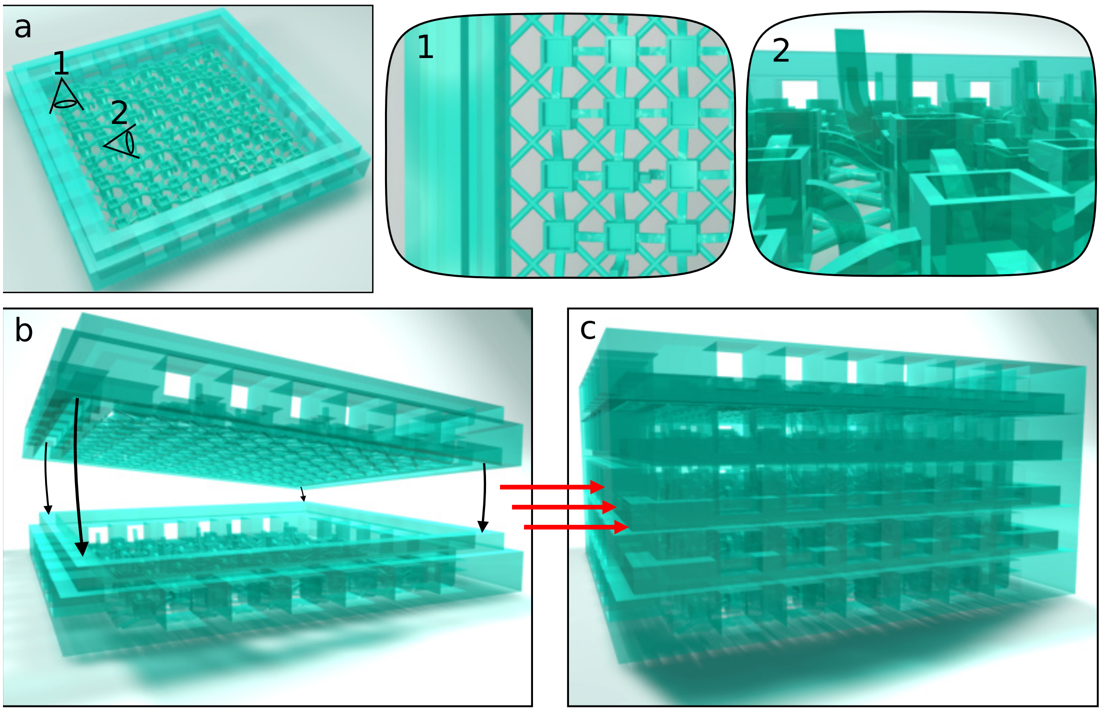

**Figure 7.3.:** Concept for stacked 3D structures. (a) A single unit of a stackable structure. The eye symbols indicate perspectives onto the unit displayed in (1) and (2). (b) Two units fit on top of each other. (c) The final structure consists of one base unit, an arbitrary number of middle units and a top unit.

### Stacked Structures for 3D complexity

High complexity in z-direction could be added with the principle of stacking. In this concept, a unit of towers is placed on a grid and connected to a border structure (Figure 7.3 a). The variety of pillar heights and tunnels within one unit is arbitrary. Some tunnels lead upwards and downwards and stop at the limits of the unit. Directly after cultivation, the units are stacked on top of each other (Figure 7.3 b - c). Afterwards, tunnels leading upwards are precisely connected to downwards tunnels from the unit above. Thus, complex neuronal networks can develop within the interconnected layers of the structure. Large openings in the resulting side walls ensure sufficient supply of nutrients to the cells through diffusion. Stacking with micro-tweezers controlled by a micromanipulator has already been applied to structures written with DLW (see Section 2.5.4).[133] In Section 5.2.3, sufficient stability of DLW-printed structures has been shown to be manipulated even by hand with reverse action tweezers.

### Interfacing Nanoelectronic Devices with Defined Neuronal Networks

A large research field is the combination of ordered neuronal networks with microelectromechanical systems to monitor network activity.[323, 324] Electrode arrays could be incorporated into the 3D structures for systematic read out of electrical signals from entire neuronal networks. Due to complete passivation with gap-less ALD coating, even cytotxic materials can theoretically be inserted for optimal readout.

One approach for the incorporation of electrodes could be in the utilization of electrochemical deposition: A multielectrode array serves as base for DLW by 2PP. The structures are written with the pillars directly on top of the electrodes. The key to obtain electrodes inside the cavities is to leave the center of the pillars unexposed in the DLW process which leads to tunnels in the center of the pillars. These tunnels extend from the electrode on the base carrier up to the bottom of the cavity. Subsequently, conducting material can be deposited selectively through electrochemical deposition, until the conducting material completely fills the tunnel and seals the bottom of the cavity. Since voltage can be applied to electrodes individually, it is possible to fine-tune the deposition time for each different pillar height in complex geometries. As a result of this approach, each pillar would have a cavity with a conducting bottom, which can be utilized to stimulate individual neurons and read out responses from the entire neuronal network simultaneously.

### Cell Culture Studies

The cell attachment rate and viability can be further optimized with systematic evaluation of different polymers and varying $Al_2O_3$ coating thickness with a special focus on substrate stiffness. The addition of extra glia cells to the cavities after maturation of neurons could be tested for increased network activity.[88] The viability and activity of cell cultures in the 3D structures can be studied under the influence of diverse environmental factors. Different adhesive substrate-bound cues as well as diffusible cues can be tested in the controlled environment of these substrates. With small modifications, the tunnels can be utilized as microfluidic or diffusion channels to study the effect of competing cues.[325] Utilizing humane neurons derived from iPSCs from affected patients in these devices could advance our understanding of neurodegenerative diseases.[326]

# Appendix: Cell Cultivation

A

## A.1. Cell Cultures

### A.1.1. Cell Adhesion Depending on Settle Time

The utilized protocol for culturing murine granular cells provides a recommended settling time of 60 min before the addition of further culture medium (Section 4.1). The actual influence of adhesion time on the cell density of MCGCs is determined with two controls each for seven different settling times between 1 min and 60 min. For each sample, cells are counted at four random spots of $275 \times 182\,\mu m^2$ after 4 DIV (see Table A.1). The cell count on substrates with adhesion times from 5 minutes to 45 minutes shows no significant difference. Cell attachment with one minute settling time is reduced by about -20 %. Cell count at 60 min is approx. 25 % up compared to the mean value for 5 minutes to 45 minutes. Thus, the recommended settling time of 60 min is met in all experiments.

**Table A.1.:** Cell count for different settle times for MCGCs at 4 DIV.

| Settle time | Sample 1 | Sample 2 | Joint Values |
|---|---|---|---|
| 1 min | 125 cells | 82 cells | 207 cells |
| 5 min | 143 cells | 136 cells | 279 cells |
| 10 min | 116 cells | 140 cells | 256 cells |
| 15 min | 140 cells | 129 cells | 269 cells |
| 30 min | 141 cells | 112 cells | 253 cells |
| 45 min | 145 cells | 119 cells | 264 cells |
| 60 min | 164 cells | 166 cells | 330 cells |

### A.1.2. Culture on $Al_2O_3$ vs ParC

$Al_2O_3$ and ParC were coated onto two glass cover slips each to evaluate the effect of surface coating on the viability of neuron cultures. Two cover slips were cultivated as control without additional coating besides PDL and laminin.

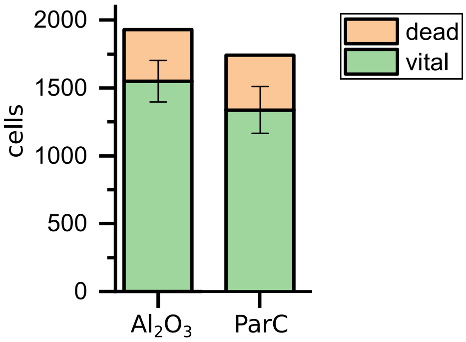

**Figure A.1.:** Viability of neurons on $Al_2O_3$ and ParC surfaces at 7 DIV. The counts for vital neurons plotted in green, the counts for dead neurons are plotted in red. All substrates were coated with PDL and laminin before culturing.

The substrates were analyzed in a CLSM live death assay at 7 DIV. Eight areas of $590 \times 590\,\mu m^2$ were imaged per substrate.

The results are plotted in Figure A.1. The highest viability and overall count of attached vital neurons is observed on $Al_2O_3$ coating with 80 % vital cells and a cell density of 278 cells/m$^2$. On ParC, 72 % of the observed cells are vital and the cell density is at 241 cells/m$^2$.

In Figure A.2, 3D scaffolds covered with (a) $Al_2O_3$ and (b) ParC are displayed. They are cultured with humane mDANs utilizing approach 1 (see Section 6.3). Because of low cell adhesion inside and high cell adhesion outside of the

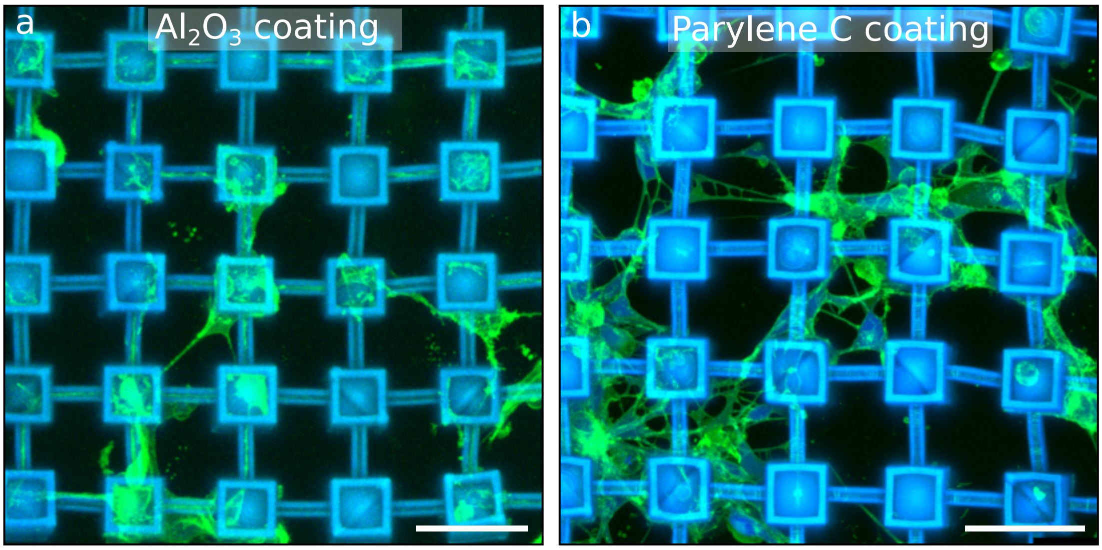

**Figure A.2.:** Humane mDANs cultivated with approach 1 on scaffolds that are coated with (a) $Al_2O_3$ and (b) ParC. Scale bars: 50 µm.

ParC coated scaffolds, $Al_2O_3$ coating was selected for further experiments with mDANs.

### A.1.3. Control cultures

Figure A.3 shows exemplary control cultures of MCGCs. Figure A.4 shows an exemplary growth cone of MCGCs close to the axon hillock that was fixated shortly after emerging from the soma.

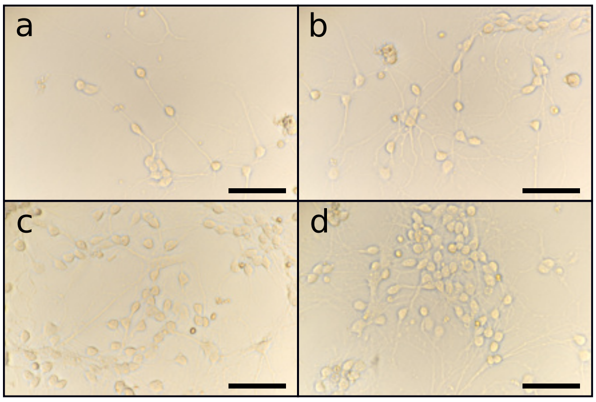

**Figure A.3.:** Optical images of MCGCs cultivated as control on the bottom of Petri dishes with approximated cell densities of (a) 400 cells/cm$^2$, (b) 800 cells/cm$^2$, (c) 2000 cells/cm$^2$ and (d) 2100 cell/cm$^2$. Scale bars: 50 µm.

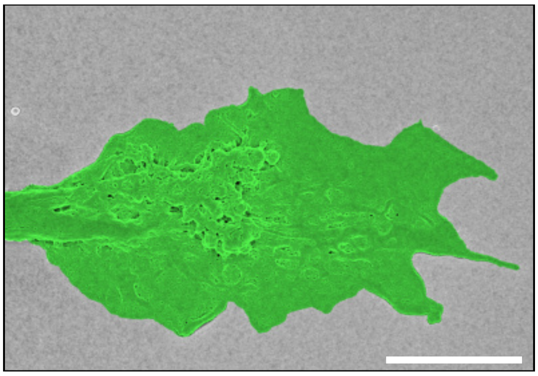

**Figure A.4.:** False colored SEM image of a growth cone from MCGCs at 1DIV. Scale bar: 4 µm.

### A.1.4. RIE Steps with PDL Pattern

In Figure A.5, PDL in a pattern of lines repeating every 300 µm is selectively printed perpendicular to steps onto substrates to limit the possible spreading direction of neurites of MCGCs. For 6 µm steps, neurites strongly align to the step edges on these surfaces and somata are mostly settled on lower steps or in the pits. Only in rare cases, neurites are expanded over top steps. Thus, multiple small networks of only a few neurons or neuron clusters arranged on lines oriented 90 ° to the steps have been build by the neurons. In between the lines is an area of approx. 150 µm without neurite attachment. On 9 µm steps, nearly all somata attached to the pits. Neurites of single cells are exclusively spread in an area of approx. 150 µm legth inside the pits. Neurites of cell clusters are also spread onto the upper steps. No neurites cross the top steps.

The reduction in size of the neuronal networks on 6 µm steps compared to complete coverage with PDL could indicate an unequal distribution of PDL along the printed lines. A possible explanation is that the droplets accumulate in the pits before the solvent evaporates, leaving the top edge without or with a low degree PDL coating. This hypothesis is consistent with the broad areas of approx. 150 µm where neurites extend parallel to the step edges despite dropplet diameters on flat surfaces of 30µm. Thus the top edge is not attractive to cross for neurites and this method is not suited to define pathways across step structures.

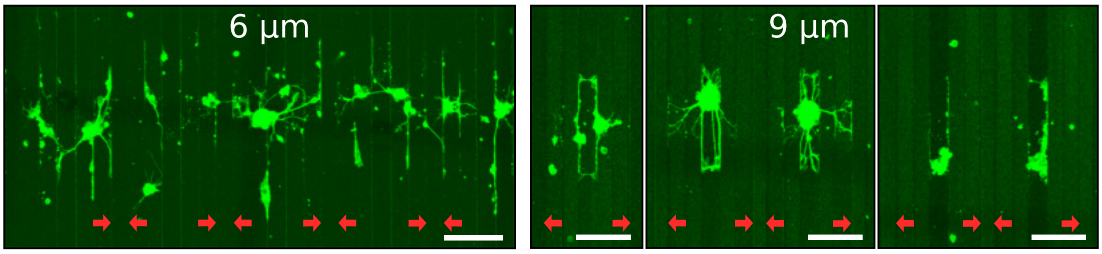

**Figure A.5.:** CLSM images of MCGCs at 10 - 11 DIV on steps produced by RIE. Steps of 6 µm and 9 µm height and 22 µm width, coated with ParC. PDL was selectively printed in lines perpendicular to the steps before culturing. Red arrows indicate top steps. Scale bars: 75 µm.

### A.1.5. Neuronal Activity of MCGCs

In Figure A.6 , exemplary recordings of membran potentials in current clamp of MCGCs in the 3D structures are plotted.

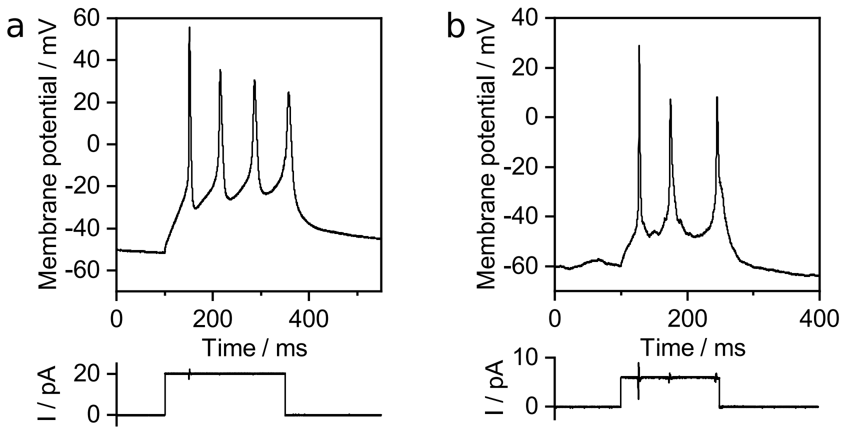

**Figure A.6.:** Exemplary current clamp recordings of MCGCs in the pillar scaffold at (a) 8 DIV with a current step of 20 pA and 250 ms duration and (b) 10 DIV with a current step of 6 pA and 150 ms.

## A.2. Cultivation of murine cerebellar granule cells

### A.2.1. Animals

C57BL/6J mice were bred at the animal facility of the University Medical Center Hamburg-Eppendorf and maintained at 22 °C on a 12 h light/12 h dark cycle and provided with food and water ad libitum. All experiments were conducted with mice of either sex, with and without green fluorescent protein (GFP) expression under the direction of the human ubiqutin C promoter (C57BL/6-Tg(UBC-GFP)30Scha/J) and in accordance with the German and European Community laws on protection of experimental animals. Procedures used were approved by the responsible committee of The State of Hamburg (permission number Org_679). Experiments were carried out and the manuscript was prepared following the ARRIVE guidelines for animal research.

### A.2.2. Media and solutions

All components for 100 ml X-1 cell culture medium are given in Table A.2. Protocols for the preparation of the components prior to mixing are given in Table A.3. The components were mixed and sterile filtered subsequently (Steriflip 0.22 µm, Millipore). Thus prepared solution was stored at 4 °Cfor a maximum of 2 weeks before use. B27 was added max. 7 d before use. At least for 1 h before use, the culture medium was transferred into 37 °Cand 5 % $CO_2$ environment for temperature- and pH-adjustment.

Additional to culture medium, stock solutions of Trypsin/DNAse I and DNase I were prepared prior to cell separation (Table A.4).

**Table A.2.:** Composition of culture medium for murine cerebellar granule cells.

| Component | Concentration | Volume | Target |
|---|---|---|---|
| Neurobasal A | 1 x | 90 ml | - |
| Pen/Strep | 100 x | 1 ml | 1 x |
| bovine serum albumin (BSA) | 10 % | 1 ml | 0.1 % |
| Insulin | 10 mg/ml | 100 µl | 10 µg/ml |
| L-Thyroxine | 4 µM | 100 µl | 4 nM |
| Transferrin, holo | 50 mg/ml | 200 µl | 100 µg/ml |
| Na-Selenite | 30 µM | 100 µl | 30 nM |
| Fetal bovine serum | - | 6 ml | 6 % |
| B27 supplement | - | 2 ml | 50 x |

## A.3. Cultivation of small molecule neural precursor cells

A variety of solutions is needed to cultivate and differentiate smNPCs. In the tables below are listed: The components for growth factor stock solution (Table A.5), N2/B27 solution (Table A.6), basic smNPC medium (Table A.7), freeze medium (Table A.8), split medium (Table A.9), patterning medium (Table A.10) and maturation medium (Table A.11).

Table A.3.: Preparation protocols for culture medium ingredients.

| Component | Protocol |
|---|---|
| Pen/Strep | Store 1 ml aliquotes at - 20 °C. |
| BSA | Prepare 10 % stock solution in aqua bidest. Store 1 ml aliquots at -20 °C. |
| Insulin | Dissolve 20 mg in 2 ml 10 mM ice cold HCl. In case of hazy solution, add small amounts of acid. Store 100 µl aliquots at -20 °C. |
| L-Thyroxine | Dissolve 3.1 mg L-thyroxine in 900 µl EtOH. Add 1 N NaOH untill the solution gets clear. Fill up with EtOH to 1 ml [4 mM stock]. Take 10 µl from the 4 mM stock and add 9.99 HBSS [4 µM stock]. Store 100 µl aliquots at -20 °C. |
| Transferrin, holo | Dissolve 50 mg in 1 ml Neurobasal A (1 x). Store 200 µl aliquotes at -20 °C. |
| Na-Selenite | Dissolve 5.19 mg Na-Selenite in 10 ml Neurobasal A (1 x) [3mM stock]. Take 100 µl of this stock solution and dissolve in 9.9 ml Neurobasal A [30 µM stock]. Store at -20 °C. |

Table A.4.: Preparation protocols for Trypsin/DNAse I- and DNAse I-solution

| Component | Protocol |
|---|---|
| Trypsin/DNAse I | Mix 0.2 g Trypsin, 20 mg DNAse I and 200 µl MgCL (80 mM). Add 18 ml HBSS, adjust pH with NaOH to 7.8 and fill up to 20 ml with HBSS. Filter sterile and store in 0.66 ml aliquots at -20 °C. |
| DNAse I | Mix 10 mg DNase I, 50 mg glucose and 20 ml Neurobasal A (1 x). Filter sterile and store in 0.66 ml aliquots at -20 °C. |

**Table A.5.:** Growth factor stock solution.

| **Component** | **Concentration** | **Solvent** |
|---|---|---|
| CHIR | 6 mM | dimethyl sulfoxide (DMSO) |
| Ascorbic acid | 200 mM | $H_2O$ |
| SAG | 10 mM | DMSO |
| GDNF | 10 µg/ml | PBS with 0.1 % BSA |
| BDNF | 20 µg/ml | PBS with 0.1 % BSA |
| TGF-SS3 | 2 µg/ml | PBS with 0.1 % BSA |
| dbcAMP | 50 mM | DMEM/F12 |

**Table A.6.:** N2/B27 solution.

| **Component** | **Concentration** |
|---|---|
| DMEM/F12 | 50 % |
| Neurobasal | 50 % |
| Penecillin-Streptomycin-Glutamine (PS/G 100x) | 1:100 |
| B27 (without Vitamin A) supplement | 1:100 |
| N2 supplement | 1:200 |

**Table A.7.:** Basic smNPC medium.

| **Component** | **Concentration** |
|---|---|
| N2/B27 | 100 % |
| CHIR | 3 µM |
| Ascorbic acid | 100 µM |
| SAG | 0.5 µM |

**Table A.8.:** Freeze medium.

| **Component** | **Concentration** |
|---|---|
| N2/B27 | 90 % |
| DMSO | 10 % |

**Table A.9.:** Split medium.

| Component | Concentration |
|---|---|
| DMEM (high glucose 1:250) | 92.5 % |
| BSA | 7.5 % |

**Table A.10.:** Patterning medium.

| Component | Concentration |
|---|---|
| N2/B27 | 100 % |
| GDNF | 1 ng/ml |
| BDNF | 1 ng/ml |
| Ascorbic acid | 100 µM |
| SAG | 0.5 µM |

**Table A.11.:** Maturation medium.

| Component | Concentration |
|---|---|
| N2/B27 | 100 % |
| GDNF | 2 ng/ml |
| BDNF | 2 ng/ml |
| Ascorbic acid | 100 µM |
| TGF-SS3 | 1 ng/ml |
| dbcAMP | 100 µM |

# B

# Appendix: 2PP Produced Structures

### 3D Scaffolds in optical microscopy

Figure B.1 displays two optical microscopy images of cultivated 3D scaffolds - one of them written into a box and the other written directly onto a glass carrier - taken with the microscope of the patch clamp setup (see Section 4.4). Visibility of cells is significantly improved in scaffolds on glass carriers compared to scaffolds in IPDip boxes.

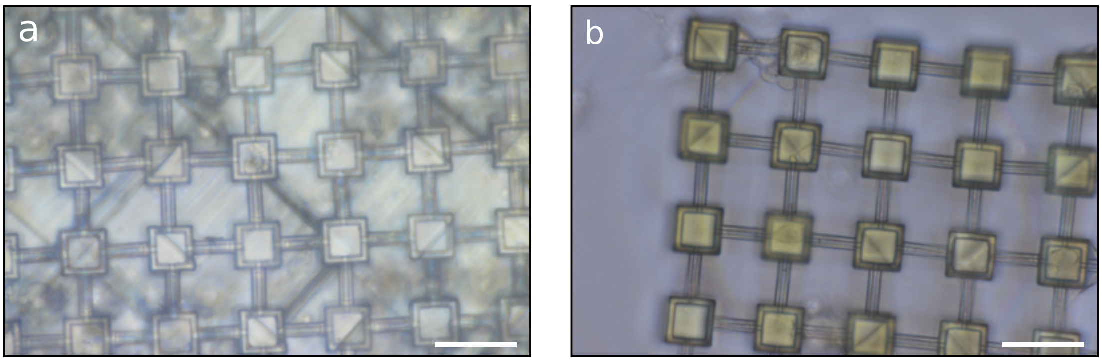

**Figure B.1.:** Optical microscopy images of the Structure (a) in a box and (b) directly on a glass carrier. Skale bars: 40 µm.

### Limits in tunnel size

The minimum width and height of tunnels with DLW by 2PP in IPDip is limited by scattering effects that lead to partial clogging beneath a certain dimension. Free horizontal tunnels were reliably achieved during this work with about 2 ţm minimum height. In future experiments and applications, smaller tunnel width might be required.

One approach to obtain smaller tunnels could be the utilization of a DLW setup with STED technology (Section 3.4.4). However, at the current state, STED integration into a DLW setup is expensive and the processing of 2PP with STED is much to slow to be feasible for the production of cell culture platforms with tunnels such as the ones presented in this thesis.

Another approach, that is readily available, is the design of scaffolds, where the tunnels are written in vertical direction. This way, the shape of the tunnel

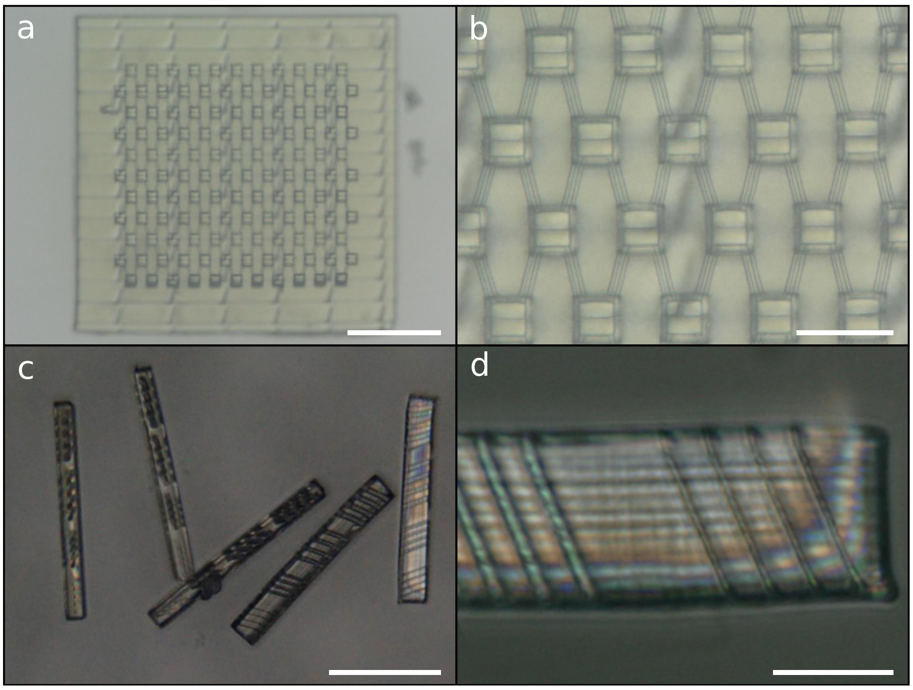

**Figure B.2.:** Optical images of tunnels written in 70 ° angle. Skale bars: 200 µm, 50 µm, 30 µm, 12 µm.

is mainly determined by the shape of the voxel in xy-diection, whereas for horizontal tunnels the larger voxel in z-direction has a larger impact on the resolution limit (Section 3.4). An exemplary structure with tunnels written in a vertical angle of 70 ° is shown in Figure B.2 a - b. The construct, consisting of a pillar structure attached to a box, is designed with a rotation of 90 °, so that the pillar structure is on one side of the box. The construct is tipped over after development with tweezers, so that the towers and tunnels are on the top of the box. The tunnels have a width of approx. 1 ţm. In further tests, tunnels with widths down to 0.5 µm were achieved (Figure B.2 c - d).

# Bibliography

[1] A. P. Alivisatos, M. Chun, G. M. Church, R. J. Greenspan, M. L. Roukes, and R. Yuste. *The Brain Activity Map Project and the Challenge of Functional Connectomics*. Neuron **74**, 970–974 (2012). Cited on page(s): 1.

[2] R. Yuste and C. Bargmann. *Toward a Global BRAIN Initiative*. Cell **168**, 956–959 (2017). Cited on page(s): 1.

[3] A. M. Dale, A. K. Liu, B. R. Fischl, R. L. Buckner, J. W. Belliveau, J. D. Lewine, and E. Halgren. *Dynamic Statistical Parametric Mapping*. Neuron **26**, 55–67 (2000). Cited on page(s): 1.

[4] D. D. Cox and R. L. Savoy. *Functional magnetic resonance imaging (fMRI) brain reading: detecting and classifying distributed patterns of fMRI activity in human visual cortex*. NeuroImage **19**, 261–270 (2003). Cited on page(s): 1.

[5] S. A. Rombouts, F. Barkhof, R. Goekoop, C. J. Stam, and P. Scheltens. *Altered resting state networks in mild cognitive impairment and mild Alzheimer's disease: An fMRI study*. Human Brain Mapping **26**, 231–239 (2005). Cited on page(s): 1.

[6] T. Tsuji. *Organ Regeneration Based on Developmental Biology*. Springer Singapore (2017). ISBN: 978-981-10-3766-5, URL: `http://link.springer.com/10.1007/978-981-10-3768-9`. Cited on page(s): 1.

[7] F. A. Azevedo, L. R. Carvalho, L. T. Grinberg, J. M. Farfel, R. E. Ferretti, R. E. Leite, W. J. Filho, R. Lent, and S. Herculano-Houzel. *Equal numbers of neuronal and nonneuronal cells make the human brain an isometrically scaled-up primate brain*. The Journal of Comparative Neurology **513**, 532–541 (2009). Cited on page(s): 1, 5.

[8] C. S. von Bartheld, J. Bahney, and S. Herculano-Houzel. *The search for true numbers of neurons and glial cells in the human brain: A review of 150 years of cell counting*. Journal of Comparative Neurology **524**, 3865–3895 (2016). Cited on page(s): 1.

[9] C. G. Galizia and P.-m. Lledo. *Neurosciences - From Molecule to Behavior: a university textbook*. Springer Spektrum (2013). ISBN: 9783642107689, URL: `https://link.springer.com/book/10.1007/978-3-642-10769-6`. Cited on page(s): 1.

[10] S. Herculano-Houzel. *The human brain in numbers: a linearly scaled-up primate brain*. Frontiers in Human Neuroscience **3**, 1–11 (2009). Cited on page(s): 1.

[11] E. R. Kandel, Y. Dudai, and M. R. Mayford. *The Molecular and Systems Biology of Memory*. Cell **157**, 163–186 (2014). Cited on page(s): 1, 6.

[12] D. Kilinc, A. Blasiak, and G. U. Lee. *Microtechnologies for studying the role of mechanics in axon growth and guidance*. Frontiers in Cellular Neuroscience **9**, 1–8 (2015). Cited on page(s): 2.

[13] K. Franze, P. A. Janmey, and J. Guck. *Mechanics in Neuronal Development and Repair*. Annual Review of Biomedical Engineering **15**, 227–251 (2013). Cited on page(s): 2.

[14] D. Hoffman-Kim, J. A. Mitchel, and R. V. Bellamkonda. *Topography, Cell Response, and Nerve Regeneration*. Annual Review of Biomedical Engineering **12**, 203–231 (2010). Cited on page(s): 2.

[15] S. Pautot, C. Wyart, and E. Y. Isacoff. *Colloid-guided assembly of oriented 3D neuronal networks*. Nature Methods **5**, 735–740 (2008). Cited on page(s): 2, 20.

[16] N. Anscombe. *Direct laser writing*. Nature Photonics **4**, 22–23 (2010). Cited on page(s): 2.

[17] S. Turunen, E. Käpylä, M. Lähteenmäki, L. Ylä-Outinen, S. Narkilahti, and M. Kellomäki. *Direct laser writing of microstructures for the growth guidance of human pluripotent stem cell derived neuronal cells*. Optics and Lasers in Engineering **55**, 197–204 (2014). Cited on page(s): 3.

[18] C. S. Bausch, A. Koitmäe, E. Stava, A. Price, P. J. Resto, Y. Huang, D. Sonnenberg, Y. Stark, C. Heyn, J. C. Williams, E. W. Dent, and R. H. Blick. *Guided neuronal growth on arrays of biofunctionalized GaAs/InGaAs semiconductor microtubes*. Applied Physics Letters **103**, 1–10 (2013). Cited on page(s): 3, 18, 70.

[19] C. Fendler, C. Denker, J. Harberts, P. Bayat, R. Zierold, G. Loers, M. Münzenberg, and R. H. Blick. *Microscaffolds by Direct Laser Writing for Neurite Guidance Leading to TailorMade Neuronal Networks*. Advanced Biosystems **3**, 1800329 (2019). Cited on page(s): 4.

[20] D. L. Sherman and P. J. Brophy. *Mechanisms of axon ensheathment and myelin growth*. Nature Reviews Neuroscience **6**, 683–690 (2005). Cited on page(s): 5.

[21] K. Susuki and M. N. Rasband. *Molecular mechanisms of node of Ranvier formation*. Current Opinion in Cell Biology **20**, 616–623 (2008). Cited on page(s): 5.

[22] A. F. Huxley and R. Stämpeli. *Evidence for saltatory conduction in peripheral myelinated nerve fibres*. The Journal of Physiology **108**, 315–339 (1949). Cited on page(s): 5.

[23] R. Stämpfli. *Saltatory Conduction in Nerve*. Physiological Reviews **34**, 101–112 (1954). Cited on page(s): 5.

[24] D. Purves, G. J. Augustine, D. Fitzpatrick, L. C. Katz, A.-S. LaMantia, J. O. McNamara, and S. M. Williams. *Increased Conduction Velocity as a Result of Myelination, Neuroscience*, **2nd edition**, Sinauer Associates (2001). ISBN: 0-87893-742-0, URL: `https://www.ncbi.nlm.nih.gov/books/NBK10921/`. Cited on page(s): 5.

[25] B. R. Karamched and P. C. Bressloff. *Delayed feedback model of axonal length sensing*. Biophysical Journal **108**, 2408–2419 (2015). Cited on page(s): 5.

[26] F. Folz, L. Wettmann, G. Morigi, and K. Kruse. *Sound of an axon's growth*. Physical Review E **99**, 050401 (2019). Cited on page(s): 5.

[27] T. E. of Encyclopaedia Britannica. *Sciatic nerve*. URL: `https://www.britannica.com/science/sciatic-nerve` (accessed on 28.10.2019). Cited on page(s): 5.

[28] J. Hawkins and S. Ahmad. *Why Neurons Have Thousands of Synapses, a Theory of Sequence Memory in Neocortex*. Frontiers in Neural Circuits **10**, 23 (2016). Cited on page(s): 6, 12.

[29] D. A. Wollner and W. A. Catterall. *Localization of sodium channels in axon hillocks and initial segments of retinal ganglion cells*. Proceedings of the National Academy of Sciences **83**, 8424–8428 (1986). Cited on page(s): 6.

[30] D. Zhou, S. Lambert, P. L. Malen, S. Carpenter, L. M. Boland, and V. Bennett. *Ankyrin G Is Required for Clustering of Voltage-gated Na Channels at Axon Initial Segments and for Normal Action Potential Firing*. The Journal of Cell Biology **143**, 1295–1304 (1998). Cited on page(s): 6.

[31] G. Major, M. E. Larkum, and J. Schiller. *Active Properties of Neocortical Pyramidal Neuron Dendrites*. Annual Review of Neuroscience **36**, 1–24 (2013). Cited on page(s): 6.

[32] J. Konorski. *Conditioned reflexes and neuron organization*. CUP Archive (1948). , . Cited on page(s): 6.

[33] B. Casey, J. D. Cohen, P. Jezzard, R. Turner, D. C. Noll, R. J. Trainor, J. Giedd, D. Kaysen, L. Hertz-Pannier, and J. L. Rapoport. *Activation of Prefrontal Cortex in Children during a Nonspatial Working Memory Task with Functional MRI*. NeuroImage **2**, 221–229 (1995). Cited on page(s): 6.

[34] S. Marinesco and T. J. Carew. *Serotonin Release Evoked by Tail Nerve Stimulation in the CNS of Aplysia : Characterization and Relationship to Heterosynaptic Plasticity*. The Journal of Neuroscience **22**, 2299–2312 (2002). Cited on page(s): 6.

[35] L. Chiu and A. J. Roskams. *A companion publication to BrainFacts. org and a primer on the brain and nervous system*. Society for Neuroscience, www. BrainFacts. org , (2012). Cited on page(s): 6.

[36] K. M. Yamada, B. S. Spooner, and N. K. Wessells. *AXON GROWTH: ROLES OF MICROFILAMENTS AND MICROTUBULES*. Proceedings of the National Academy of Sciences **66**, 1206–1212 (1970). Cited on page(s): 7.

[37] M. Tessier-Lavigne and C. S. Goodman. *The molecular biology of axon guidance*. Science (New York, N.Y.) **274**, 1123–33 (1996). Cited on page(s): 7.

[38] P. Froeter, Y. Huang, O. V. Cangellaris, W. Huang, E. W. Dent, M. U. Gillette, J. C. Williams, and X. Li. *Toward Intelligent Synthetic Neural Circuits: Directing and Accelerating Neuron Cell Growth by Self-Rolled-Up Silicon Nitride Microtube Array*. ACS Nano **8**, 11108–11117 (2014). Cited on page(s): 7, 18, 79.

[39] L. Erskine and E. Herrera. *The retinal ganglion cell axon's journey: Insights into molecular mechanisms of axon guidance*. Developmental Biology **308**, 1–14 (2007). Cited on page(s): 7.

[40] E. W. Dent and F. B. Gertler. *Cytoskeletal Dynamics and Transport in Growth Cone Motility and Axon Guidance*. Neuron **40**, 209–227 (2003). Cited on page(s): 7, 9.

[41] L. A. Lowery and D. V. Vactor. *The trip of the tip: understanding the growth cone machinery*. Nature Reviews Molecular Cell Biology **10**, 332–343 (2009). Cited on page(s): 7–9.

[42] Y. Xiong, A. C. Lee, D. M. Suter, and G. U. Lee. *Topography and Nanomechanics of Live Neuronal Growth Cones Analyzed by Atomic Force Microscopy*. Biophysical Journal **96**, 5060–5072 (2009). Cited on page(s): 7.

[43] P. F. Maness and M. Schachner. *Neural recognition molecules of the immunoglobulin superfamily: signaling transducers of axon guidance and neuronal migration*. Nature Neuroscience **10**, 19–26 (2007). Cited on page(s): 7.

[44] A. R. Evans, S. Euteneuer, E. Chavez, L. M. Mullen, E. E. Hui, S. N. Bhatia, and A. F. Ryan. *Laminin and fibronectin modulate inner ear spiral ganglion neurite outgrowth in anin vitro alternate choice assay*. Developmental Neurobiology **67**, 1721–1730 (2007). Cited on page(s): 7, 80.

[45] B. J. Dickson. *Molecular Mechanisms of Axon Guidance*. Science **298**, 1959–1964 (2002). Cited on page(s): 7.

[46] I. Brunet, C. Weinl, M. Piper, A. Trembleau, M. Volovitch, W. Harris, A. Prochiantz, and C. Holt. *The transcription factor Engrailed-2 guides retinal axons*. Nature **438**, 94–98 (2005). Cited on page(s): 7.

[47] J. K. Chilton. *Molecular mechanisms of axon guidance*. Developmental Biology **292**, 13–24 (2006). Cited on page(s): 7, 17.

[48] Y. Zou and A. I. Lyuksyutova. *Morphogens as conserved axon guidance cues*. Current Opinion in Neurobiology **17**, 22–28 (2007). Cited on page(s): 7.

[49] S. J. Butler and G. Tear. *Getting axons onto the right path: The role of transcription factors in axon guidance*. Development **134**, 439–448 (2007). Cited on page(s): 7.

[50] S. D. Sanford, J. C. Gatlin, T. Hkfelt, and K. H. Pfenninger. *Growth cone responses to growth and chemotropic factors*. European Journal of Neuroscience **28**, 268–278 (2008). Cited on page(s): 7.

[51] E. T. Stoeckli. *Understanding axon guidance: are we nearly there yet?*. Development **145**, dev151415 (2018). Cited on page(s): 8.

[52] K. Kalil and E. W. Dent. *Touch and go: guidance cues signal to the growth cone cytoskeleton*. Current Opinion in Neurobiology **15**, 521–526 (2005). Cited on page(s): 8.

[53] G. J. Bashaw and R. Klein. *Signaling from Axon Guidance Receptors*. Cold Spring Harbor Perspectives in Biology **2**, a001941–a001941 (2010). Cited on page(s): 8.

[54] T. Tojima, H. Akiyama, R. Itofusa, Y. Li, H. Katayama, A. Miyawaki, and H. Kamiguchi. *Attractive axon guidance involves asymmetric membrane transport and exocytosis in the growth cone*. Nature Neuroscience **10**, 58–66 (2007). Cited on page(s): 8.

[55] D. Bonanomi, E. F. Fornasiero, G. Valdez, S. Halegoua, F. Benfenati, A. Menegon, and F. Valtorta. *Identification of a developmentally regulated pathway of membrane retrieval in neuronal growth cones*. Journal of Cell Science **121**, 3757–3769 (2008). Cited on page(s): 8.

[56] N. Gomez, S. Chen, and C. E. Schmidt. *Polarization of hippocampal neurons with competitive surface stimuli: contact guidance cues are preferred over chemical ligands*. Journal of The Royal Society Interface **4**, 223–233 (2007). Cited on page(s): 8, 19.

[57] D. Mortimer, T. Fothergill, Z. Pujic, L. J. Richards, and G. J. Goodhill. *Growth cone chemotaxis*. Trends in Neurosciences **31**, 90–98 (2008). Cited on page(s): 9.

[58] M. Yoshihara, M. B. Rheuben, and Y. Kidokoro. *Transition from Growth Cone to Functional Motor Nerve Terminal in Drosophila Embryos*. The Journal of Neuroscience **17**, 8408–8426 (1997). Cited on page(s): 9.

[59] R. C. Thomas. *Electrogenic sodium pump in nerve and muscle cells*. Physiological Reviews **52**, 563–594 (1972). Cited on page(s): 11.

[60] O. Pongs. *Voltage-gated potassium channels*. Biomembranes: A Multi-Volume Treatise **6**, 199–220 (1997). Cited on page(s): 11.

[61] W. Stuehmer. *Sodium Channels, Encyclopedia of Life Sciences*, 65–71, John Wiley & Sons, Ltd (2001). ISBN: 9780080450469, URL: `http://doi.wiley.com/10.1038/npg.els.0000127`. Cited on page(s): 11.

[62] C. Egri and P. C. Ruben. *Action Potentials: Generation and Propagation*. eLS , (2012). Cited on page(s): 11, 12.

[63] F. Bezanilla. *How membrane proteins sense voltage*. Nature Reviews Molecular Cell Biology **9**, 323–332 (2008). Cited on page(s): 11.

[64] R. H. Adrian, W. K. Chandler, and A. L. Hodgkin. *Slow changes in potassium permeability in skeletal muscle*. The Journal of Physiology **208**, 645–668 (1970). Cited on page(s): 11.

[65] A. E. Pereda. *Electrical synapses and their functional interactions with chemical synapses*. Nature Reviews Neuroscience **15**, 250–263 (2014). Cited on page(s): 12.

[66] B. Zuber, I. Nikonenko, P. Klauser, D. Muller, and J. Dubochet. *The mammalian central nervous synaptic cleft contains a high density of periodically organized complexes*. Proceedings of the National Academy of Sciences **102**, 19192–19197 (2005). Cited on page(s): 12.

[67] E. Neher and T. Sakaba. *Multiple Roles of Calcium Ions in the Regulation of Neurotransmitter Release*. Neuron **59**, 861–872 (2008). Cited on page(s): 12, 13.

[68] D. Purves, G. J. Augustine, D. Fitzpatrick, L. C. Katz, A.-S. LaMantia, J. O. McNamara, and S. M. Williams. *Electrical Synapses*, , **2nd edition**, Sinauer Associates (2001). ISBN: 0-87893-742-0, URL: `https://www.ncbi.nlm.nih.gov/books/NBK11164/`. Cited on page(s): 13, 14.

[69] A. K. McAllister, L. C. Katz, and D. C. Lo. *NEUROTROPHINS AND SYNAPTIC PLASTICITY*. Annual Review of Neuroscience **22**, 295–318 (1999). Cited on page(s): 13.

[70] G. G. Turrigiano. *The Self-Tuning Neuron: Synaptic Scaling of Excitatory Synapses*. Cell **135**, 422–435 (2008). Cited on page(s): 13.

[71] A. G. Carter, G. J. Soler-Llavina, and B. L. Sabatini. *Timing and Location of Synaptic Inputs Determine Modes of Subthreshold Integration in Striatal Medium Spiny Neurons*. Journal of Neuroscience **27**, 8967–8977 (2007). Cited on page(s): 14.

[72] N. Hiratani and T. Fukai. *Redundancy in synaptic connections enables neurons to learn optimally*. Proceedings of the National Academy of Sciences **115**, E6871–E6879 (2018). Cited on page(s): 14.

[73] B. W. Connors and M. A. Long. *ELECTRICAL SYNAPSES IN THE MAMMALIAN BRAIN*. Annual Review of Neuroscience **27**, 393–418 (2004). Cited on page(s): 14.

[74] S. G. Hormuzdi, M. A. Filippov, G. Mitropoulou, H. Monyer, and R. Bruzzone. *Electrical synapses: a dynamic signaling system that shapes the activity of neuronal networks*. Biochimica et Biophysica Acta (BBA) - Biomembranes **1662**, 113–137 (2004). Cited on page(s): 14.

[75] L. J. Millet and M. U. Gillette. *Over a century of neuron culture: from the hanging drop to microfluidic devices*. The Yale journal of biology and medicine **85**, 501–21 (2012). Cited on page(s): 14, 15.

[76] R. G. Harrison. *The outgrowth of the nerve fiber as a mode of protoplasmic movement*. Journal of Experimental Zoology **9**, 787–846 (1910). Cited on page(s): 14, 15.

[77] A. CARREL. *CULTIVATION OF ADULT TISSUES AND ORGANS OUTSIDE OF THE BODY*. JAMA: The Journal of the American Medical Association **55**, 1379 (1910). Cited on page(s): 15.

[78] S. Roth, S. Zhang, J. Chiu, E. K. Wirth, and U. Schweizer. *Development of a serum-free supplement for primary neuron culture reveals the interplay of selenium and vitamin E in neuronal survival*. Journal of Trace Elements in Medicine and Biology **24**, 130–137 (2010). Cited on page(s): 15.

[79] A. Carrel. *A METHOD FOR THE PHYSIOLOGICAL STUDY OF TISSUES IN VITRO*. Journal of Experimental Medicine **38**, 407–418 (1923). Cited on page(s): 15.

[80] G. O. Gey. *An improved technic for massive tissue culture*. The American Journal of Cancer **17**, 752–756 (1933). Cited on page(s): 15.

[81] M. J. Hogue. *Human fetal ependymal cells in tissue cultures*. The Anatomical Record **99**, 523–529 (1947). Cited on page(s): 15.

[82] G. Rose. *A separable and multipurpose tissue culture chamber*. Texas reports on biology and medicine **12**, 1074–83 (1954). Cited on page(s): 15.

[83] E. J. Furshpan, P. R. MacLeish, P. H. O'Lague, and D. D. Potter. *Chemical transmission between rat sympathetic neurons and cardiac myocytes developing in microcultures: evidence for cholinergic, adrenergic, and dual-function neurons*. Proceedings of the National Academy of Sciences **73**, 4225–4229 (1976). Cited on page(s): 15.

[84] C. Yamamoto. *Activation of hippocampal neurons by mossy fiber stimulation in thin brain sections in vitro*. Experimental Brain Research **14**, 423–435 (1972). Cited on page(s): 15.

[85] R. B. Campenot. *Local control of neurite development by nerve growth factor*. Proceedings of the National Academy of Sciences **74**, 4516–4519 (1977). Cited on page(s): 15.

[86] J. Gordon, S. Amini, and M. K. White. *General Overview of Neuronal Cell Culture*, , **1078**1–8, Humana Press (2013). ISBN: 978-1-62703-639-9, URL: `http://link.springer.com/10.1007/978-1-62703-640-5%7B%5C_%7D1`. Cited on page(s): 16.

[87] L. M. Yu, N. D. Leipzig, and M. S. Shoichet. *Promoting neuron adhesion and growth*. Materials Today **11**, 36–43 (2008). Cited on page(s): 16.

[88] B. Wheeler and G. Brewer. *Designing Neural Networks in Culture*. Proceedings of the IEEE **98**, 398–406 (2010). Cited on page(s): 16, 110.

[89] L. W. Lau, R. Cua, M. B. Keough, S. Haylock-Jacobs, and V. W. Yong. *Pathophysiology of the brain extracellular matrix: a new target for remyelination*. Nature Reviews Neuroscience **14**, 722–729 (2013). Cited on page(s): 16.

[90] D. Edgar, R. Timpl, and H. Thoenen. *The heparin-binding domain of laminin is responsible for its effects on neurite outgrowth and neuronal survival*. The EMBO Journal **3**, 1463–1468 (1984). Cited on page(s): 16, 72.

[91] R. W. Gundersen. *Response of sensory neurites and growth cones to patterned substrata of laminin and fibronectin in vitro*. Developmental Biology **121**, 423–431 (1987). Cited on page(s): 16.

[92] D. Mazia. *Adhesion of cells to surfaces coated with polylysine. Applications to electron microscopy*. The Journal of Cell Biology **66**, 198–200 (1975). Cited on page(s): 16.

[93] T. Takahashi, F. Nakamura, Z. Jin, R. G. Kalb, and S. M. Strittmatter. *Semaphorins A and E act as antagonists of neuropilin-1 and agonists of neuropilin-2 receptors*. Nature Neuroscience **1**, 487–493 (1998). Cited on page(s): 16.

[94] I. Dupin, L. Lokmane, M. Dahan, S. Garel, and V. Studer. *Subrepellent doses of Slit1 promote Netrin-1 chemotactic responses in subsets of axons*. Neural Development **10**, 1–10 (2015). Cited on page(s): 16, 17.

[95] S. Varon and C. Raiborn. *Dissociation, fractionation, and culture of embryonic brain cells*. Brain Research **12**, 180–199 (1969). Cited on page(s): 17.

[96] M. Sensenbrenner, J. Booher, and P. Mandel. *Cultivation and growth of dissociated neurons from chick embryo cerebral cortex in the presence of different substrates*. Zeitschrift fuer Zellforschung und Mikroskopische Anatomie **117**, 559–569 (1971). Cited on page(s): 17.

[97] E. Yavin. *ATTACHMENT AND CULTURE OF DISSOCIATED CELLS FROM RAT EMBRYO CEREBRAL HEMISPHERES ON POLYLYSINE-COATED SURFACE*. The Journal of Cell Biology **62**, 540–546 (1974). Cited on page(s): 17, 70.

[98] D. Londono, W. F. Kuhs, and J. L. Finney. *Enclathration of helium in ice II: the first helium hydrate*. Nature **332**, 141–142 (1988). Cited on page(s): 17.

[99] D. Kleinfeld, K. Kahler, and P. Hockberger. *Controlled outgrowth of dissociated neurons on patterned substrates*. The Journal of Neuroscience **8**, 4098–4120 (1988). Cited on page(s): 17, 18, 70.

[100] A. A. Oliva, C. D. James, C. E. Kingman, H. G. Craighead, and G. A. Banker. *Patterning axonal guidance molecules using a novel strategy for microcontact printing*. Neurochemical research **28**, 1639–48 (2003). Cited on page(s): 17, 18, 66.

[101] M. Kwiat, R. Elnathan, A. Pevzner, A. Peretz, B. Barak, H. Peretz, T. Ducobni, D. Stein, L. Mittelman, U. Ashery, and F. Patolsky. *Highly Ordered Large-Scale Neuronal Networks of Individual Cells  Toward Single Cell to 3D Nanowire Intracellular Interfaces*. ACS Applied Materials & Interfaces **4**, 3542–3549 (2012). Cited on page(s): 17, 18, 66.

[102] C. Miller, S. Jeftinija, and S. Mallapragada. *Synergistic Effects of Physical and Chemical Guidance Cues on Neurite Alignment and Outgrowth on Biodegradable Polymer Substrates*. Tissue Engineering **8**, 367–378 (2002). Cited on page(s): 18.

[103] Y. Fan, F. Cui, S. Hou, Q. Xu, L. Chen, and I.-S. Lee. *Culture of neural cells on silicon wafers with nano-scale surface topograph*. Journal of Neuroscience Methods **120**, 17–23 (2002). Cited on page(s): 18.

[104] A. Marino, G. Ciofani, C. Filippeschi, M. Pellegrino, M. Pellegrini, P. Orsini, M. Pasqualetti, V. Mattoli, and B. Mazzolai. *Two-Photon Polymerization of Sub-micrometric Patterned Surfaces: Investigation of Cell-Substrate Interactions and Improved Differentiation of Neuron-like Cells*. ACS Applied Materials & Interfaces **5**, 13012–13021 (2013). Cited on page(s): 18, 61.

[105] B. Kaehr, R. Allen, D. J. Javier, J. Currie, and J. B. Shear. *Guiding neuronal development with in situ microfabrication*. Proceedings of the National Academy of Sciences **101**, 16104–16108 (2004). Cited on page(s): 18.

[106] J. S. Goldner, J. M. Bruder, G. Li, D. Gazzola, and D. Hoffman-Kim. *Neurite bridging across micropatterned grooves*. Biomaterials **27**, 460–472 (2006). Cited on page(s): 18.

[109] H. Francisco, B. B. Yellen, D. S. Halverson, G. Friedman, and G. Gallo. *Regulation of axon guidance and extension by three-dimensional constraints*. Biomaterials **28**, 3398–3407 (2007). Cited on page(s): 18, 61.

[110] A. Tooker, E. Meng, J. Erickson, Y.-C. Tai, and J. Pine*Development of biocompatible parylene neurocages*IEEE (2004).

[111] B. W. Tuft, L. Xu, S. P. White, A. E. Seline, A. M. Erwood, M. R. Hansen, and C. A. Guymon. *Neural Pathfinding on Uni- and Multidirectional Photopolymerized Micropatterns*. ACS Applied Materials & Interfaces **6**, 11265–11276 (2014). Cited on page(s): 18, 19, 81.

[112] W. Li, Q. Y. Tang, A. D. Jadhav, A. Narang, W. X. Qian, P. Shi, and S. W. Pang. *Large-scale topographical screen for investigation of physical neural-guidance cues*. Scientific Reports **5**, 1–8 (2015). Cited on page(s): 18, 81.

[113] R. Renault, J.-B. Durand, J.-L. Viovy, and C. Villard. *Asymmetric axonal edge guidance: a new paradigm for building oriented neuronal networks*. Lab on a Chip **16**, 2188–2191 (2016). Cited on page(s): 18.

[114] M. Yu, Y. Huang, J. Ballweg, H. Shin, M. Huang, D. E. Savage, M. G. Lagally, E. W. Dent, R. H. Blick, and J. C. Williams. *Semiconductor Nanomembrane Tubes: Three-Dimensional Confinement for Controlled Neurite Outgrowth*. ACS Nano **5**, 2447–2457 (2011). Cited on page(s): 18.

[115] A. Koitmäe, M. Müller, C. S. Bausch, J. Harberts, W. Hansen, G. Loers, and R. H. Blick. *Designer Neural Networks with Embedded Semiconductor Microtube Arrays*. Langmuir **34**, 1528–1534 (2018). Cited on page(s): 18.

[116] J. N. Hanson, M. J. Motala, M. L. Heien, M. Gillette, J. Sweedler, and R. G. Nuzzo. *Textural guidance cues for controlling process outgrowth of mammalian neurons*. Lab on a Chip **9**, 122–131 (2009). Cited on page(s): 18.

[117] L. Micholt, A. Gärtner, D. Prodanov, D. Braeken, C. G. Dotti, and C. Bartic. *Substrate Topography Determines Neuronal Polarization and Growth In Vitro*. PLoS ONE **8**, e66170 (2013). Cited on page(s): 18.

[118] T. Limongi, F. Cesca, F. Gentile, R. Marotta, R. Ruffilli, A. Barberis, M. Dal Maschio, E. M. Petrini, S. Santoriello, F. Benfenati, and E. Di Fabrizio. *Nanostructured Superhydrophobic Substrates Trigger the Development of 3D Neuronal Networks*. Small **9**, 402–412 (2013). Cited on page(s): 18.

[119] M. Park, E. Oh, J. Seo, M.-H. Kim, H. Cho, J. Y. Choi, H. Lee, and I. S. Choi. *Control over Neurite Directionality and Neurite Elongation on Anisotropic Micropillar Arrays*. Small **12**, 1148–1152 (2016). Cited on page(s): 18.

[120] H. Amin, M. Dipalo, F. De Angelis, and L. Berdondini. *Biofunctionalized 3D nanopillar arrays fostering cell-guidance and promoting synapse stability and neuronal activity in networks*. ACS Applied Materials & Interfaces , acsami.8b00387 (2018). Cited on page(s): 18.

[121] A. Gladkov, Y. Pigareva, D. Kutyina, V. Kolpakov, A. Bukatin, I. Mukhina, V. Kazantsev, and A. Pimashkin. *Design of Cultured Neuron Networks in vitro with Predefined Connectivity Using Asymmetric Microfluidic Channels*. Scientific Reports **7**, 15625 (2017). Cited on page(s): 19.

[122] J. N. Hanson Shepherd, S. T. Parker, R. F. Shepherd, M. U. Gillette, J. A. Lewis, and R. G. Nuzzo. *3D Microperiodic Hydrogel Scaffolds for Robust Neuronal Cultures*. Advanced Functional Materials **21**, 47–54 (2011). Cited on page(s): 20.

[123] D. D. McKinnon, A. M. Kloxin, and K. S. Anseth. *Synthetic hydrogel platform for three-dimensional culture of embryonic stem cell-derived motor neurons*. Biomaterials Science **1**, 460 (2013). Cited on page(s): 20.

[124] A. Kaneko and Y. Sankai. *Long-Term Culture of Rat Hippocampal Neurons at Low Density in Serum-Free Medium: Combination of the Sandwich Culture Technique with the Three-Dimensional Nanofibrous Hydrogel PuraMatrix*. PLoS ONE **9**, e102703 (2014). Cited on page(s): 20.

[125] M. Frega, M. Tedesco, P. Massobrio, M. Pesce, and S. Martinoia. *Network dynamics of 3D engineered neuronal cultures: a new experimental model for in-vitro electrophysiology*. Scientific Reports **4**, 5489 (2015). Cited on page(s): 20.

[126] Y. S. Nam, J. J. Yoon, and T. G. Park. *A novel fabrication method of macroporous biodegradable polymer scaffolds using gas foaming salt as a porogen additive*. Journal of Biomedical Materials Research **53**, 1–7 (2000). Cited on page(s): 20.

[127] K. Cheng, Y. Lai, and W. S. Kisaalita. *Three-dimensional polymer scaffolds for high throughput cell-based assay systems*. Biomaterials **29**, 2802–2812 (2008). Cited on page(s): 20.

[128] Y. Lai, K. Cheng, and W. Kisaalita. *Three Dimensional Neuronal Cell Cultures More Accurately Model Voltage Gated Calcium Channel Functionality in Freshly Dissected Nerve Tissue*. PLoS ONE **7**, e45074 (2012). Cited on page(s): 20.

[129] D. Yucel, G. T. Kose, and V. Hasirci. *Polyester based nerve guidance conduit design*. Biomaterials **31**, 1596–1603 (2010). Cited on page(s): 20.

[130] F. Sharifi, B. B. Patel, A. K. Dzuilko, R. Montazami, D. S. Sakaguchi, and N. Hashemi. *Polycaprolactone Microfibrous Scaffolds to Navigate Neural Stem Cells*. Biomacromolecules **17**, 3287–3297 (2016). Cited on page(s): 20.

[131] N. Li, Q. Zhang, S. Gao, Q. Song, R. Huang, L. Wang, L. Liu, J. Dai, M. Tang, and G. Cheng. *Three-dimensional graphene foam as a biocompatible and conductive scaffold for neural stem cells*. Scientific Reports **3**, 1604 (2013). Cited on page(s): 20.

[132] M. Malinauskas, M. Farsari, A. Piskarskas, and S. Juodkazis. *Ultrafast laser nanostructuring of photopolymers: A decade of advances*. Physics Reports **533**, 1–31 (2013). Cited on page(s): 20, 31.

[133] F. Larramendy, S. Yoshida, Z. Fekete, D. Serien, S. Takeuchi, and O. Paul*Stackable octahedron-based photoresist scaffold by direct laser writing for controlled three-dimensional cell networks*IEEE (2015).

[134] F. Klein, T. Striebel, J. Fischer, Z. Jiang, C. M. Franz, G. von Freymann, M. Wegener, and M. Bastmeyer. *Elastic Fully Three-dimensional Microstructure Scaffolds for Cell Force Measurements*. Advanced Materials **22**, 868–871 (2010). Cited on page(s): 21.

[135] F. Klein, B. Richter, T. Striebel, C. M. Franz, G. V. Freymann, M. Wegener, and M. Bastmeyer. *Two-component polymer scaffolds for controlled three-dimensional cell culture*. Advanced Materials **23**, 1341–1345 (2011). Cited on page(s): 21, 58.

[136] A. M. Greiner, B. Richter, and M. Bastmeyer. *Micro-Engineered 3D Scaffolds for Cell Culture Studies*. Macromolecular Bioscience **12**, 1301–1314 (2012). Cited on page(s): 21, 58.

[137] V. Melissinaki, A. A. Gill, I. Ortega, M. Vamvakaki, A. Ranella, J. W. Haycock, C. Fotakis, M. Farsari, and F. Claeyssens. *Direct laser writing of 3D scaffolds for neural tissue engineering applications*. Biofabrication **3**, 045005 (2011). Cited on page(s): 21.

[138] S. D. Gittard, A. Nguyen, K. Obata, A. Koroleva, R. J. Narayan, and B. N. Chichkov. *Fabrication of microscale medical devices by two-photon polymerization with multiple foci via a spatial light modulator*. Biomedical Optics Express **2**, 3167 (2011). Cited on page(s): 21.

[139] M. T. Raimondi, S. M. Eaton, M. M. Nava, M. Laganà, G. Cerullo, and R. Osellame. *Two-photon laser polymerization: from fundamentals to biomedical application in tissue engineering and regenerative medicine*. Journal of Applied Biomaterials & Biomechanics , 55–65 (2012). Cited on page(s): 21.

[140] E. Käpylä, D. B. Aydogan, S. Virjula, S. Vanhatupa, S. Miettinen, J. Hyttinen, and M. Kellomäki. *Direct laser writing and geometrical analysis of scaffolds with designed pore architecture for three-dimensional cell culturing*. Journal of Micromechanics and Microengineering **22**, 115016 (2012). Cited on page(s): 21.

[141] A. M. Greiner, F. Klein, T. Gudzenko, B. Richter, T. Striebel, B. G. Wundari, T. J. Autenrieth, M. Wegener, C. M. Franz, and M. Bastmeyer. *Cell type-specific adaptation of cellular and nuclear volume in micro-engineered 3D environments*. Biomaterials **69**, 121–132 (2015). Cited on page(s): 21.

[142] A. Accardo, M. C. Blatché, R. Courson, I. Loubinoux, C. Thibault, L. Malaquin, and C. Vieu. *Multiphoton Direct Laser Writing and 3D Imaging of Polymeric Freestanding Architectures for Cell Colonization*. Small **13**, (2017). Cited on page(s): 21.

[143] S. Turunen, T. Joki, M. L. Hiltunen, T. O. Ihalainen, S. Narkilahti, and M. Kellomäki. *Direct Laser Writing of Tubular Microtowers for 3D Culture of Human Pluripotent Stem Cell-Derived Neuronal Cells*. ACS Applied Materials & Interfaces **9**, 25717–25730 (2017). Cited on page(s): 21.

[144] B. Richter, V. Hahn, S. Bertels, T. K. Claus, M. Wegener, G. Delaittre, C. Barner-Kowollik, and M. Bastmeyer. *Guiding Cell Attachment in 3D Microscaffolds Selectively Functionalized with Two Distinct Adhesion Proteins*. Advanced Materials **29**, 1604342 (2017). Cited on page(s): 21, 31.

[145] A. Accardo, M.-C. Blatché, R. Courson, I. Loubinoux, C. Vieu, and L. Malaquin. *Two-photon lithography and microscopy of 3D hydrogel scaffolds for neuronal cell growth*. Biomedical Physics & Engineering Express **4**, 027009 (2018). Cited on page(s): 21.

[146] S. Tahirovic and F. Bradke. *Neuronal Polarity*. Cold Spring Harbor Perspectives in Biology **1**, a001644–a001644 (2009). Cited on page(s): 22, 23.

[147] B. B. Andersen, L. Korbo, and B. Pakkenberg. *A quantitative study of the human cerebellum with unbiased stereological techniques*. The Journal of Comparative Neurology **326**, 549–560 (1992). Cited on page(s): 22.

[148] S. K. Powell, R. J. Rivas, E. Rodriguez-Boulan, and M. E. Hatten. *Development of polarity in cerebellar granule neurons*. Journal of Neurobiology **32**, 223–236 (1997). Cited on page(s): 23.

[149] J. F. Zmuda and R. J. Rivas. *The Golgi apparatus and the centrosome are localized to the sites of newly emerging axons in cerebellar granule neurons in vitro*. Cell Motility and the Cytoskeleton **41**, 18–38 (1998). Cited on page(s): 23.

[150] A. A. Faisal and S. B. Laughlin. *Stochastic Simulations on the Reliability of Action Potential Propagation in Thin Axons*. PLoS Computational Biology **3**, e79 (2007). Cited on page(s): 23.

[151] P. Chadderton, T. W. Margrie, and M. Häusser. *Integration of quanta in cerebellar granule cells during sensory processing*. Nature **428**, 856–860 (2004). Cited on page(s): 23.

[152] H. Olson, G. Betton, D. Robinson, K. Thomas, A. Monro, G. Kolaja, P. Lilly, J. Sanders, G. Sipes, W. Bracken, M. Dorato, K. Van Deun, P. Smith, B. Berger, and A. Heller. *Concordance of the Toxicity of Pharmaceuticals in Humans and in Animals*. Regulatory Toxicology and Pharmacology **32**, 56–67 (2000). Cited on page(s): 24.

[153] M. Carter and J. Shieh. *Cell Culture Techniques, Guide to Research Techniques in Neuroscience*, 295–310, Elsevier (2015). , URL: `https://linkinghub.elsevier.com/retrieve/pii/B9780128005118000149`. Cited on page(s): 24.

[154] S. Parija, J. Mandal, and S. Acharya. *Ethics in human research*. Tropical Parasitology **1**, 2 (2011). Cited on page(s): 24.

[155] J. L. Sterneckert, P. Reinhardt, and H. R. Schöler. *Investigating human disease using stem cell models*. Nature Reviews Genetics **15**, 625–639 (2014). Cited on page(s): 24–26.

[156] P. J. Schweiger and K. B. Jensen. *Modeling human disease using organotypic cultures*. Current Opinion in Cell Biology **43**, 22–29 (2016). Cited on page(s): 24.

[157] D. A. Robinton and G. Q. Daley. *The promise of induced pluripotent stem cells in research and therapy*. Nature **481**, 295–305 (2012). Cited on page(s): 24.

[158] K. Takahashi and S. Yamanaka. *Induction of Pluripotent Stem Cells from Mouse Embryonic and Adult Fibroblast Cultures by Defined Factors*. Cell **126**, 663–676 (2006). Cited on page(s): 24.

[159] M. Scudellari. *How iPS cells changed the world*. Nature **534**, 310–312 (2016). Cited on page(s): 24.

[160] NobelPrize.org*Shinya Yamanaka Facts.*2019cited on page(s): 24.

[161] K. Takahashi, K. Tanabe, M. Ohnuki, M. Narita, T. Ichisaka, K. Tomoda, and S. Yamanaka. *Induction of Pluripotent Stem Cells from Adult Human Fibroblasts by Defined Factors*. Cell **131**, 861–872 (2007). Cited on page(s): 24.

[162] J. Yu, M. A. Vodyanik, K. Smuga-Otto, J. Antosiewicz-Bourget, J. L. Frane, S. Tian, J. Nie, G. A. Jonsdottir, V. Ruotti, R. Stewart, I. I. Slukvin, and J. A. Thomson. *Induced Pluripotent Stem Cell Lines Derived from Human Somatic Cells*. Science **318**, 1917–1920 (2007). Cited on page(s): 24.

[163] L. Warren, P. D. Manos, T. Ahfeldt, Y.-H. Loh, H. Li, F. Lau, W. Ebina, P. K. Mandal, Z. D. Smith, A. Meissner, G. Q. Daley, A. S. Brack, J. J. Collins, C. Cowan, T. M. Schlaeger, and D. J. Rossi. *Highly Efficient Reprogramming to Pluripotency and Directed Differentiation of Human Cells with Synthetic Modified mRNA*. Cell Stem Cell **7**, 618–630 (2010). Cited on page(s): 25.

[164] F. Anokye-Danso, C. M. Trivedi, D. Juhr, M. Gupta, Z. Cui, Y. Tian, Y. Zhang, W. Yang, P. J. Gruber, J. A. Epstein, and E. E. Morrisey. *Highly Efficient miRNA-Mediated Reprogramming of Mouse and Human Somatic Cells to Pluripotency*. Cell Stem Cell **8**, 376–388 (2011). Cited on page(s): 25.

[165] B.-K. Chou and L. Cheng. *And Then There Were None: No Need for Pluripotency Factors to Induce Reprogramming*. Cell Stem Cell **13**, 261–262 (2013). Cited on page(s): 25.

[166] H. Zhu, M. W. Lensch, P. Cahan, and G. Q. Daley. *Investigating monogenic and complex diseases with pluripotent stem cells*. Nature Reviews Genetics **12**, 266–275 (2011). Cited on page(s): 25.

[167] H. Scho and L. Edge. *iPS Cells 10 Years Later*. Cell **166**, 1356–1359 (2016). Cited on page(s): 25.

[168] M. Mandai, A. Watanabe, Y. Kurimoto, Y. Hirami, C. Morinaga, T. Daimon, M. Fujihara, H. Akimaru, N. Sakai, Y. Shibata, M. Terada, Y. Nomiya, S. Tanishima, M. Nakamura, H. Kamao, S. Sugita, A. Onishi, T. Ito, K. Fujita, S. Kawamata, M. J. Go, C. Shinohara, K.-i. Hata, M. Sawada, M. Yamamoto, S. Ohta, Y. Ohara, K. Yoshida, J. Kuwahara, Y. Kitano, N. Amano, M. Umekage, F. Kitaoka, A. Tanaka, C. Okada, N. Takasu, S. Ogawa, S. Yamanaka, and M. Takahashi. *Autologous Induced Stem-CellDerived Retinal Cells for Macular Degeneration*. New England Journal of Medicine **376**, 1038–1046 (2017). Cited on page(s): 25.

[169] S. S. Han, L. A. Williams, and K. C. Eggan. *Constructing and Deconstructing Stem Cell Models of Neurological Disease*. Neuron **70**, 626–644 (2011). Cited on page(s): 25.

[170] A. SánchezDanés, Y. RichaudPatin, I. CarballoCarbajal, S. JiménezDelgado, C. Caig, S. Mora, C. Di Guglielmo, M. Ezquerra, B. Patel, A. Giralt, J. M. Canals, M. Memo, J. Alberch, J. LópezBarneo, M. Vila, A. M. Cuervo, E. Tolosa, A. Consiglio, and A. Raya. *Diseasespecific phenotypes in dopamine neurons from human iPSbased models of genetic and sporadic Parkinson's disease*. EMBO Molecular Medicine **4**, 380–395 (2012). Cited on page(s): 25.

[171] T. Kondo, M. Asai, K. Tsukita, Y. Kutoku, Y. Ohsawa, Y. Sunada, K. Imamura, N. Egawa, N. Yahata, K. Okita, K. Takahashi, I. Asaka, T. Aoi, A. Watanabe, K. Watanabe, C. Kadoya, R. Nakano, D. Watanabe, K. Maruyama, O. Hori, S. Hibino, T. Choshi, T. Nakahata, H. Hioki, T. Kaneko, M. Naitoh, K. Yoshikawa, S. Yamawaki, S. Suzuki, R. Hata, S.-i. Ueno, T. Seki, K. Kobayashi, T. Toda, K. Murakami, K. Irie, W. L. Klein, H. Mori, T. Asada, R. Takahashi, N. Iwata, S. Yamanaka, and H. Inoue. *Modeling Alzheimer's Disease with iPSCs Reveals Stress Phenotypes Associated with Intracellular Aβ and Differential Drug Responsiveness*. Cell Stem Cell **12**, 487–496 (2013). Cited on page(s): 25.

[172] J. Jo, Y. Xiao, A. X. Sun, E. Cukuroglu, H.-D. Tran, J. Göke, Z. Y. Tan, T. Y. Saw, C.-P. Tan, H. Lokman, Y. Lee, D. Kim, H. S. Ko, S.-O. Kim, J. H. Park, N.-J. Cho, T. M. Hyde, J. E. Kleinman, J. H. Shin, D. R. Weinberger, E. K. Tan, H. S. Je, and H.-H. Ng. *Midbrain-like Organoids from Human Pluripotent Stem Cells Contain Functional Dopaminergic and Neuromelanin-Producing Neurons*. Cell Stem Cell **19**, 248–257 (2016). Cited on page(s): 25.

[173] P. Reinhardt, M. Glatza, K. Hemmer, Y. Tsytsyura, C. S. Thiel, S. Höing, S. Moritz, J. A. Parga, L. Wagner, J. M. Bruder, G. Wu, B. Schmid, A. Röpke, J. Klingauf, J. C. Schwamborn, T. Gasser, H. R. Schöler, and J. Sterneckert. *Derivation and Expansion Using Only Small Molecules of Human Neural Progenitors for Neurodegenerative Disease Modeling*. PLoS ONE **8**, e59252 (2013). Cited on page(s): 25.

[174] H. N. Nguyen, B. Byers, B. Cord, A. Shcheglovitov, J. Byrne, P. Gujar, K. Kee, B. Schüle, R. E. Dolmetsch, W. Langston, T. D. Palmer, and R. R. Pera. *LRRK2 Mutant iPSC-Derived DA Neurons Demonstrate Increased Susceptibility to Oxidative Stress*. Cell Stem Cell **8**, 267–280 (2011). Cited on page(s): 25.

[175] P. Reinhardt, B. Schmid, L. F. Burbulla, D. C. Schöndorf, L. Wagner, M. Glatza, S. Höing, G. Hargus, S. A. Heck, A. Dhingra, G. Wu, S. Müller, K. Brockmann, T. Kluba, M. Maisel, R. Krüger, D. Berg, Y. Tsytsyura, C. S. Thiel, O.-e. Psathaki, J. Klingauf, T. Kuhlmann, M. Klewin, H. Müller, T. Gasser, H. R. Schöler, and J. Sterneckert. *Genetic Correction of a LRRK2 Mutation in Human iPSCs Links Parkinsonian Neurodegeneration to ERK-Dependent Changes in Gene Expression*. Cell Stem Cell **12**, 354–367 (2013). Cited on page(s): 25–27.

[176] S. Puglisi-Allegra and R. Ventura. *Prefrontal/accumbal catecholamine system processes high motivational salience*. Frontiers in Behavioral Neuroscience **6**, 1–13 (2012). Cited on page(s): 26.

[177] J. M. Wenzel, N. A. Rauscher, J. F. Cheer, and E. B. Oleson. *A Role for Phasic Dopamine Release within the Nucleus Accumbens in Encoding Aversion: A Review of the Neurochemical Literature*. ACS Chemical Neuroscience **6**, 16–26 (2015). Cited on page(s): 26.

[178] J. Roeper. *Dissecting the diversity of midbrain dopamine neurons*. Trends in Neurosciences **36**, 336–342 (2013). Cited on page(s): 26.

[179] M. Rice, J. Patel, and S. Cragg. *Dopamine release in the basal ganglia*. Neuroscience **198**, 112–137 (2011). Cited on page(s): 26.

[180] S. Juodkazis, V. Mizeikis, and H. Misawa. *Three-dimensional microfabrication of materials by femtosecond lasers for photonics applications*. Journal of Applied Physics **106**, 051101 (2009). Cited on page(s): 29.

[181] M. Göppert-Mayer. *Über Elementarakte mit zwei Quantensprüngen*. Annalen der Physik **401**, 273–294 (1931). Cited on page(s): 29, 32.

[182] W. Kaiser and C. G. B. Garrett. *Physical review letters of two-photon excitation in CaF Eu'+*. Physical Review **7**, 229–231 (1961). Cited on page(s): 29.

[183] Y. Pao and P. M. Rentzepis. *LASERINDUCED PRODUCTION OF FREE RADICALS IN ORGANIC COMPOUNDS*. Applied Physics Letters **6**, 93–95 (1965). Cited on page(s): 29.

[184] A. Spangenberg, N. Hobeika, F. Stehlin, J. Pierre Malval, F. Wieder, P. Prabhakaran, P. Baldeck, and O. Sopper. *Recent Advances in Two-Photon Stereolithography, Updates in Advanced Lithography,*, InTech (2013). ISBN: 0009-2541, URL: `http://www.intechopen.com/books/updates-in-advanced-lithography/recent-advances-in-two-photon-stereolithography`. Cited on page(s): 29.

[185] W. Denk, J. Strickler, and W. Webb. *Two-photon laser scanning fluorescence microscopy*. Science **248**, 73–76 (1990). Cited on page(s): 30.

[186] C. Xu, W. Zipfel, J. B. Shear, R. M. Williams, and W. W. Webb. *Multiphoton fluorescence excitation: new spectral windows for biological nonlinear microscopy*. Proceedings of the National Academy of Sciences **93**, 10763–10768 (1996). Cited on page(s): 30.

[187] F. Helmchen and W. Denk. *Deep tissue two-photon microscopy*. Nature Methods **2**, 932–940 (2005). Cited on page(s): 30.

[188] J. H. Strickler and W. W. Webb. *Three-dimensional optical data storage in refractive media by two-photon point excitation*. Optics Letters **16**, 1780 (1991). Cited on page(s): 30.

[189] S. Maruo, O. Nakamura, and S. Kawata. *Three-dimensional microfabrication with two-photon-absorbed photopolymerization*. Optics Letters **22**, 132 (1997). Cited on page(s): 30, 35.

[190] S. Kawata, H.-B. Sun, T. Tanaka, and K. Takada. *Finer features for functional microdevices*. Nature **412**, 697–698 (2001). Cited on page(s): 30.

[191] F. Burmeister, S. Steenhusen, R. Houbertz, U. D. Zeitner, S. Nolte, and A. Tünnermann. *Materials and technologies for fabrication of three-dimensional microstructures with sub-100 nm feature sizes by two-photon polymerization*. Journal of Laser Applications **24**, 042014 (2012). Cited on page(s): 30.

[192] J.-F. Xing, X.-Z. Dong, W.-Q. Chen, X.-M. Duan, N. Takeyasu, T. Tanaka, and S. Kawata. *Improving spatial resolution of two-photon microfabrication by using photoinitiator with high initiating efficiency*. Applied Physics Letters **90**, 131106 (2007). Cited on page(s): 30.

[193] V. F. Paz, M. Emons, K. Obata, A. Ovsianikov, S. Peterhänsel, K. Frenner, C. Reinhardt, B. Chichkov, U. Morgner, and W. Osten. *Development of functional sub-100 nm structures with 3D two-photon polymerization technique and optical methods for characterization*. Journal of Laser Applications **24**, 042004 (2012). Cited on page(s): 30.

[194] W. Haske, V. W. Chen, J. M. Hales, W. Dong, S. Barlow, S. R. Marder, and J. W. Perry. *65 nm feature sizes using visible wavelength 3-D multiphoton lithography*. Optics Express **15**, 3426 (2007). Cited on page(s): 30.

[195] R. Wollhofen, J. Katzmann, C. Hrelescu, J. Jacak, and T. A. Klar. *120 nm resolution and 55 nm structure size in STED-lithography*. Optics Express **21**, 10831 (2013). Cited on page(s): 30.

[196] T. A. Klar, R. Wollhofen, and J. Jacak. *Sub-Abbe resolution: from STED microscopy to STED lithography*. Physica Scripta **T162**, 014049 (2014). Cited on page(s): 30, 41.

[197] T. A. Klar. *Miniemulsion Polymerization Technology*. John Wiley & Sons, Inc. (2010). ISBN: 9780470922354, URL: `http://doi.wiley.com/10.1002/9780470922354.pubnote%20http://doi.wiley.com/10.1002/9780470922354`. Cited on page(s): 30.

[198] T. P. Xiao, O. S. Cifci, S. Bhargava, H. Chen, T. Gissibl, W. Zhou, H. Giessen, K. C. Toussaint, E. Yablonovitch, and P. V. Braun. *Diffractive Spectral-Splitting Optical Element Designed by Adjoint-Based Electromagnetic Optimization and Fabricated by Femtosecond 3D Direct Laser Writing*. ACS Photonics **3**, 886–894 (2016). Cited on page(s): 31.

[199] S. Thiele, K. Arzenbacher, T. Gissibl, H. Giessen, and A. M. Herkommer. *3D-printed eagle eye: Compound microlens system for foveated imaging*. Science Advances **3**, e1602655 (2017). Cited on page(s): 31.

[200] U. T. Sanli, H. Ceylan, I. Bykova, M. Weigand, M. Sitti, G. Schütz, and K. Keskinbora. *3D Nanoprinted Plastic Kinoform X-Ray Optics*. Advanced Materials **30**, 1802503 (2018). Cited on page(s): 31.

[201] J. K. Gansel, M. Latzel, A. Frölich, J. Kaschke, M. Thiel, and M. Wegener. *Tapered gold-helix metamaterials as improved circular polarizers*. Applied Physics Letters **100**, 101109 (2012). Cited on page(s): 31.

[202] N. Muller, J. Haberko, C. Marichy, and F. Scheffold. *Silicon Hyperuniform Disordered Photonic Materials with a Pronounced Gap in the Shortwave Infrared*. Advanced Optical Materials **2**, 115–119 (2014). Cited on page(s): 31.

[203] D. Franklin, Y. Chen, A. Vazquez-Guardado, S. Modak, J. Boroumand, D. Xu, S.-T. Wu, and D. Chanda. *Polarization-independent actively tunable colour generation on imprinted plasmonic surfaces*. Nature Communications **6**, 7337 (2015). Cited on page(s): 31.

[204] T. Bückmann, N. Stenger, M. Kadic, J. Kaschke, A. Frölich, T. Kennerknecht, C. Eberl, M. Thiel, and M. Wegener. *Tailored 3D Mechanical Metamaterials Made by Dip-in Direct-Laser-Writing Optical Lithography*. Advanced Materials **24**, 2710–2714 (2012). Cited on page(s): 31.

[205] I. Sakellari, X. Yin, M. L. Nesterov, K. Terzaki, A. Xomalis, and M. Farsari. *3D Chiral Plasmonic Metamaterials Fabricated by Direct Laser Writing: The Twisted Omega Particle*. Advanced Optical Materials **5**, 1700200 (2017). Cited on page(s): 31.

[206] W. C. Lee, Y. J. Heo, and S. Takeuchi. *Wall-less liquid pathways formed with three-dimensional microring arrays*. Applied Physics Letters **101**, 114108 (2012). Cited on page(s): 31.

[207] Y. Li, Y. Fang, J. Wang, L. Wang, S. Tang, C. Jiang, L. Zheng, and Y. Mei. *Integrative optofluidic microcavity with tubular channels and coupled waveguides via two-photon polymerization*. Lab on a Chip **16**, 4406–4414 (2016). Cited on page(s): 31.

[208] G. Nelson, R. A. Kirian, U. Weierstall, N. A. Zatsepin, T. Faragó, T. Baumbach, F. Wilde, F. B. P. Niesler, B. Zimmer, I. Ishigami, M. Hikita, S. Bajt, S.-R. Yeh, D. L. Rousseau, H. N. Chapman, J. C. H. Spence, and M. Heymann. *Three-dimensional-printed gas dynamic virtual nozzles for x-ray laser sample delivery*. Optics Express **24**, 11515 (2016). Cited on page(s): 31.

[209] A. Marino, C. Filippeschi, G. G. Genchi, V. Mattoli, B. Mazzolai, and G. Ciofani. *The Osteoprint: A bioinspired two-photon polymerized 3-D structure for the enhancement of bone-like cell differentiation*. Acta Biomaterialia **10**, 4304–4313 (2014). Cited on page(s): 31.

[210] A. Marino, O. Tricinci, M. Battaglini, C. Filippeschi, V. Mattoli, E. Sinibaldi, and G. Ciofani. *A 3D Real-Scale, Biomimetic, and Biohybrid Model of the Blood-Brain Barrier Fabricated through Two-Photon Lithography*. Small **14**, 1702959 (2018). Cited on page(s): 31.

[211] C. A. Lissandrello, W. F. Gillis, J. Shen, B. W. Pearre, F. Vitale, M. Pasquali, B. J. Holinski, D. J. Chew, A. E. White, and T. J. Gardner. *A micro-scale printable nanoclip for electrical stimulation and recording in small nerves*. Journal of Neural Engineering **14**, 036006 (2017). Cited on page(s): 31.

[212] M. Röhrig, M. Thiel, M. Worgull, and H. Hölscher. *3D Direct Laser Writing of Nano- and Microstructured Hierarchical Gecko-Mimicking Surfaces*. Small **8**, 3009–3015 (2012). Cited on page(s): 31.

[213] M. Suzuki, T. Sawa, Y. Terada, T. Takahashi, and S. Aoyagi*Fabrication of microneedles precisely imitating mosquito's proboscis by nanoscale tree dimensional laser lithography and its characterization*IEEE (2015).

[214] O. Tricinci, T. Terencio, B. Mazzolai, N. M. Pugno, F. Greco, and V. Mattoli. *3D Micropatterned Surface Inspired by Salvinia molesta via Direct Laser Lithography*. ACS Applied Materials & Interfaces **7**, 25560–25567 (2015). Cited on page(s): 31.

[215] M. A. Zeeshan, R. Grisch, E. Pellicer, K. M. Sivaraman, K. E. Peyer, J. Sort, B. Özkale, M. S. Sakar, B. J. Nelson, and S. Pané. *Hybrid Helical Magnetic Microrobots Obtained by 3D Template-Assisted Electrodeposition*. Small **10**, 1284–1288 (2014). Cited on page(s): 31.

[216] T.-Y. Huang, M. S. Sakar, A. Mao, A. J. Petruska, F. Qiu, X.-B. Chen, S. Kennedy, D. Mooney, and B. J. Nelson. *3D Printed Microtransporters: Compound Micromachines for Spatiotemporally Controlled Delivery of Therapeutic Agents*. Advanced Materials **27**, 6644–6650 (2015). Cited on page(s): 31.

[217] H. Zeng, P. Wasylczyk, C. Parmeggiani, D. Martella, M. Burresi, and D. S. Wiersma. *Light-Fueled Microscopic Walkers*. Advanced Materials **27**, 3883–3887 (2015). Cited on page(s): 31.

[218] D. Martella, S. Nocentini, D. Nuzhdin, C. Parmeggiani, and D. S. Wiersma. *Photonic Microhand with Autonomous Action*. Advanced Materials **29**, 1–8 (2017). Cited on page(s): 31.

[219] T. Bückmann, M. Thiel, M. Kadic, R. Schittny, and M. Wegener. *An elasto-mechanical unfeelability cloak made of pentamode metamaterials*. Nature Communications **5**, 4130 (2014). Cited on page(s): 31.

[220] J. Bauer, A. Schroer, R. Schwaiger, and O. Kraft. *Approaching theoretical strength in glassy carbon nanolattices*. Nature Materials **15**, 438–443 (2016). Cited on page(s): 31.

[221] T. Frenzel, M. Kadic, and M. Wegener. *Three-dimensional mechanical metamaterials with a twist*. Science **358**, 1072–1074 (2017). Cited on page(s): 31.

[222] R. K. Jayne, T. J. Stark, J. B. Reeves, D. J. Bishop, and A. E. White. *Dynamic Actuation of Soft 3D Micromechanical Structures Using Micro-Electromechanical Systems (MEMS)*. Advanced Materials Technologies **3**, 1700293 (2018). Cited on page(s): 31.

[223] B. Spagnolo, V. Brunetti, G. Leménager, E. De Luca, L. Sileo, T. Pellegrino, P. Paolo Pompa, M. De Vittorio, and F. Pisanello. *Three-dimensional cage-like microscaffolds for cell invasion studies*. Scientific Reports **5**, 10531 (2015). Cited on page(s): 31.

[224] X.-H. Qin, X. Wang, M. Rottmar, B. J. Nelson, and K. Maniura-Weber. *Near-Infrared Light-Sensitive Polyvinyl Alcohol Hydrogel Photoresist for Spatiotemporal Control of Cell-Instructive 3D Microenvironments*. Advanced Materials **30**, 1705564 (2018). Cited on page(s): 31.

[225] K.-S. Lee, D.-Y. Yang, S. H. Park, and R. H. Kim. *Recent developments in the use of two-photon polymerization in precise 2D and 3D microfabrications*. Polymers for Advanced Technologies **17**, 72–82 (2006). Cited on page(s): 31.

[226] W. G. Fisher, W. P. Partridge, C. Dees, and E. A. Wachter. *Simultaneous Two-Photon Activation of Type-I Photodynamic Therapy Agents*. Photochemistry and Photobiology **66**, 141–155 (1997). Cited on page(s): 31, 34, 35.

[227] F. a. Moscatelli. *A simple conceptual model for twophoton absorption*. American Journal of Physics **54**, 52–54 (1986). Cited on page(s): 31, 33.

[228] K.-S. Lee, R. H. Kim, D.-Y. Yang, and S. H. Park. *Advances in 3D nano/microfabrication using two-photon initiated polymerization*. Progress in Polymer Science **33**, 631–681 (2008). Cited on page(s): 32, 33, 36.

[229] W. K. Bischel, P. J. Kelly, and C. K. Rhodes. *High-resolution Doppler-free two-photon spectroscopic studies of molecules. I. The v3 bands of 12CH3F*. Physical Review A **13**, 1817–1828 (1976). Cited on page(s): 32.

[230] N. Bloembergen and M. D. Levenson. *Doppler-free two-photon absorption spectroscopy*,,315–369, (1976)., URL: `http://link.springer.com/10.1007/3540077197%7B%5C_%7D24`. Cited on page(s): 32.

[231] W. G. Fisher, E. A. Wachter, M. Armas, and C. Seaton. *Titanium:Sapphire laser as an excitation source in two-photon spectroscopy*. Applied Spectroscopy **51**, 218–226 (1997). Cited on page(s): 33.

[232] H.-B. Sun and S. Kawata. *Two-Photon Photopolymerization and 3D Lithographic Microfabrication*, *Advances in Polymer Science*, **170**169–273, (2006). ISBN: 9788578110796, URL: `http://link.springer.com/10.1007/b94405`. Cited on page(s): 33.

[233] S. Turunen. *Direct Laser Writing of Proteins and Synthetic Photoresists for Neuronal Cell Growth Guidance* PhD thesis Tampere University of Technology (2017) cited on page(s): 35.

[234] A. Spangenberg, J.-P. Malval, H. Akdas-Kilig, J.-L. Fillaut, F. Stehlin, N. Hobeika, F. Morlet-Savary, and O. Soppera. *Enhancement of Two-Photon Initiating Efficiency of a 4,4-Diaminostyryl-2,2-bipyridine Derivative Promoted by Complexation with Silver Ions*. Macromolecules **45**, 1262–1269 (2012). Cited on page(s): 36.

[235] M. Malinauskas, A. ukauskas, G. Bikauskait, R. Gadonas, and S. Juodkazis. *Mechanisms of three-dimensional structuring of photo-polymers by tightly focussed femtosecond laser pulses*. Optics Express **18**, 10209 (2010). Cited on page(s): 36.

[236] M. Malinauskas, P. Danileviius, and S. Juodkazis. *Three-dimensional micro-/nano-structuring via direct write polymerization with picosecond laser pulses*. Optics Express **19**, 5602 (2011). Cited on page(s): 36.

[237] T. Baldacchini, S. Snider, and R. Zadoyan. *Two-photon polymerization with variable repetition rate bursts of femtosecond laser pulses*. Optics Express **20**, 29890 (2012). Cited on page(s): 36.

[238] J. Fischer, J. B. Mueller, J. Kaschke, T. J. A. Wolf, A.-N. Unterreiner, and M. Wegener. *Three-dimensional multi-photon direct laser writing with variable repetition rate*. Optics Express **21**, 26244 (2013). Cited on page(s): 36.

[239] X. Zhou, Y. Hou, and J. Lin. *A review on the processing accuracy of two-photon polymerization*. AIP Advances **5**, 030701 (2015). Cited on page(s): 37, 38.

[240] A. Ovsianikov, S. Passinger, R. Houbertz, and B. N. Chichkov. *Three Dimensional Material Processing with Femtosecond Lasers, Laser Ablation and its Applications,* **129**121–157, Springer US (2006). ISBN: 0387304525, URL: `http://link.springer.com/10.1007/978-0-387-30453-3%7B%5C_%7D6`. Cited on page(s): 37.

[241] H.-B. Sun, K. Takada, M.-S. Kim, K.-S. Lee, and S. Kawata. *Scaling laws of voxels in two-photon photopolymerization nanofabrication*. Applied Physics Letters **83**, 1104–1106 (2003). Cited on page(s): 38.

[242] Houbertz, Ruth, Steenhusen, Snke, Stiche, Thomas, and S. Gerhar. *Two-Photon Polymerization of Inorganic-Organic Hybrid Polymers as Scalable Technology Using Ultra-Short Laser Pulses, Coherence and Ultrashort Pulse Laser Emission,*, InTech (2010)., URL: `http://www.intechopen.com/books/coherence-and-ultrashort-pulse-laser-emission/two-photon-polymerization-of-inorganic-organic-hybrid-polymers-as-scalable-technology-using-ultra-sh`. Cited on page(s): 38.

[243] J. Fischer and M. Wegener. *Three-dimensional optical laser lithography beyond the diffraction limit*. Laser & Photonics Reviews **7**, 22–44 (2013). Cited on page(s): 38.

[244] E. Abbe. *Beiträge zur Theorie des Mikroskops und der mikroskopischen Wahrnehmung*. Archiv für Mikroskopische Anatomie **9**, 413–468 (1873). Cited on page(s): 38.

[245] C. M. Sparrow. *On Spectroscopic Resolving Power*. The Astrophysical Journal **44**, 76 (1916). Cited on page(s): 38.

[246] H.-B. Sun, T. Tanaka, and S. Kawata. *Three-dimensional focal spots related to two-photon excitation*. Applied Physics Letters **80**, 3673–3675 (2002). Cited on page(s): 39.

[247] S. Maruo, T. Hasegawa, and N. Yoshimura. *Single-anchor support and supercritical CO_2 drying enable high-precision microfabrication of three-dimensional structures*. Optics Express **17**, 20945 (2009). Cited on page(s): 40, 63.

[248] A. Ovsianikov, X. Shizhou, M. Farsari, M. Vamvakaki, C. Fotakis, and B. N. Chichkov. *Shrinkage of microstructures produced by two-photon polymerization of Zr-based hybrid photosensitive materials*. Optics Express **17**, 2143 (2009). Cited on page(s): 40, 64.

[249] H.-B. Sun, T. Kawakami, Y. Xu, J.-Y. Ye, S. Matuso, H. Misawa, M. Miwa, and R. Kaneko. *Real three-dimensional microstructures fabricated by photopolymerization of resins through two-photon absorption*. Optics Letters **25**, 1110 (2000). Cited on page(s): 41.

[250] R. Wollhofen, B. Buchegger, C. Eder, J. Jacak, J. Kreutzer, and T. A. Klar. *Functional photoresists for sub-diffraction stimulated emission depletion lithography*. Optical Materials Express **7**, 2538 (2017). Cited on page(s): 41.

[251] S. W. Hell and J. Wichmann. *Breaking the diffraction resolution limit by stimulated emission: stimulated-emission-depletion fluorescence microscopy*. Optics Letters **19**, 780 (1994). Cited on page(s): 41.

[252] L. Li, R. R. Gattass, E. Gershgoren, H. Hwang, and J. T. Fourkas. *Achieving /20 Resolution by One-Color Initiation and Deactivation of Polymerization*. Science **324**, 910–913 (2009). Cited on page(s): 41.

[253] J. Fischer and M. Wegener. *Three-dimensional direct laser writing inspired by stimulated-emission-depletion microscopy [Invited]*. Optical Materials Express **1**, 614 (2011). Cited on page(s): 41.

[254] W. R. Zipfel, R. M. Williams, and W. W. Webb. *Nonlinear magic: multiphoton microscopy in the biosciences*. Nature Biotechnology **21**, 1369–1377 (2003). Cited on page(s): 41.

[255] B. O. Leung and K. C. Chou. *Review of Super-Resolution Fluorescence Microscopy for Biology*. Applied Spectroscopy **65**, 967–980 (2011). Cited on page(s): 41.

[256] G. Loers, S. Chen, M. Grumet, and M. Schachner. *Signal transduction pathways implicated in neural recognition molecule L1 triggered neuroprotection and neuritogenesis*. Journal of Neurochemistry **92**, 1463–1476 (2005). Cited on page(s): 43.

[257] C. A. Schneider, W. S. Rasband, and K. W. Eliceiri. *NIH Image to ImageJ: 25 years of image analysis*. Nature Methods **9**, 671–675 (2012). Cited on page(s): 46.

[258] J. Schindelin, I. Arganda-Carreras, E. Frise, V. Kaynig, M. Longair, T. Pietzsch, S. Preibisch, C. Rueden, S. Saalfeld, B. Schmid, J.-Y. Tinevez, D. J. White, V. Hartenstein, K. Eliceiri, P. Tomancak, and A. Cardona. *Fiji: an open-source platform for biological-image analysis*. Nature Methods **9**, 676–682 (2012). Cited on page(s): 46.

[259] R. Rezakhaniha, A. Agianniotis, J. T. C. Schrauwen, A. Griffa, D. Sage, C. V. C. Bouten, F. N. van de Vosse, M. Unser, and N. Stergiopulos. *Experimental investigation of collagen waviness and orientation in the arterial adventitia using confocal laser scanning microscopy*. Biomechanics and Modeling in Mechanobiology **11**, 461–473 (2012). Cited on page(s): 46.

[260] Z. Püspöki, M. Storath, D. Sage, and M. Unser. *Focus on Bio-Image Informatics*. Springer International Publishing (2016). ISBN: 978-3-319-28547-4, URL: `http://link.springer.com/10.1007/978-3-319-28549-8`. Cited on page(s): 46.

[261] J. Harberts. *Installation of a Patch Clamp Setup for Action Potential Studies of Neurons Cultured on InP Solar Cell Nanowire Arrays* MA thesis Universität Hamburg, Germany (2016) cited on page(s): 47.

[262] D. Gall, C. Roussel, I. Susa, E. D'Angelo, P. Rossi, B. Bearzatto, M. C. Galas, D. Blum, S. Schurmans, and S. N. Schiffmann. *Altered Neuronal Excitability in Cerebellar Granule Cells of Mice Lacking Calretinin*. The Journal of Neuroscience **23**, 9320–9327 (2003). Cited on page(s): 47.

[263] H.-C. Eckstein, U. D. Zeitner, R. Leitel, M. Stumpf, P. Schleicher, A. Bräuer, and A. Tünnermann*High dynamic grayscale lithography with an LED-based micro-image stepper* (2016).

[264] H. Mekaru. *Performance of SU-8 Membrane Suitable for Deep X-Ray Grayscale Lithography*. Micromachines **6**, 252–265 (2015). Cited on page(s): 50.

[265] S.-Y. Lee and K. Anbumony. *Accurate control of remaining resist depth for nanoscale three-dimensional structures in electron-beam grayscale lithography*. Journal of Vacuum Science & Technology B: Microelectronics and Nanometer Structures **25**, 2008 (2007). Cited on page(s): 50.

[266] J. Loomis, D. Ratnayake, C. McKenna, and K. M. Walsh. *Grayscale lithographyautomated mask generation for complex three-dimensional topography*. Journal of Micro/Nanolithography, MEMS, and MOEMS **15**, 013511 (2016). Cited on page(s): 50.

[267] C. M. Waits, A. Modafe, and R. Ghodssi. *Investigation of gray-scale technology for large area 3D silicon MEMS structures*. Journal of Micromechanics and Microengineering **13**, 170–177 (2003). Cited on page(s): 50.

[268] H. Jansen, H. Gardeniers, M. de Boer, M. Elwenspoek, and J. Fluitman. *A survey on the reactive ion etching of silicon in microtechnology*. Journal of Micromechanics and Microengineering **6**, 14–28 (1996). Cited on page(s): 52.

[269] G. Smolinsky and D. L. Flamm. *The plasma oxidation of CF4 in a tubularalumina fastflow reactor*. Journal of Applied Physics **50**, 4982–4987 (1979). Cited on page(s): 52.

[270] H. Schift. *Nanoimprint lithography: 2D or not 2D? A review*. Applied Physics A **121**, 415–435 (2015). Cited on page(s): 54.

[271] S. Y. Chou, P. R. Krauss, and P. J. Renstrom. *Imprint of sub25 nm vias and trenches in polymers*. Applied Physics Letters **67**, 3114–3116 (1995). Cited on page(s): 54.

[272] J. Haisma, M. Verheijen, K. van den Heuvel, and J. van den Berg. *Mold-assisted nanolithography: A process for reliable pattern replication*. Journal of Vacuum Science & Technology B: Microelectronics and Nanometer Structures **14**, 4124 (1996). Cited on page(s): 54.

[273] H. Schift. *Nanoimprint lithography: An old story in modern times? A review*. Journal of Vacuum Science & Technology B: Microelectronics and Nanometer Structures **26**, 458 (2008). Cited on page(s): 54.

[274] H. Schift and A. Kristensen. *Nanoimprint Lithography Patterning of Resists Using Molding, Springer Handbook of Nanotechnology*,3rd 271–312, Springer Berlin Heidelberg (2009). ISBN: 9783642025242, . Cited on page(s): 55.

[275] H. Hiroshima and M. Komuro. *Control of Bubble Defects in UV Nanoimprint*. Japanese Journal of Applied Physics **46**, 6391–6394 (2007). Cited on page(s): 56, 57.

[276] X. Liang, H. Tan, Z. Fu, and S. Y. Chou. *Air bubble formation and dissolution in dispensing nanoimprint lithography*. Nanotechnology **18**, 025303 (2007). Cited on page(s): 57.

[277] S. Schlie, A. Ngezahayo, A. Ovsianikov, T. Fabian, H.-A. Kolb, H. Haferkamp, and B. N. Chichkov. *Three-Dimensional Cell Growth on Structures Fabricated from ORMOCER(R) by Two-Photon Polymerization Technique*. Journal of Biomaterials Applications **22**, 275–287 (2007). Cited on page(s): 58.

[278] A. Ovsianikov, J. Viertl, B. Chichkov, M. Oubaha, B. Maccraith, A. Giakoumaki, D. Gray, M. Vamvakaki, M. Farsari, C. Fotakis, P. Microfabrication, I. Sakellari, and A. Giakoumaki. *Ultra-Low Shrinkage Hybrid*. ACS Nano **2**, 2257–2262 (2008). Cited on page(s): 58.

[279] E. D. Lemma, F. Rizzi, T. Dattoma, B. Spagnolo, L. Sileo, A. Qualtieri, M. De Vittorio, and F. Pisanello. *Mechanical Properties Tunability of Three-Dimensional Polymeric Structures in Two-Photon Lithography*. IEEE Transactions on Nanotechnology **16**, 23–31 (2017). Cited on page(s): 58.

[280] H. Van Der Loos and E. M. Glaser. *Autapses in neocortex cerebri: synapses between a pyramidal cell's axon and its own dendrites*. Brain Research **48**, 355–360 (1972). Cited on page(s): 69, 82, 107.

[281] A. Rao, E. M. Cha, and A. M. Craig. *Mismatched appositions of presynaptic and postsynaptic components in isolated hippocampal neurons*. The Journal of neuroscience : the official journal of the Society for Neuroscience **20**, 8344–53 (2000). Cited on page(s): 69, 82.

[282] H. S. Seung, D. D. Lee, B. Y. Reis, and D. W. Tank. *The autapse: A simple illustration of short-term analog memory storage by tuned synaptic feedback*. Journal of Computational Neuroscience **9**, 171–185 (2000). Cited on page(s): 69, 107, 108.

[283] S. P. Khan, G. G. Auner, and G. M. Newaz. *Influence of nanoscale surface roughness on neural cell attachment on silicon*. Nanomedicine: Nanotechnology, Biology and Medicine **1**, 125–129 (2005). Cited on page(s): 70.

[284] I. Nagata and N. Nakatsuji. *Granule cell behavior on laminin in cerebellar microexplant cultures*. Developmental Brain Research **52**, 63–73 (1990). Cited on page(s): 70.

[285] D. Mazia. *Adhesion of cells to surfaces coated with polylysine. Applications to electron microscopy*. The Journal of Cell Biology **66**, 198–200 (1975). Cited on page(s): 70, 72.

[286] S. Kuppusami and R. H. Oskouei. *Parylene Coatings in Medical Devices and Implants: A Review*. Universal Journal of Biomedical Engineering **3**, 9–14 (2015). Cited on page(s): 71.

[287] C. Metallo, R. D. White, and B. A. Trimmer. *Flexible parylene-based microelectrode arrays for high resolution EMG recordings in freely moving small animals*. Journal of Neuroscience Methods **195**, 176–184 (2011). Cited on page(s): 71.

[288] E. M. Schmidt, M. J. Bak, and J. S. McIntosh. *Long-term chronic recording from cortical neurons*. Experimental Neurology **52**, 496–506 (1976). Cited on page(s): 71.

[289] E. M. Schmidt, J. S. Mcintosh, and M. J. Bak. *Long-term implants of Parylene-C coated microelectrodes*. Medical & Biological Engineering & Computing **26**, 96–101 (1988). Cited on page(s): 71.

[290] C. Xu, W. Lemon, and C. Liu. *Design and fabrication of a high-density metal microelectrode array for neural recording*. Sensors and Actuators, A: Physical **96**, 78–85 (2002). Cited on page(s): 71.

[291] J. P. Seymour and D. R. Kipke. *Neural probe design for reduced tissue encapsulation in CNS*. Biomaterials **28**, 3594–3607 (2007). Cited on page(s): 71.

[292] B. D. Winslow, M. B. Christensen, W. K. Yang, F. Solzbacher, and P. A. Tresco. *A comparison of the tissue response to chronically implanted Parylene-C-coated and uncoated planar silicon microelectrode arrays in rat cortex*. Biomaterials **31**, 9163–9172 (2010). Cited on page(s): 71.

[293] A. Dillon, A. Ott, J. Way, and S. George. *Surface chemistry of Al2O3 deposition using Al(CH3)3 and H2O in a binary reaction sequence*. Surface Science **322**, 230–242 (1995). Cited on page(s): 71.

[294] A. Ott, J. Klaus, J. Johnson, and S. George. *Al3O3 thin film growth on Si(100) using binary reaction sequence chemistry*. Thin Solid Films **292**, 135–144 (1997). Cited on page(s): 71.

[295] H. Kim, H.-B.-R. Lee, and W.-J. Maeng. *Applications of atomic layer deposition to nanofabrication and emerging nanodevices*. Thin Solid Films **517**, 2563–2580 (2009). Cited on page(s): 71.

[296] T. V. Thamaraiselvi and S. Rajeswari. *Biological Evaluation of Bioceramic Materials - A Review*. Trends Biomater. Artif. Organs, **18**, 9–17 (2004). Cited on page(s): 71.

[297] D. S. Finch, T. Oreskovic, K. Ramadurai, C. F. Herrmann, S. M. George, and R. L. Mahajan. *Biocompatibility of atomic layer-deposited alumina thin films*. Journal of Biomedical Materials Research Part A **87A**, 100–106 (2008). Cited on page(s): 71.

[298] M. O. Brose, R. J. Avers, M. R. Rieger, and J. E. Duckworth. *Submerged alumina dental root implants in humans: Five-year evaluation*. The Journal of Prosthetic Dentistry **61**, 594–601 (1989). Cited on page(s): 71.

[299] G. Mendonça, D. B. S. Mendonça, L. G. P. Simões, A. L. Araújo, E. R. Leite, W. R. Duarte, L. F. Cooper, and F. J. L. Aragão. *Nanostructured alumina-coated implant surface: Effect on osteoblast-related gene expression and bone-to-implant contact in vivo*. The Journal of Prosthetic Dentistry **104**, 324 (2010). Cited on page(s): 71.

[300] R. Sweitzer, C. Scholz, S. Montezuma, and J. F. Rizzo. *Evaluation of Subretinal Implants Coated with Amorphous Aluminum Oxide and Diamond-like Carbon*. Journal of Bioactive and Compatible Polymers **21**, 5–22 (2006). Cited on page(s): 71.

[301] S. Musallam, M. J. Bak, P. R. Troyk, and R. A. Andersen. *A floating metal microelectrode array for chronic implantation*. Journal of Neuroscience Methods **160**, 122–127 (2007). Cited on page(s): 71.

[302] J. Harberts. *Poly-D-Lysin-Fixierung von Neuronen auf GaAs-Proben mit Hilfe von Fotolitho- graphie und Dimatix Materials Printer* Bachelor's Thesis Universität Hamburg (2013) cited on page(s): 73.

[303] P. Clark, P. Connolly, A. S. Curtis, J. A. Dow, and C. D. Wilkinson. *Topographical control of cell behaviour. I. Simple step cues*. Development (Cambridge, England) **99**, 439–48 (1987). Cited on page(s): 77.

[304] P. Clark, P. Connolly, A. S. Curtis, J. A. Dow, and C. D. Wilkinson. *Topographical control of cell behaviour: II. Multiple grooved substrata*. Development (Cambridge, England) **108**, 635–44 (1990). Cited on page(s): 77.

[305] N. Li and A. Folch. *Integration of topographical and biochemical cues by axons during growth on microfabricated 3-D substrates*. Experimental Cell Research **311**, 307–316 (2005). Cited on page(s): 77, 83.

[306] D. Soltman and V. Subramanian. *Inkjet-Printed Line Morphologies and Temperature Control of the Coffee Ring Effect*. Langmuir **24**, 2224–2231 (2008). Cited on page(s): 81.

[307] N. Nakatsuji and I. Nagata. *Paradoxical perpendicular contact guidance displayed by mouse cerebellar granule cell neurons*. Cell Differentiation and Development **27**, 199 (1989). Cited on page(s): 84.

[308] I. Nagata, A. Kawana, and N. Nakatsuji. *Perpendicular contact guidance of CNS neuroblasts on artificial microstructures*. Development (Cambridge, England) **117**, 401–8 (1993). Cited on page(s): 84.

[309] A. Rajnicek, S. Britland, and C. McCaig. *Contact guidance of CNS neurites on grooved quartz: influence of groove dimensions, neuronal age and cell type*. Journal of cell science **110 ( Pt 2**, 2905–13 (1997). Cited on page(s): 84.

[310] A. Abbott. *Biology's new dimension*. Nature **424**, 870–872 (2003). Cited on page(s): 100.

[311] M. C. LaPlaca, V. N. Vernekar, J. T. Shoemaker, and D. K. Cullen. *Three-Dimensional Neuronal Cultures*. (2010). ISBN: 4043855044, . Cited on page(s): 100.

[312] J. M. Simard, Y. Song, K. Tewari, S. Dunn, K. Werrbach-Perez, J. R. Perez-Polo, and H. M. Eisenberg. *Ionic channel currents in cultured neurons from human cortex*. Journal of Neuroscience Research **34**, 170–178 (1993). Cited on page(s): 101.

[313] T. R. Cummins, Y. Xia, and G. G. Haddad. *Functional properties of rat and human neocortical voltage-sensitive sodium currents*. Journal of Neurophysiology **71**, 1052–1064 (1994). Cited on page(s): 101.

[314] M. Telias, M. Segal, and D. Ben-Yosef. *Electrical maturation of neurons derived from human embryonic stem cells*. F1000Research **3**, 196 (2014). Cited on page(s): 101.

[315] S. J. Tripathy, S. D. Burton, M. Geramita, R. C. Gerkin, and N. N. Urban. *Brain-wide analysis of electrophysiological diversity yields novel categorization of mammalian neuron types*. Journal of Neurophysiology **113**, 3474–3489 (2015). Cited on page(s): 101.

[316] S. Tripathy and R. Gerkin. *NeuroElectro: organizing information on cellular neurophysiology*. URL: `https://neuroelectro.org/` (accessed on ..). Cited on page(s): 101.

[317] J. del Castillo and B. Katz. *Quantal components of the end-plate potential*. The Journal of Physiology **124**, 560–573 (1954). Cited on page(s): 103.

[318] F. A. Edwards, A. Konnerth, and B. Sakmann. *Quantal analysis of inhibitory synaptic transmission in the dentate gyrus of rat hippocampal slices: a patch-clamp study.*. The Journal of Physiology **430**, 213–249 (1990). Cited on page(s): 104.

[319] D. J. Wyllie, T. Manabe, and R. A. Nicoll. *A rise in postsynaptic Ca 2+ potentiates miniature excitatory postsynaptic currents and AMPA responses in hippocampal neurons*. Neuron **12**, 127–138 (1994). Cited on page(s): 104.

[320] K. Inenaga, E. Honda, T. Hirakawa, S. Nakamura, and H. Yamashita. *Glutamatergic Synaptic Inputs to Mouse Supraoptic Neurons in Calcium-Free Medium in vitro/e1*. Journal of Neuroendocrinology **10**, 1–7 (2008). Cited on page(s): 104.

[321] C. S. HERRMANN and A. KLAUS. *AUTAPSE TURNS NEURON INTO OSCILLATOR*. International Journal of Bifurcation and Chaos **14**, 623–633 (2004). Cited on page(s): 107.

[322] Y. K. Kim, J. A. Park, W. H. Yoon, J. Kim, and S. Jung. *Drop-on-demand inkjet-based cell printing with 30- $\mu$m nozzle diameter for cell-level accuracy*. Biomicrofluidics **10**, 064110 (2016). Cited on page(s): 108.

[323] J. Erickson, A. Tooker, Y. C. Tai, and J. Pine. *Caged neuron MEA: A system for long-term investigation of cultured neural network connectivity*. Journal of Neuroscience Methods **175**, 1–16 (2008). Cited on page(s): 109.

[324] M. Shein, A. Greenbaum, T. Gabay, R. Sorkin, M. David-Pur, E. Ben-Jacob, and Y. Hanein. *Engineered neuronal circuits shaped and interfaced with carbon nanotube microelectrode arrays*. Biomedical Microdevices **11**, 495–501 (2009). Cited on page(s): 109.

[325] A. M. Taylor, S. Menon, and S. L. Gupton. *Passive microfluidic chamber for long-term imaging of axon guidance in response to soluble gradients*. Lab on a Chip **15**, 2781–2789 (2015). Cited on page(s): 110.

[326] D. Pamies, T. Hartung, and H. T. Hogberg. *Biological and medical applications of a brain-on-a-chip*. Experimental Biology and Medicine **239**, 1096–1107 (2014). Cited on page(s): 110.

# Danksagung

An dieser Stelle möchte ich mich bei allen bedanken, die mich in den letzten Jahren begleitet haben und ohne die diese Arbeit nicht möglich gewesen wäre. Ich bedanke mich bei:

-Prof. Dr. Robert H. Blick für die stetige Unterstützung, das Vertrauen in meine Arbeit, die hervorragenden Voraussetzungen, die er sowohl bei der technischen Ausstattung als auch auf menschlicher Ebene in der Gruppe geschaffen hat, und natürlich die Übernahme des Erstgutachtens.

-Dr. Robert Zierold für die hilfreichen wöchentlichen Meetings, die allgemeine Hilfsbereitschaft, die wissenschaftliche Unterstützung, leckeres Grillen bei ihm zu Hause und für das ausführliche Korrekturlesen.

-Ein besonderer Dank gilt Jann Harberts für alles, was er in unserem Biolab auf die Beine gestellt hat, die Unterstützung und Zusammenarbeit, die essenziell war zum Zustandekommen dieser Arbeit, die Pflege der smNPCs, für die tolle Zeit auf gemeinsamen Reisen, natürlich die Mitbegründung des Filmklubs und die gute Freundschaft, die über die Zeit entstanden ist.

-Dr. Christian Denker und Prof. Dr. Markus Münzenberg für die Einladung nach Greifswald zur Einweisung in das NanoScribe PPGT und die anschließende hervorragende Kooperation.

-Dr. Gabriele Loers für die allgemeine Hilfsbereitschaft und stetige Versorgung mit MCGCs.

-Michael Glatza, für die Einladung an das Max Planck Institut nach Münster und in Einweisung in die Geheimnisse der iPSCs, als auch für die nachträgliche Unterstützung.

-Dr. Jonas Sichau, mit dem ich (wenn auch in sehr verschiedenen Forschungsfeldern) parallel den Weg als Masterand und Doktorand beschritten und sehr gerne ein Büro geteilt habe.

-Gerda Ekindorf für das Korrekturlesen und die schöne bisherige gemeinsame Zeit.

-Andreas Schlegel für das Korrekturlesen und ebenfalls die Mitbegründung des besten Filmklubs Hamburgs.

-Dr. Aune Koitmäe für die Einarbeitung ins Biolab zu Beginn der Arbeit.

-Niklas Rieck, Jeremy Teuber, Lars Raffeldt, Charline Becker und Oliver Aust für die Mitarbeit im Labor.

-Prof. Dr. Wolfgang Parak für die Übernahme des Zweitgutachtens.

-Prof. Dr. Michael A. Rübhausen, Prof. Dr. Viacheslav Nikolaev und Prof. Dr. Gabriel Bester für die Einwilligung zur Teilnahme der Disputationsprüfung.

-Andrea Köppen und Christina Lampe für die technische Unterstützung und Betreuung im Reinraum in der Jungiusstraße.

-Der gesamten Gruppe H/B + Marten Rittner und Katrin Groth für die schöne gemeinsame Zeit am CHyN.

# Eidesstattliche Versicherung / Declaration on Oath

Hiermit versichere ich an Eides statt, die vorliegende Dissertationsschrift selbst verfasst und keine anderen als die angegebenen Hilfsmittel und Quellen benutzt zu haben.

Die eingereichte schriftliche Fassung entspricht der auf dem elektronischen Speichermedium.

Die Dissertation wurde in der vorgelegten oder einer ähnlichen Form nicht schon einmal in einem früheren Promotionsverfahren angenommen oder als ungenügend beurteilt.

Hamburg, den 13.12.2019

Cornelius Fendler